A Thesis for the Doctor's Degree of Science

Dark Matter Search Experiment in a Deep Underground Laboratory with LiF Bolometer

Kentaro Miuchi
Department of Physics, School of Science,
University of Tokyo

March 2002

Abstract

Dark matter is one of the largest astrophysical problem that is still unsolved. The SUSY particle neutralino is one of the strongest candidates for the dark matter. It is predicted that neutralino can be detected by the elastic scattering with the ordinary matter. We performed an experiment with a LiF bolometer aiming for a direct detection of the neutralino dark matter. Since low cosmic ray background environment is indispensable for the expected low rate neutralino detection, we performed the measurement at Kamioka Observatory that is located 2,700 m.w.e. underground. With some improvements for the low background and low threshold measurement, we started our dark matter measurement in November 2001.

In this experiment, we obtained spin-independent neutralino-proton cross section($\sigma^{\rm SI}_{\chi-{\rm p}}$) upper limit of 0.055 pb and spin-dependent neutralino-proton cross section($\sigma^{\rm SD}_{\chi-{\rm p}}$) upper limit of 21 pb for the neutralinos with mass 28GeVc^{-2}.

We derived the limits in the $\sigma^{\rm SD}_{\chi-{\rm p}}$-$\sigma^{\rm SD}_{\chi-{\rm n}}$ plane and in the $a_{\rm p} - a_{\rm n}$(neutralino-nucleon spin-dependent couplings) plane. We excluded a part of the parameter space allowed by the DAMA's annual modulation results for the neutralinos with mass heavier than 50GeVc^{-2}. We also excluded a part of the parameter space which is not excluded by the DAMA's upper limits for the neutralinos with mass lighter than 15GeVc^{-2} and heavier than 100GeVc^{-2}.

Contents

Chapter 1

Dark Matter

1.1 Dark Matter Problem

1.1.1 Observational Evidence

It is well known that the mass of the universe mostly consists of the dark matter[1]. The rotation velocities of spiral galaxies measured by observing atomic hydrogen clouds are found to be flat out to the maximum observed radii of about 30 kpc, while the ordinary luminous matters converge within 10 kpc[2, 3]. These results firmly support the existence of the galactic halos, which consist of non-luminous matters surrounding the galaxies. Similar results are obtained by the observations of the elliptical galaxies and the clusters of galaxies[2, 3].

1.1.2 Flat Universe, Matter Density, and Dark Matter Density

There are several candidates of the dark matter and the contribution of each candidate to the whole universe is expressed by its energy density like other ordinary components of the universe. Ω_i, a parameter that expresses the ratio of the energy density of each component to the critical density, is often used.

$$\Omega_i = \frac{\rho_i}{\rho_{\rm c}} \tag{1.1}$$

where $\rho_{\rm i}$ is the energy density of a component i, $\rho_{\rm c} \equiv 3H_0^2/8\pi G_{\rm N}$ is the critical density at which the universe is balanced between the infinite expansion and the eventual re-collapse, H_0 is the present value of the Hubble constant, and $G_{\rm N} = 6.71 \times 10^{-39}\hbar c({\rm GeV/c^2})^{-2}$ is the gravitational constant. The total density ρ_0 is expressed as

$$\Omega_0 = \Sigma_i \Omega_i = \Omega_{\rm m} + \Omega_{\rm e} \tag{1.2}$$

where $\Omega_{\rm m}$ and $\Omega_{\rm e}$ are the pressureless matter density and the energy density, respectively. Observations of the anisotropy of the Cosmic Microwave Background(CMB) imply the value

of Ω_0. Boomerang experiment[4] gives the result of $0.88 < \Omega_0 < 1.12$ and MAXIMA[5] shows $\Omega_0 = 1.0^{+0.15}_{-0.30}$. These values are consistent with flat universe with

$$\Omega_0 = 1. \tag{1.3}$$

Observations of the high-redshift supernovae[6] give

$$0.8\Omega_{\rm m} - 0.6\Omega_{\rm e} \sim -0.2 \pm 0.1 \tag{1.4}$$

If we assume the flat universe as shown in Eq.(1.3), Eq. (1.2) and Eq. (1.4) give

$$\Omega_{\rm m}^{\rm flat} = 0.28^{+0.09}_{-0.08}({\rm statistical})^{+0.05}_{-0.04}({\rm systematics}). \tag{1.5}$$

Densities of some components are well measured or estimated[1]. The density of the luminous stars is estimated to be

$$\Omega_{\rm luminous} = 0.004 \tag{1.6}$$

as a consequence of Big Bang Nucleosynthesis(BBN) cosmology. Photons of the CMB have $\rho_\gamma = \frac{\pi^2}{15} T_0^4$, where $T_0 = 2.73$K is the present tempreture, thus

$$\Omega_\gamma = 5.1 \times 10^{-5}. \tag{1.7}$$

Densities discussed above are summarized in Table 1.1.

Ω_0	1
$\Omega_{\rm m}^{\rm flat}$	0.28
$\Omega_{\rm luminous}$	0.004
Ω_γ	5.1×10^{-5}

Table 1.1: Matter densities in the universe[1].

Therefore, quite a few part of the matter density is unobserved and is referred to as the dark matter. Taking the values in Table 1.1, the dark matter density $\Omega_{\rm D}$ is estimated to be at least 0.25.

For the detection of dark matter, it is important to know the density of the dark matter around us. The local dark halo density is estimated for several galactic halo models and they are summarized in Table 1.2[7].

In this thesis, we take $0.3{\rm GeVc}^{-2}{\rm cm}^{-3}$ for calculations since this is used as the standard value by many dark matter search experiments.

1.2 Dark Matter Candidates

There are two types of dark matter candidates: baryonic and non-baryonic candidates. We will describe the features of these two types of candidates in this section.

$\rho_{\mathrm{D}}[\mathrm{GeVc^{-2}cm^{-3}}]$	halo model
$0.34 - 0.72$	standard halo (flattening= $2.5:1$)
$0.29 - 0.61$	spherical halo
$0.61 - 1.3$	flattened halo

Table 1.2: Dark matter densities ρ_{D} for various shapes of the galactic halo[7].

1.2.1 Baryonic Candidates

There are two main ways to estimate the density of the baryonic dark matter. One is the observation of the MAssive Compact Halo Objects(MACHOs) and the other is the Big Bang Nucleosynthesis(BBN) and the observation of the abundance of light elements.

- Observations of MACHOs
  MAssive Compact Halo Objects(MACHOs) are thought to be good candidates of the dark matter and observations of MACHOs have been performed for years. Most probable candidates for the MACHOs are light brown dwarfs with masses smaller than $0.08\mathrm{M}_{\odot}$. They are made of hydrogen and helium and their temperature never become high enough to ignite the hydrogen fusion. Therefore they just radiate very weakly in the infrared due to the gravitational contraction. Old dwarfs, neutron stars and black holes are thought to be other candidates for MACHOs. If a MACHO passes very close to the line of the sight to the background star, the light of the star is amplified by the gravitational microlensing. MACHO project[8] observed the light curves of 8.5 million stars in the Large Magellanic Cloud and found 8 candidates in 2.3 years. Though 8 candidates are in excess of expected background arising from the known stellar populations, they are not thought to form the substantial fraction of the galactic dark halo. The candidates have long timescales of 1 to 6 months, which infer the masses of about $0.5M_{\odot}$ and these objects are limited to form less than 3% of the halo mass.

- BBN and the Observation of the Abundance of Light Elements.
  The Big Bang Nucleosynthesis(BBN) explains the early universe up to one second well and predicts the abundance of light elements: $^4\mathrm{He}, ^3\mathrm{He}, ^2\mathrm{H}$, and $^7\mathrm{Li}$ by one parameter: η, the baryon-to-photon ratio, where $\eta = 273 \times 10^{-10}\Omega_{\mathrm{B}}(H_0/100)^2$[9]. Observations of the D/H ratio and ^{4}He abundance restrict η into two regions as shown in Eq. (1.8).

$$\eta \sim (1.2 - 2.8) \times 10^{-10}, (4.2 - 6.3) \times 10^{-10} \tag{1.8}$$

  Thus baryon density Ω_{B} are found to have the value

$$0.01 < \Omega_{\mathrm{B}} < 0.05. \tag{1.9}$$

Observations of the MACHOs and the BBN both indicate that baryonic dark matter candidates consist some part of the dark matter, though a substantial part of dark matter is taken by the non-baryonic dark matter.

1.2.2 Non-Baryonic Candidates

Although some of the baryonic candidates have been found to occupy a part of the dark matter, we still need other candidates for $\Omega_{\rm m}^{\rm flat} = 0.28$. Non-baryonic dark matter candidates can be classified into the hot dark matter(HDM) and the cold dark matter (CDM) depending on whether the dark matter particles were relativistic or nonrelativistic at the time when the horizon of the universe enclosed enough matter to form a galaxy. Among these candidates, neutrinos, axions, and neutralinos are thought to be the most plausible ones[10].

- Neutrino
  The neutrino is a HDM candidate. Evidences for the oscillation of atmospheric neutrinos presented by the Super-Kamiokande Collaboration[11] and the oscillation of solar neutrinos presented by the Super-Kamiokande Collaboration[12] and confirmed by the SNO Collaboration[13] indicate that neutrinos have mass. As the other two candidates are merely hypothetical particles, neutrinos are the only known non-baryonic dark matter.

The anisotropy of the CMB supports the CDM[4], therefore, the other two candidates are also promising dark matter candidate, though they are both only hypothetical particles.

- Axion
  The axion is a light boson proposed by Peccei and Quinn [14] in 1977 to solve the strong CP violation problem. With mass in the range between $10^{-2}\mathrm{eVc}^{-2}$ and $10^{-5}\mathrm{eVc}^{-2}$, axion can be a CDM. Several searches for the dark matter axions have been performed or are under way[15, 16, 17], but there has not been a positive result.

- Neutralino
  The neutralino is a supersymmetric particle and the lightest neutralino is a promising CDM candidate. Details are described in Section 2 and 3.

Chapter 2

Neutralino

2.1 SM and SUSY

The 'Standard Model'(SM) of the elementary particle physics is a non-Abelian gauge theory based on the gauge group $SU(3)_{\rm C} \times SU(2)_{\rm L} \times U(1)_{\rm Y}$. Although the SM is a very successful theory which describes all experimental results with a surprising accuracy, there are some questions remaining unanswered which can be solved with the supersymmetric(SUSY) extension of the standard model[18]. Some of the questions are

- The SM requires at least 18 free input parameters(fermion masses, $\sin^2\theta_{\rm W}$, etc.).
- There is no framework where the gravity is incorporated.
- The Hierarchy Problem exists.

Among the several questions, the Hierarchy Problem is the most embarrassing one to the SM and is the direct motivation to require supersymmetric extension. The radiative corrections to the scalar Higgs boson masses and the gauge boson masses have quadratic divergences at large loop momentum. The energy cut-off Λ is required to avoid this divergences. For Higgs boson masses,

$$\begin{aligned} M_{\rm H}^2 &= M_0^2 + \delta M_{\rm H}^2 \\ \delta M_{\rm H}^2 &\sim g^2\Lambda^2 \end{aligned} \tag{2.1}$$

where M_0 is the bare mass of the Higgs boson, δM_H is the mass correction. The experimental results suggest $M_{\rm H} > 114.3{\rm GeVc}^{-2}$[1]. On the other hand, it is natural to consider the cut-off energy to be the GUT scale $\sim 10^{15}{\rm GeVc}^{-2}$ or the Plank scale $\sim 10^{19}{\rm GeVc}^{-2}$, that means the correction is many orders of magnitude larger than the mass itself. The SUSY model provides a solution to this Hierarchy problem. In the SUSY model, the loop corrections to the Higgs boson masses contain the contributions of both fermions and bosons. Since the

supersymmetry is not an exact symmetry below the typical SUSY breaking scale $M_{\rm SUSY}$, two contributions do not exactly cancel out: i.e.

$$\delta M_{\rm H}^2 \sim O(10^{-2}) M_{\rm SUSY}^2 \tag{2.2}$$

The typical SUSY breaking mass scale can be estimated by requiring that the Higgs boson mass is heavier than its radiative correction: $\delta M_{\rm H} < M_{\rm H}$. From Eq.(2.1) and Eq.(2.2), we obtain

$$M_{\rm SUSY} \leq 1{\rm TeVc}^{-2}. \tag{2.3}$$

2.2 Structures of the MSSM

The minimal supersymmetric extension of the Standard Model(MSSM) consists of the elementary particles in the SM and corresponding supersymmetric partners. Particles with spin j in SM has supersymmetric partners with spin $|j - 1/2|$. Other internal quantum numbers are identical with those in the SM. The particles presupposed in the SUSY model are shown in Table 2.1.

Normal particles			SUSY partners		
Symbol	Name	Spin	Spin	Name	Symbol
$q = u, c, t$	up quarks	1/2	0	up squarks	$\tilde{q}_u^1, ..., \tilde{q}_u^6$
$q = d, s, b$	down quarks	1/2	0	down squarks	$\tilde{q}_d^1, ..., \tilde{q}_d^6$
$l = e, \mu, \tau$	leptons	1/2	0	sleptons	$\tilde{l}_1, ..., \tilde{l}_6$
ν_e, ν_μ, ν_τ	neutrinos	1/2	0	sneutrinos	$\tilde{\nu}_1, \tilde{\nu}_2, \tilde{\nu}_3$
g	gluons	1	1/2	gluinos	$\tilde{g}$
$W^\pm$	W boson	1	1/2	charginos	$\tilde{\chi}_1^\pm, \tilde{\chi}_2^\pm$
$H^\pm$	charged Higgs	0			
γ	photon	1	1/2	neutralinos	$\tilde{\chi}_1^0, ..., \tilde{\chi}_4^0$
Z^0	Z boson	1			
$h^0(H_2^0)$	light scalar Higgs	0			
$H^0(H_1^0)$	heavy scalar Higgs	0			
$A^0(H_3^0, P_0)$	pseudoscalar Higgs	0			

Table 2.1: Particles presupposed in the SUSY model[18].

2.3 Neutralino

In the minimum supersymmetric extension of the standard model(MSSM), the interactions between SUSY particles and ordinary particles are governed by 'R-Parity'. R-parity is defined as,

$$R = (-1)^{3B+L+2S} \tag{2.4}$$

where B is the baryon number, L is the lepton number and S is the spin. SUSY particles are assigned odd R-parities and the ordinary matter particles are assigned even R-parities. According to the R-parity conservation, heavier SUSY particles could decay into lighter ones and the lightest supersymmetric particle(LSP) is stable because decays into the ordinary particles violate R-parity conservation.

The lightest neutralino (χ), the lowest-mass linear combination of photino($\tilde{\gamma}$), zino($\tilde{Z}$), and higgsinos($\tilde{H}_1, \tilde{H}_2$) is the leading candidate for LSP and also for the non-baryonic cold dark matter. The photino and the zino are expressed with the superpartners of gauge bosons the Bino($\tilde{B}$) and the Wino($\tilde{W}$).

$$\begin{aligned} \tilde{\gamma} &= \cos\theta_{\rm W}\tilde{B} + \sin\theta_{\rm W}\tilde{W}_3 \\ \tilde{\rm Z} &= -\sin\theta_{\rm W}\tilde{B} + \cos\theta_{\rm W}\tilde{W}_3 \end{aligned} \tag{2.5}$$

Therefore, χ can be written as

$$\chi = a_1\tilde{B} + a_2\tilde{W}_3 + a_3\tilde{H}_1 + a_4\tilde{H}_2. \tag{2.6}$$

Neutralino mass matrix is written as Eq.(2.7)

$$\begin{pmatrix} M_1 & 0 & -M_{\rm Z}\cos\beta\sin\theta_{\rm W} & M_{\rm Z}\cos\beta\cos\theta_{\rm W} \\ 0 & M_2 & M_{\rm Z}\sin\beta\sin\theta_{\rm W} & -M_{\rm Z}\sin\beta\cos\theta_{\rm W} \\ -M_{\rm Z}\cos\beta\sin\theta_{\rm W} & M_{\rm Z}\sin\beta\sin\theta_{\rm W} & 0 & -\mu \\ M_{\rm Z}\cos\beta\cos\theta_{\rm W} & -M_{\rm Z}\sin\beta\cos\theta_{\rm W} & -\mu & 0 \end{pmatrix} \tag{2.7}$$

where M_1 and M_2 are the gaugino masses, μ is the higgsino mass parameter, and $\tan\beta = v_2/v_1$, where v_1 and v_2 are the vacuum expectation values of the two Higgses. If we assume the grand unification, $M_1 = (5/3)M_2\tan^2\theta_{\rm W} \sim 0.5M_2$ is obtained, thus the neutralino mass matrix is characterized by three parameters: μ, M_2, and $\tan\beta$. Fig.2.1 and Fig.2.2 shows calculated neutralino masses and gaugino fractions in the (M_2, μ) plane.

2.4 Review of Neutralino Search Experiments

There have been three types of the neutralino search experiments: direct search experiments, indirect search experiments and search by accelerator experiments. We will review these experiments in this section.

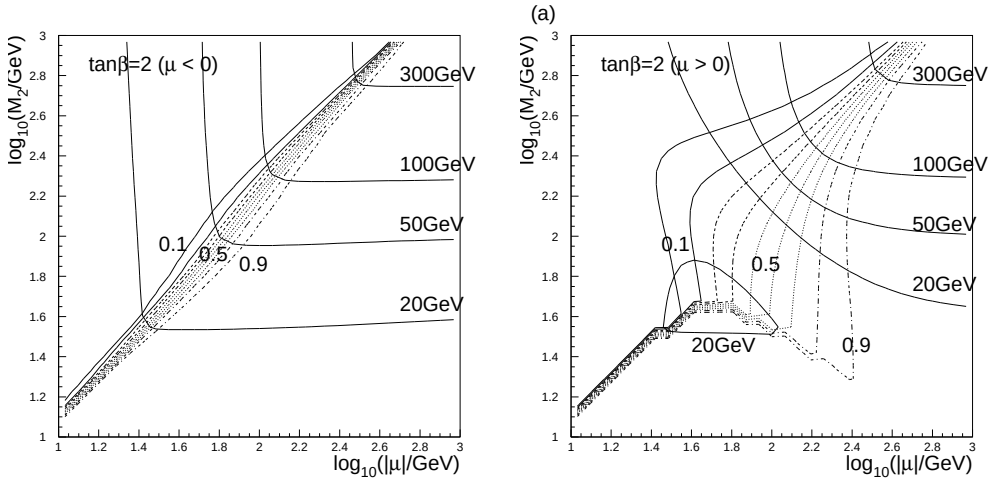

Figure 2.1: Contours of the neutralino mass and gaugino fraction. ($\tan\beta = 2$)[19]

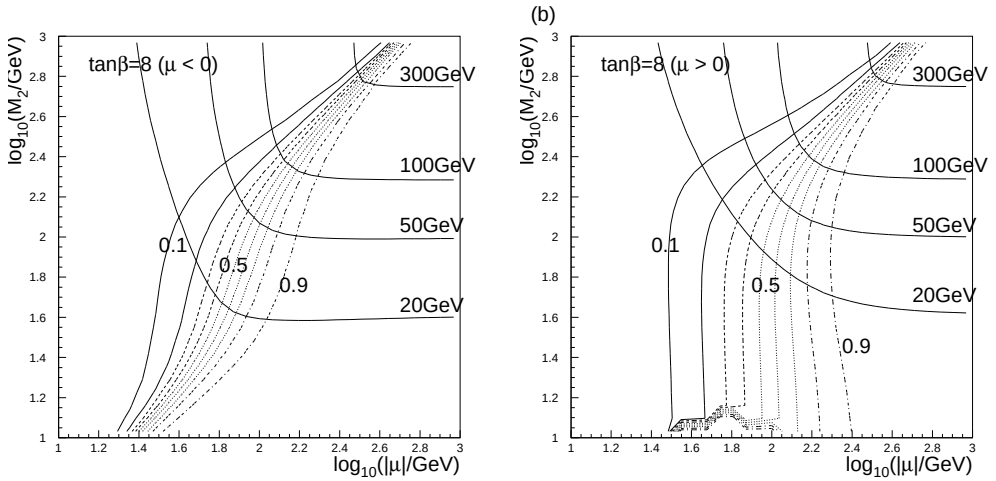

Figure 2.2: Contours of the neutralino mass and gaugino fraction. ($\tan\beta = 8$)[19]

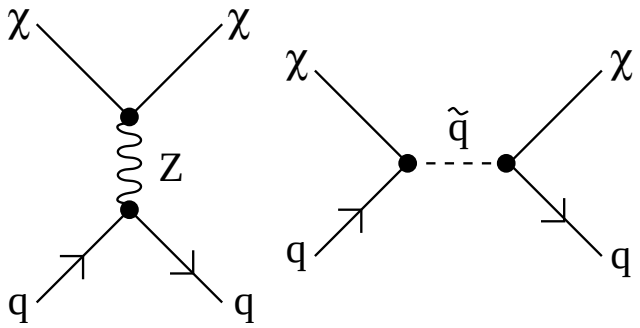

Figure 2.3: Feynman diagram contributing to the spin-dependent elastic scattering of neutralino from quarks.

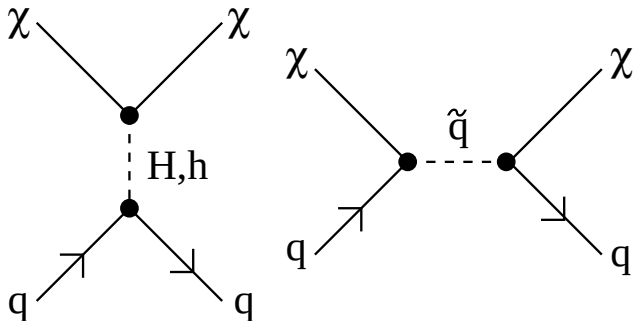

Figure 2.4: Feynman diagram contributing to the spin-independent elastic scattering of neutralino from quarks.

2.4.1 Direct Search

Neutralinos can be detected via elastic scattering with ordinary matters. Feynman diagrams of the spin-dependent and spin-independent neutralino-quark elastic scatterings are shown in 2.3 and 2.4, respectively. Limits to the neutralino-nucleon cross section have been improved since the first result with a Ge semiconductor was shown[20]. Then, in 1998, DAMA group published their first 'positive' result based on the annual modulation measurement[21]. DAMA group published their updated results successively[22]. The WIMP parameter region claimed by the DAMA group is $M_\chi = (52^{+10}_{-8})\mathrm{GeVc}^{-2}$ and $\sigma^{\mathrm{SI}}_{\chi-\mathrm{p}} = (7.2^{+0.4}_{-0.9})\cdot 10^{-6}\mathrm{pb}$ at 4σ C.L. with standard astrophysical parameters[1]. Here, the superscript SI means 'spin-independent' cross section. However, in the year of 2000, CDMS group published their first result and killed most of the parameter space claimed by the DAMA group[23]. Results are shown in Fig. 2.5. Several experiments are running or in preparation for the investigation of the whole DAMA region and exploration the parameter space predicted by MSSM[24, 25].

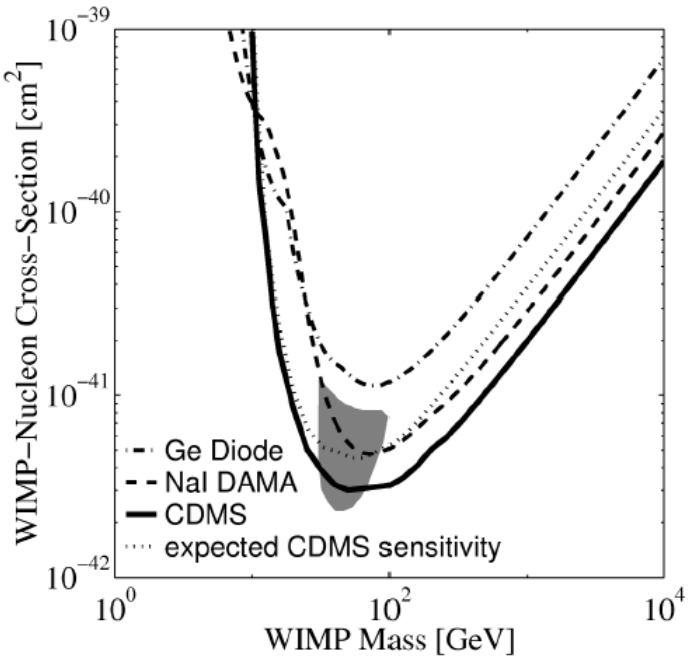

Figure 2.5: Spin-independent neutralino-proton cross section ($\sigma^{\mathrm{SI}}_{\chi-\mathrm{p}}$) as a function of neutralino mass(M_χ) The cross sections are shown in units of 1pb($=10^{-36}\mathrm{cm}^2$) in the figure. The regions above the curves are excluded at 90 % C.L. The gray region shows the DAMA's positive result. This figure is taken from Ref. [23].

[1]The gray region in Fig. 2.5 representing the DAMA's positive result is taken from Ref. [21] and the values in the sentence are taken from updated references[22]. Therefore these two are not exactly identical.

These results and projects are mainly aiming to detect neutralinos by spin-independent(SI) interaction. As we will describe in Section 3, neutralinos can be detected also by spin-dependent(SD) interaction and several experiments have set the limits to the SD neutralino-nucleon cross section[26, 27, 29, 30]. Results of the spin-dependent interaction are shown in Fig. 2.6[30].

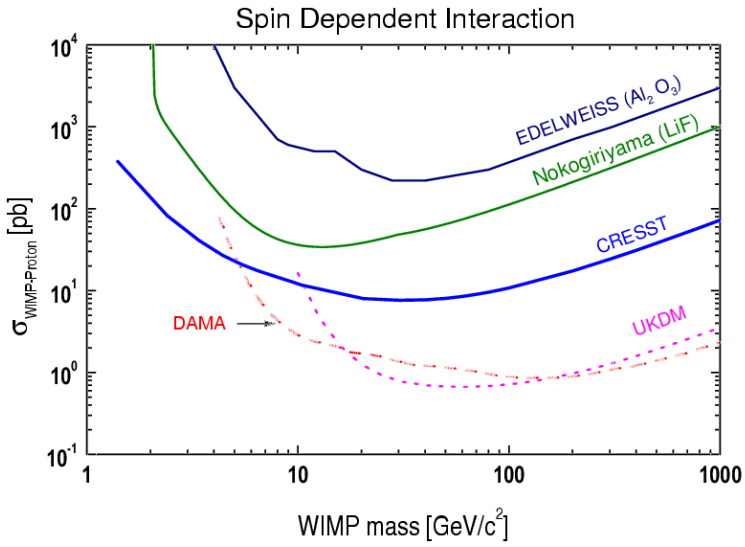

Figure 2.6: Spin-dependent neutralino-proton cross section($\sigma^{SD}_{\chi-p}$) as a function of neutralino mass(M_χ). The regions above the curves are excluded at 90 % C.L. This figure is taken from Ref. [30].

There is also an attempt to interpret the DAMA's positive result in the SD-SI mixed coupling framework[31]. Fig. 2.7 shows the result of this analysis. In this figure, allowed regions of the $\sigma^{SD}_{\chi-p}$ are shown for three $\sigma^{SI}_{\chi-p}$ values and four types of neutralino.

Neutralinos could also interact with nucleus via inelastic scattering and excite the nucleus. In this case, we can detect gamma rays which are resulted from de-excitation, and thus can have a much background reduction[18]. However, the cross section expected for these interactions are usually extremely small except for iodine[32].

2.4.2 Indirect Search

Neutralinos can be trapped in the core of the Earth, the Sun, Galactic center and annihilate with each other. The annihilation process has many channels as listed in Table 2.2. Most of the decay products will decay and be absorbed by the materials near by almost immediately. However, when muon neutrinos are produced, they can pass through the Earth or Sun and

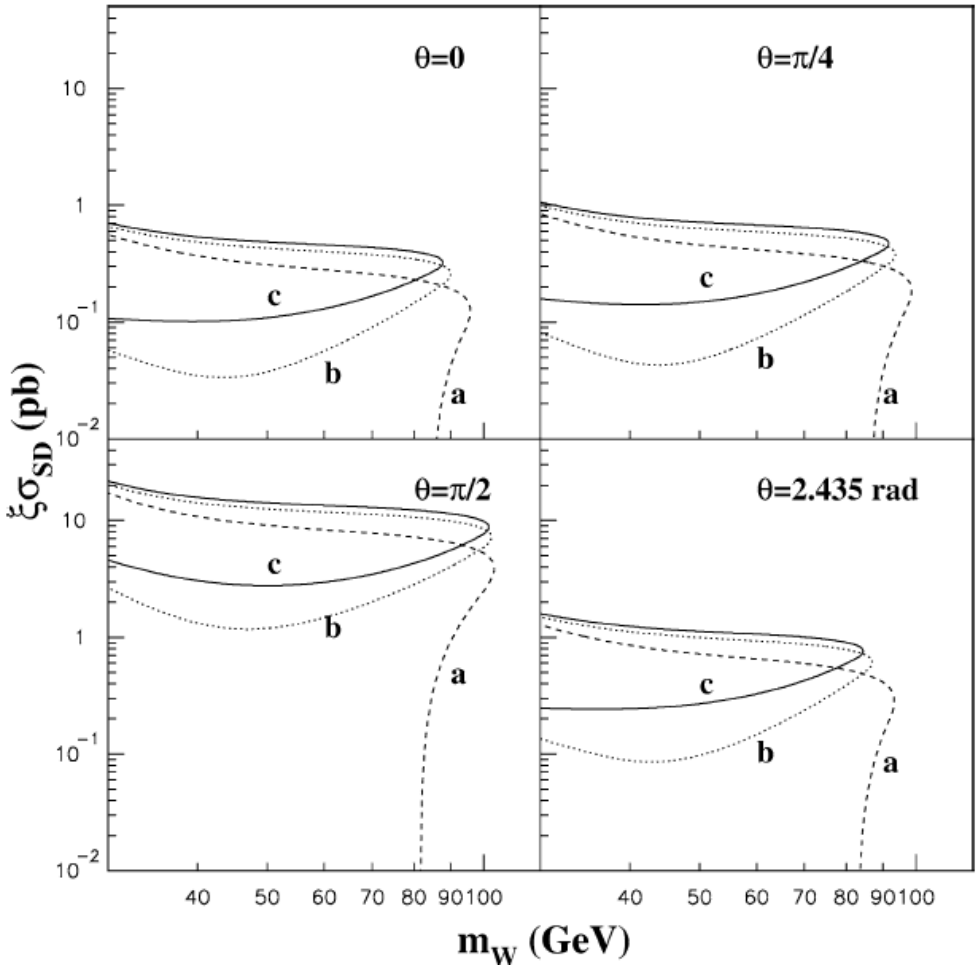

Figure 2.7: 3σ C.L. allowed region for a SD-SI mixed coupled candidates. The allowed $\xi\sigma^{\mathrm{SD}}_{\chi-\mathrm{p}}$ is plotted in function of the neutralino mass with the assumptions of (a) $\xi\sigma^{\mathrm{SI}}_{\chi-\mathrm{p}} = 3\times10^{-6}$pb, (b) $\xi\sigma^{\mathrm{SI}}_{\chi-\mathrm{p}} = 1\times10^{-6}$pb, (c) $\xi\sigma^{\mathrm{SI}}_{\chi-\mathrm{p}} = 5\times10^{-8}$pb. For simplicity, the calculation have been performed fixing $v_0 = 220$km/s and the quenching factors and the parameters of the SI and SD nuclear form factors at their mean values. $\xi = \rho_{\mathrm{D}}/(0.3\mathrm{GeVc^{-2}cm^{-3}})$ is the dimensionless dark matter density parameter. $a_{\mathrm{n}}/a_{\mathrm{p}} = \tan\theta$ is the parameter that expresses the dark matter composition, where a_{n} and a_{p} are the effective neutralino-nucleon couplings. $\theta = 0$ expresses $|a_{\mathrm{p}}| \gg |a_{\mathrm{n}}|$, $\theta = \pi/4$ expresses $a_{\mathrm{p}} = a_{\mathrm{n}}$, $\theta = \pi/2$ expresses $|a_{\mathrm{p}}| \ll |a_{\mathrm{n}}|$, $\theta = 2.435$ rad expresses $a_{\mathrm{n}}/a_{\mathrm{p}} = -0.85$, pure Z^0 coupling. This figure is taken from Ref. [31].

will reach the detectors placed at the surface of the Earth. The muon neutrinos will undergo a charged current interactions in the rocks below the detector or within the detector materials. Thus neutralinos are indirectly detectable as upward-going muons. Several experiments are undergoing[33, 34] and have set limits to the flux of the upward going muon from the Earth, Sun and Galactic center. Though there are some attempts to compare these indirect search results with the direct search results[35], they are highly model-dependent. Therefore, direct and indirect detection are both needed for the study of the neutralinos.

annihilation channel
$\bar{f}f$
W^+W^-
Z^0Z^0
W^+H^-, W^-H^+
Z^0A^0
Z^0H^0, Z^0h^0
$A^0A^0, H^0H^0, h^0h^0, H^0h^0$
A^0H^0, A^0h^0
H^+H^-
gg
$\gamma\gamma$

Table 2.2: Neutralino-neutralino annihilation channels[18].

2.4.3 Search by Accelerator Experiments

The neutralino search is also performed by accelerator experiments[36]. Neutralinos could be produced in the e^+e^- collider by the reaction

$$e^+e^- \rightarrow Z \rightarrow \chi_1\chi_2 \text{ or } \chi_2\chi_2 \tag{2.8}$$

where χ_1 is the lightest neutralino and χ_2 is the second lightest neutralino. In this thesis we usually refer to χ_1 as χ. χ_2 decays via

$$\chi_2 \rightarrow \chi_1 Z^* \rightarrow \chi f\bar{f} \text{ or } \chi_2 \rightarrow \chi_1\gamma. \tag{2.9}$$

The signature is the missing energy due to the undetected χ_1 and one or two photons, two or four leptons, or one to four hadronic jets.

Constrained Minimal Supersymmetric Standard Model(CMSSM) motivated by Grand Unified Theory(GUT) is often used for the analysis to simplify the physics interpretation. The absolute lower limit to M_{χ_1} mass for a certain parameter sets is 31.6GeVc^{-2}[1]. However, searches for neutralino with mass lighter than 30 GeVc^{-2} are still needed because it is

probable that GUT may not work and in that case, neutralinos with masses of a few $GeVc^{-2}$ can exist[37].

Chapter 3

Direct Detection of Neutralino

In this section, the theoretical framework of the direct detection of neutralinos is described[38]. Typical expression of the differential energy spectra expected by the neutralino-nucleus elastic scattering is

$$\frac{dR(0,\infty)}{dE_{\mathrm{R}}} = \frac{R_0}{E_0 r} e^{-E_{\mathrm{R}}/E_0 r} \tag{3.1}$$

where $R(0,\infty)$ is the observed event rate for the Earth(target) velocity relative to the neutralino sea $v_{\mathrm{E}} = 0$ and the local galactic escape velocity $v_{\mathrm{esc}} = \infty$, E_{R} is the recoil energy, R_0 is the total event rate for $v_{\mathrm{E}} = 0$ and $v_{\mathrm{esc}} = \infty$, E_0 is the kinetic energy of a neutralino with mass M_χ and most probable velocity v_0, and r is the kinematic factor

$$r = \frac{4 M_\chi M_{\mathrm{N}}}{(M_\chi + M_{\mathrm{N}})^2} \tag{3.2}$$

for a target nucleus with mass $M_{\mathrm{N}} = 0.932A$ GeVc^{-2}, where A is the target atomic mass in units of AMU. Eq. (3.1) for $v_{\mathrm{E}} \neq 0$ and $v_{\mathrm{esc}} \neq \infty$ is

$$\frac{dR(v_{\mathrm{E}}, v_{\mathrm{esc}})}{dE_{\mathrm{R}}} = S(E_{\mathrm{R}}, R_0(\sigma_{\chi-\mathrm{N}} F^2(E_{\mathrm{R}})), v_{\mathrm{E}}, v_{\mathrm{esc}}) \tag{3.3}$$

where S is the modified spectral function taking account of astrophysical factors, $\sigma_{\chi-\mathrm{N}}$ is the cross section at zero momentum transfer, $F^2(E_{\mathrm{R}})$ is the form factor that reveals the finite size of the nucleus. Each term of Eq.(3.3) is discussed in the following sections.

The differential rate of the event and the background is often expressed in unit of 1 count $\cdot$ keV^{-1} $\cdot$ kg^{-1}day^{-1} and we refer to this simply as the 'differential rate unit'(dru)[38]. Integrated over energy, the unit for total rate is 1 count $\cdot$ kg^{-1}day^{-1}, which we refer to as 'total rate unit'(tru)[38]. The unit for integral of the differential spectrum between selected values of energy is also 1 count $\cdot$ kg^{-1}day^{-1}, but we refer to as 'integrated rate unit'(iru) to distinguish it from tru.

3.1 R_0: Total Event Rate

The event rate per kg of a target is

$$dR = \frac{1000}{\mathrm{kg}} \frac{N_0}{A} \sigma_{\chi-\mathrm{N}} v dn \tag{3.4}$$

where N_0 is the Avogadro number ($6.02 \cdot 10^{23}\mathrm{mol}^{-1}$), n is the dark matter particle number density, v is the dark matter velocity, and $\sigma_{\chi-\mathrm{N}}$ is the neutralino-nucleus($\chi - \mathrm{N}$) cross section for zero momentum transfer. The cross section for non-zero momentum transfer scattering, $\sigma_{\chi-\mathrm{N(non-zero)}}$ is expressed as

$$\sigma_{\chi-\mathrm{N(non-zero)}} = \sigma_{\chi-\mathrm{N}} F^2(E_\mathrm{R}), \tag{3.5}$$

which is discussed later in Section 3.4. Total rate R is then expressed as

$$R = \frac{1000}{\mathrm{kg}} \frac{N_0}{A} \sigma_{\chi-\mathrm{N}} \int v dn = \frac{1000}{\mathrm{kg}} \frac{N_0}{A} \sigma_{\chi-\mathrm{N}} n_0 \langle v \rangle \tag{3.6}$$

where n_0 is the mean dark matter particle number density and $\langle v \rangle$ is the mean dark matter velocity. Maxwellian dark matter velocity distribution:

$$f(\vec{v}, \vec{v_\mathrm{E}}) = e^{-|\vec{v}+\vec{v_\mathrm{E}}|^2/v_0^2}. \tag{3.7}$$

with the velocity of the dark matter $\vec{v}$ is commonly assumed. For $v_\mathrm{E} = 0$ and $v_\mathrm{esc} = \infty$, $\langle v \rangle$ is expressed as

$$\langle v \rangle = \frac{2}{\sqrt{\pi}} v_0. \tag{3.8}$$

From Eq. (3.6) and Eq. (3.8), R_0 is written as

$$R_0 = \frac{1000}{\mathrm{kg}} \frac{N_0}{A} \sigma_{\chi-\mathrm{N}} \frac{\rho_\mathrm{D}}{M_\chi} \frac{2}{\sqrt{\pi}} v_0 \tag{3.9}$$

where $n_0 = \rho_\mathrm{D}/M_\chi$ is the mean dark matter particle number density, ρ_D is the dark matter density described in Section 1.1.2, R_0 is conventionally expressed in units of $\mathrm{kg}^{-1}\mathrm{day}^{-1}$. Normalized to $\rho_\mathrm{D} = 0.3\mathrm{GeVc}^{-2}\mathrm{cm}^{-3}$ and v_0=230km s^{-1}, Eq.(3.9) becomes

$$R_0 = \frac{377}{M_\chi M_\mathrm{N}} \left(\frac{\sigma_{\chi-\mathrm{N}}}{1\mathrm{pb}} \right) \left(\frac{\rho_\mathrm{D}}{0.3\mathrm{GeVc}^{-2}\mathrm{cm}^{-3}} \right) \left(\frac{v_0}{230\mathrm{km\,s}^{-1}} \right). \tag{3.10}$$

with M_χ, M_N in units of GeVc^{-2}.

3.2 S: Modified Spectral Function

Total count rate for $v_{\rm E} \neq 0$ and $v_{\rm esc} \neq \infty$ is expressed using Eq. (3.6) and Eq. (3.9).

$$R = R_0 \frac{\sqrt{\pi}}{2} \frac{\langle v \rangle}{v_0} = R_0 \frac{k_0}{k} \frac{1}{2\pi v_0^4} \int v f(\vec{v}, \vec{v}_{\rm E}) d^3\vec{v} \tag{3.11}$$

where k is the normalization constant

$$k = \int_0^{2\pi} d\phi \int_{-1}^{+1} d(\cos\theta) \int_0^{v_{\rm esc}} f(\vec{v}, \vec{v_{\rm E}}) v^2 dv, \tag{3.12}$$

$k_0 = (\pi v_0^2)^{3/2}$ is the value of k in Eq. (3.12) for $v_{\rm esc} = \infty$. Eq. (3.11) is then written as

$$\frac{R(0, v_{\rm esc})}{R_0} = \frac{k_0}{k_1} \left[1 - \left(1 + \frac{v_{\rm esc}^2}{v_0^2} \right) e^{-v_{\rm esc}^2/v_0^2} \right] \tag{3.13}$$

$$\frac{R(v_{\rm E}, \infty)}{R_0} = \frac{1}{2} \left[\pi^{1/2} \left(\frac{v_{\rm E}}{v_0} + \frac{1}{2} \frac{v_0}{v_{\rm E}} \right) {\rm erf} \left(\frac{v_{\rm E}}{v_0} \right) + e^{-v_E^2/v_0^2} \right] \tag{3.14}$$

$$\frac{R(v_{\rm E}, v_{\rm esc})}{R_0} = \frac{k_0}{k_1} \left[\frac{R(v_{\rm E}, \infty)}{R_0} - (\frac{v_{\rm esc}^2}{v_0^2} + \frac{1}{3} \frac{v_E^2}{v_0^2} + 1) e^{-v_{esc}^2/v_0^2} \right] \tag{3.15}$$

where ${\rm erf}(x) = 2/\sqrt{\pi} \int_0^x \exp(-t^2) dt$ is the error function and k_1 is the value of k for finite value of $v_{\rm esc}$ and written as

$$k_1 = k_0 \left[{\rm erf} \left(\frac{v_{\rm esc}}{v_0} \right) - \frac{2}{\sqrt{\pi}} \frac{v_{\rm esc}}{v_0} e^{-v_{\rm esc}^2/v_0^2} \right] \tag{3.16}$$

Recoil energy $E_{\rm R}$ of a nucleus struck by a dark matter particle of kinetic energy E, scattered at angle θ(in center-of-mass) is[38].

$$E_{\rm R} = Er(1 - \cos\theta)/2 \tag{3.17}$$

where r is defined in Eq. (3.2). With an assumption that the scattering is isotropic, where recoils are uniformly distributed in $E_{\rm R}$ over the range $0 \leq E_{\rm R} \leq Er$

$$\frac{dR}{dE_{\rm R}} = \int_{E_{\rm min}}^{E_{\rm max}} \frac{1}{Er} dR(E) = \frac{1}{E_0 r} \int_{v_{\rm min}}^{v_{\rm max}} \frac{v_0^2}{v^2} dR(v) \tag{3.18}$$

where $E_{\rm min}$ and $E_{\rm max}$ are minimum and maximum of the kinematic energies of the dark matter that gives recoil energy of $E_{\rm R}$, and $v_{\rm min}$ and $v_{\rm max}$ are dark matter velocities corresponding to $E_{\rm min}$ and $E_{\rm max}$, respectively, where $E_{\rm min} = E_{\rm R}/r$ and $v_{\rm min} = (2E_{\rm min}/M_{\rm D})^{1/2} = (E_{\rm R}/E_0 r)^{1/2} v_0$.

Using Eq.(3.18) and the differential form of Eq.(3.11) we have:

$$dR = R_0 \frac{k_0}{k} \frac{1}{2\pi v_0^4} v f(\vec{v}, \vec{v}_{\rm E}) d^3 v, \tag{3.19}$$

then the differential spectral function is

$$\frac{dR}{dE_{\rm R}} = \frac{R_0}{E_0 r}\frac{k_0}{k}\frac{1}{2\pi v_0^2}\int_{v_{\rm min}}^{v_{\rm max}}\frac{1}{v}f(\vec{v},\vec{v}_{\rm E})d^3v \tag{3.20}$$

From Eq.(3.20), unmodified spectrum of Eq.(3.1) is obtained.

$$\begin{aligned}
\frac{dR(0,v_{\rm esc})}{dE_{\rm R}} &= \frac{k_0}{k_1}\frac{R_0}{E_0 r}(e^{-E_{\rm R}/E_0 r} - e^{-v_{\rm esc}^2/v_0^2}) \\
&= \frac{k_0}{k_1}\left[\frac{dR(0,\infty)}{dE_{\rm R}} - \frac{R_0}{E_0 r}e^{-v_{\rm esc}^2/v_0^2}\right] && (3.21)\\
\frac{dR(v_{\rm E},\infty)}{dE_{\rm R}} &= \frac{R_0}{E_0 r}\frac{\sqrt{\pi}}{4}\frac{v_0}{v_{\rm E}}\left[{\rm erf}\left(\frac{v_{\rm min}+v_{\rm E}}{v_0}\right) - {\rm erf}\left(\frac{v_{\rm min}-v_{\rm E}}{v_0}\right)\right] && (3.22)\\
&\sim c_1\frac{R_0}{E_0 r}e^{-c_2 E_{\rm R}/E_0 r} && (3.23)\\
\frac{dR(v_{\rm E},v_{\rm esc})}{dE_{\rm R}} &= \frac{k_0}{k_1}\left[\frac{dR(v_{\rm E},\infty)}{dE_{\rm R}} - \frac{R_0}{E_0 r}e^{-v_{\rm esc}^2/v_0^2}\right] && (3.24)
\end{aligned}$$

where $c_1 = 0.751$ and $c_2 = 0.561$ are parameters in Eq.(3.23).

The Earth velocity $v_{\rm E}$ varies during the year as the Earth moves around the Sun. For practical purposes,

$$v_{\rm E} \sim 244 + 15\sin(2\pi y){\rm km\,s^{-1}} \tag{3.25}$$

where y is the elapsed time from March 2nd in years, is used.

The escape velocity $v_{\rm esc}$ is discussed by several authors [48, 49] and

$$625{\rm km\,s^{-1}} > v_{\rm esc} > 475{\rm km\,s^{-1}} \tag{3.26}$$

is the commonly used value. Expected spectra by 1kg LiF for $M_\chi = 30{\rm GeVc^{-2}}$ and $M_\chi = 100{\rm GeVc^{-2}}$ are shown in Fig. 3.1.

3.3 $\sigma_{\chi-{\rm N}}$: Cross Section at Zero Momentum Transfer

Neutralinos could interact with quarks spin-independently(SI) and spin-dependently(SD). The cross section related to each interaction can be calculated by assuming certain sets of parameters in MSSM model[18, 39].

3.3.1 Theoretical Framework

The MSSM Lagrangian leads to an effective Lagrangian $\mathcal{L}$ which describes the low energy neutralino-quark interaction. [39]

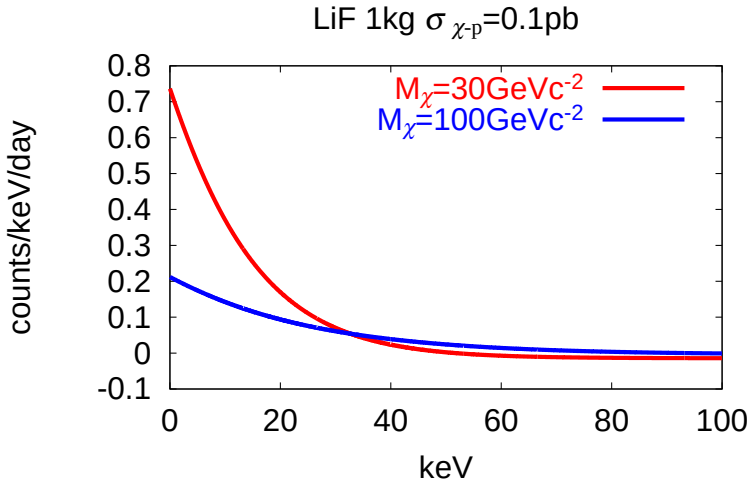

Figure 3.1: Expected spectra by 1kg LiF for $M_\chi = 30\text{GeVc}^{-2}$ and $M_\chi = 100\text{GeVc}^{-2}$. Here, $\sigma^{\text{SD}}_{\chi-\text{p}}$=0.1pb and odd group shell model are assumed. We take v_0=230km/s, v_{E}=244km/s, and v_{esc}=475km. We used Eq. (3.24) for the calculation.

$$\begin{aligned}\mathcal{L} &= \overline{\chi}\gamma^\mu\gamma^5\chi\overline{Q}_{q_i}\gamma_\mu(\alpha_{1(q_i)}+\alpha_{2(q_i)}\gamma^5)Q_{q_i}+\alpha_{3(q_i)}\overline{\chi}\chi\overline{Q}_{q_i}Q_{q_i}\\ &\quad +\alpha_{4(q_i)}\overline{\chi}\gamma^5\chi\overline{Q_{q_i}}\gamma^5Q_{q_i}+\alpha_{5(q_i)}\overline{\chi}\chi\overline{Q}_{q_i}\gamma^5Q_{q_i}+\alpha_{6(q_i)}\overline{\chi}\gamma^5\chi\overline{Q}_{q_i}Q_{q_i},\end{aligned} \tag{3.27}$$

Q_{q_i} denotes the quark and the subscript q_i show the quark type; the subscript $q = 1, 2$ denotes the quark sector(up or down) and $i = 1, 2, 3$ denotes the flavor(d, s, b or u, c, t) of the quark in that sector. Terms in Eq.(3.27) with coefficients α_2, α_3 contributes to the SD and SI interactions, respectively. Terms in Eq.(3.27) with coefficients $\alpha_1, \alpha_4, \alpha_5$, and α_6 are negligible for the dark matters with non-relativistic velocities. α_2 and α_3 are written as follows.

$$\begin{aligned}\alpha_{2(q_i)} &= \frac{1}{4(M_{q_1}^2-M_\chi^2)}[|Y_{q_1}|^2]+|X_{q_1}|^2]+\frac{1}{4(M_{q_2}^2-M_\chi^2)}[|V_{q_2}|^2]+|W_{q_2}|^2]\\ &\quad -\frac{g^2}{4M_Z^2\cos^2\theta_{\text{W}}}[|a_3|^2-|a_4|^2]\frac{T_q^3}{2}\end{aligned} \tag{3.28}$$

and

$$\alpha_{3(q_i)} = \frac{1}{2(M_{q_1}^2-M_\chi^2)}Re[(X_{q_1})(Y_{q_1})^*]-\frac{1}{2(M_{q_2}^2-M_\chi^2)}Re[(W_{q_2})(V_{q_2})^*]$$

$$-\frac{gM_{q_i}}{4M_{\rm W}B_q}[Re(\delta_{q_1}[ga_2-g'a_1])D_qC_q(-\frac{1}{M_{\rm H_1}^2}+\frac{1}{M_{\rm H_2}^2})$$
$$+Re(\delta_{q_2}[ga_2-g'a_1])(\frac{D_q^2}{M_{\rm H2}^2}+\frac{C_q^2}{M_{\rm H1}^2})] \tag{3.29}$$

where M_{q_i} is the quark mass. Eq. (3.28) and Eq. (3.29) are to be summed over q and i. M_χ is the mass of the neutralino, $M_{\rm Z}$ is the mass of the Z boson, $M_{\rm W}$ is the mass of the W boson, T_q^3 is the third component of the weak isospin, $a_{1,2,3,4}$ is the neutralino composition parameter in Eq. (2.6), $M_{\rm H_2} < M_{\rm H_1}$ denote two scalar Higgs masses, and $\theta_{\rm W}$ is the weak mixing angle, which is given by the ratio of the two weak coupling constants, $\tan\theta_{\rm W} = g'/g$.

$$\begin{aligned}
X_{q_i} &\equiv \eta_{11}^*\frac{gM_{q_i}a_{(5-q)}^*}{2M_{\rm W}B_i} - \eta_{12}^* e_q g' a_1 \\
Y_{q_i} &\equiv \eta_{11}^*(\frac{y_q}{2}g'a_1 + gT_q^3 a_2) + \eta_{12}^*\frac{gM_{q_i}a_{(5-q)}}{2M_{\rm W}B_i} \\
W_{q_i} &\equiv \eta_{12}^*\frac{gM_{q_i}a_{(5-q)}}{2M_{\rm W}B_q} - \eta_{22}^* e_q g' a_1^* \\
V_{q_i} &\equiv \eta_{22}^*\frac{gM_{q_i}a_{(5-q)}}{2M_{\rm W}B_q} + \eta_{21}^*(\frac{y_q}{2}g'a_1 + gT_q^3 a_2)
\end{aligned} \tag{3.30}$$

y_q is the hypercharge of the sfermion defined by $e_q = T_q^3 + y_q/2$. η is the sfermion mass matrix and defined by an angle θ_{q_i} as

$$\begin{pmatrix} \eta_{11} & \eta_{12} \\ \eta_{21} & \eta_{22} \end{pmatrix} = \begin{pmatrix} \cos\theta_{qi} & \sin\theta_{qi} \\ -\sin\theta_{qi} & \cos\theta_{qi} \end{pmatrix}. \tag{3.31}$$

$$\delta_{1_1} = a_3,\ \delta_{1_2} = a_4,\ \delta_{2_1} = a_4,\ \delta_{2_2} = -a_3, \tag{3.32}$$

$$A_1 = \cos\beta,\ A_2 = -\sin\beta,\ B_1 = \sin\beta,\ B_2 = \cos\beta \tag{3.33}$$
$$C_1 = \sin\beta,\ C_2 = \cos\alpha, D_1 = \cos\alpha,\ D_2 = -\sin\alpha \tag{3.34}$$

where α denotes the Higgs mixing angle, and $\tan\beta = v_2/v_1$, where v_1 and v_2 are the vacuum expectation values of the two Higgses. α and β and Higgs mass $M_{\rm H}$ are related by the following equations:

$$\sin\alpha = -\left(\frac{1-k}{2}\right)^{\frac{1}{2}},\ \cos\alpha = -\left(\frac{1+k}{2}\right)^{\frac{1}{2}} \tag{3.35}$$

where

$$k = c\left(\frac{c^2+r^2-2r}{c^2+r^2-2rc^2}\right),\ c = \cos 2\beta,\ r = \frac{M_{\rm H}^2}{M_{\rm Z}^2}. \tag{3.36}$$

3.3.2 Cross Sections

The neutralino-nucleus cross section at zero momentum transfer is expressed as

$$\sigma_{\chi-\mathrm{N}} = 4G_{\mathrm{F}}^2 \mu_{\chi-\mathrm{N}}^2 C_{\mathrm{N}} \tag{3.37}$$

where G_{F}=1.166 $\times 10^{-5}\mathrm{GeV}^{-2}(\hbar c)^3$ is the Fermi coupling constant, $\mu_{\chi-\mathrm{N}}$ is the reduced mass of the neutralino of mass $M_\chi \mathrm{GeVc}^{-2}$ and the target nucleus of mass $M_N \mathrm{GeVc}^{-2}$:

$$\mu_{\chi-\mathrm{N}} = \frac{M_\chi M_{\mathrm{N}}}{M_\chi + M_{\mathrm{N}}}. \tag{3.38}$$

C_{N} is a dimensionless number referred to as enhancement factor that carries all the particle physics model information. It is expressed by the sum of SI and SD terms:

$$C_{\mathrm{N}} = (C_{\mathrm{N}}^{\mathrm{SI}} + C_{\mathrm{N}}^{\mathrm{SD}}). \tag{3.39}$$

In the following sections, $C_{\mathrm{N}}^{\mathrm{SI}}$ and $C_{\mathrm{N}}^{\mathrm{SD}}$ values are discussed for various nuclei. Since $\sigma_{\chi-\mathrm{N}}$ can be expressed as

$$\sigma_{\chi-\mathrm{N}} = \sigma_{\chi-\mathrm{p}} \frac{\mu_{\chi-\mathrm{N}}^2}{\mu_{\chi-\mathrm{p}}^2} \frac{C_{\mathrm{N}}}{C_{\mathrm{p}}} = \sigma_{\chi-\mathrm{n}} \frac{\mu_{\chi-\mathrm{N}}^2}{\mu_{\chi-\mathrm{n}}^2} \frac{C_{\mathrm{N}}}{C_{\mathrm{n}}} \tag{3.40}$$

with the enhancement factor of proton C_{p} and C_{n}, we can convert the experimental result $\sigma_{\chi-\mathrm{N}}$ to $\sigma_{\chi-\mathrm{p}}$ or $\sigma_{\chi-\mathrm{n}}$ with the enhancement factors $C_{\mathrm{N}}^{\mathrm{SI}}$ and $C_{\mathrm{N}}^{\mathrm{SD}}$. Here $\sigma_{\chi-\mathrm{p}}$ and $\sigma_{\chi-\mathrm{n}}$ are neutralino-proton and neutralino-neutron cross sections, respectively.

3.3.3 Spin-Independent Interaction

The enhancement factor of the SI cross section is written as[39]

$$C_{\mathrm{N}}^{\mathrm{SI}} = \frac{1}{\pi G_{\mathrm{F}}^2} [Z f^{(\mathrm{p})} + (A - Z) f^{(\mathrm{n})}]^2 \tag{3.41}$$

where Z is the atomic number. $f^{(\mathrm{p})}$ and $f^{(\mathrm{n})}$ are the nucleon-neutralino spin-independent couplings. They are written as the sum of quark-neutralino spin-independent coupling $f_{Tq_i}^{(p)}$ and $f_{Tq_i}^{(n)}$ over the quarks that comprise the nucleon:

$$\frac{f^{(\mathrm{p})}}{M_{\mathrm{p}}} = \sum_{q_i=\mathrm{u,d,s}} f_{\mathrm{T}q_i}^{(\mathrm{p})} \frac{\alpha_{3(q_i)}}{M_{q_i}} + \frac{2}{27} f_{\mathrm{TG}}^{(\mathrm{p})} \sum_{q_i=\mathrm{c,b,t}} \frac{\alpha_{3(q_i)}}{M_{q_i}} \tag{3.42}$$

$$\frac{f^{(\mathrm{n})}}{M_{\mathrm{n}}} = \sum_{q_i=\mathrm{u,d,s}} f_{\mathrm{T}q_i}^{(\mathrm{n})} \frac{\alpha_{3(q_i)}}{M_{q_i}} + \frac{2}{27} f_{\mathrm{TG}}^{(\mathrm{n})} \sum_{q_i=\mathrm{c,b,t}} \frac{\alpha_{3(q_i)}}{M_{q_i}} \tag{3.43}$$

where M_{q_i} is the quark mass, $M_{\rm p}$ and $M_{\rm n}$ are the proton and neutron masses, respectively. Parameters $f^{(\rm p)}_{{\rm T}q_i}$ and $f^{(\rm n)}_{{\rm T}q_i}$ are determined by the information of quark mass ratio and chiral symmetry applied to baryons. The values of $f^{(\rm p)}_{{\rm T}q_i}$ and $f^{(\rm n)}_{{\rm T}q_i}$ are as follows:

$$\begin{aligned} f^{(\rm p)}_{\rm Tu} &= 0.020 \pm 0.004, f^{(\rm p)}_{\rm Td} = 0.026 \pm 0.005, f^{(\rm p)}_{\rm Ts} = 0.118 \pm 0.062 \\ f^{(\rm n)}_{\rm Tu} &= 0.014 \pm 0.003, f^{(\rm n)}_{\rm Td} = 0.036 \pm 0.008, f^{(\rm n)}_{\rm Ts} = 0.118 \pm 0.062 \end{aligned} \tag{3.44}$$

while

$$f^{(\rm p)}_{\rm TG} = 1 - \sum_{q_i={\rm u,d,s}} f^{(\rm p)}_{{\rm T}q_i} \tag{3.45}$$

$$f^{(\rm n)}_{\rm TG} = 1 - \sum_{q_i={\rm u,d,s}} f^{(\rm n)}_{{\rm T}q_i}. \tag{3.46}$$

The difference between $f^{(\rm p)}_{\rm Tq}$ and $f^{(\rm n)}_{\rm Tq}$ is small in most cases, therefore $C^{\rm SI}_{\rm N} \propto A^2$:

$$\frac{C^{\rm SI}_{\rm N}}{C^{\rm SI}_{\rm p}} = \frac{C^{\rm SI}_{\rm N}}{C^{\rm SI}_{\rm n}} = A^2 \tag{3.47}$$

is a practical estimation. Eq. (3.40) and Eq.(3.47) give

$$\sigma^{\rm SI}_{\chi-{\rm p}} = \sigma^{\rm SI}_{\chi-{\rm N}} \frac{\mu^2_{\chi-{\rm p}}}{\mu^2_{\chi-{\rm N}}} \frac{1}{A^2}. \tag{3.48}$$

Eq. (3.48) can be used for the conversion of the obtained $\sigma^{\rm SI}_{\chi-{\rm N}}$ into $\sigma^{\rm SI}_{\chi-{\rm p}}$.

If Dirac neutrinos are assumed, in which case neutrons dominate the cross sections,

$$\frac{C^{\rm SI}_{\rm N}}{C^{\rm SI}_{\rm n}} = (A-Z)^2 \tag{3.49}$$

should be used instead. Eq. (3.40) and Eq.(3.49) give

$$\sigma^{\rm SI}_{\chi-{\rm p}} = \sigma^{\rm SI}_{\chi-{\rm N}} \frac{\mu^2_{\chi-{\rm p}}}{\mu^2_{\chi-{\rm N}}} \frac{1}{(A-Z)^2}. \tag{3.50}$$

Eq. (3.47) and Eq. (3.49) indicate that materials with large A values are effective for SI interacting neutralino detection.

3.3.4 Spin-Dependent Interactions

The enhancement factor of the SD cross section is written as[39]

$$C^{\rm SD}_{\rm N} = \frac{8}{\pi}(a_{\rm p}\langle S_{\rm p(N)}\rangle + a_{\rm n}\langle S_{\rm n(N)}\rangle)^2 \frac{J+1}{J} \tag{3.51}$$

where $\langle S_{\mathrm{p(N)}}\rangle$ and $\langle S_{\mathrm{n(N)}}\rangle$ are the expectation value of the proton and neutron spins in the nucleus N, and a_{p} and a_{n} are the neutralino-nucleon spin-dependent couplings, and J is the total spin of the nucleus. a_{p} and a_{n} are expressed as

$$a_{\mathrm{p}} = \sum_{q_i=u,d,s} \frac{\alpha_{2(q_i)}}{\sqrt{2}G_{\mathrm{F}}}\Delta^{\mathrm{p}}_{q_i} \tag{3.52}$$

$$a_{\mathrm{n}} = \sum_{q_i=u,d,s} \frac{\alpha_{2(q_i)}}{\sqrt{2}G_{\mathrm{F}}}\Delta^{\mathrm{n}}_{q_i} \tag{3.53}$$

$\Delta^{\mathrm{p}}_{q_i}$ and $\Delta^{\mathrm{n}}_{q_i}$ are the quark spin content of the nucleon and are calculated as[39],

$$\Delta^{\mathrm{p}}_{u} = 0.78 \pm 0.02,\ \Delta^{\mathrm{p}}_{d} = -0.48 \pm 0.02,\ \Delta^{\mathrm{p}}_{s} = -0.15 \pm 0.02 \tag{3.54}$$

in the case of neutron, we have $\Delta^{\mathrm{n}}_{\mathrm{u}} = \Delta^{\mathrm{p}}_{\mathrm{d}}$, $\Delta^{\mathrm{n}}_{\mathrm{d}} = \Delta^{\mathrm{p}}_{\mathrm{u}}$, $\Delta^{\mathrm{n}}_{\mathrm{s}} = \Delta^{\mathrm{p}}_{\mathrm{s}}$. Eq.(3.51) is written as

$$C^{\mathrm{SD}}_{\mathrm{N}} = \frac{8}{\pi}\lambda^2 J(J+1) \tag{3.55}$$

where

$$\lambda \equiv \frac{1}{J}(a_{\mathrm{p}}\langle S_{\mathrm{p(N)}}\rangle + a_{\mathrm{n}}\langle S_{\mathrm{n(N)}}\rangle). \tag{3.56}$$

λ is referred to as Landé factor. $\lambda^2 J(J+1)$ values calculated on the basis of the single particle model and the odd group model for various nuclei are listed in Table 3.1. In the single particle model, only the unpaired nucleon is considered, while all nucleons of the same type as the unpaired nucleon are taken account of in the odd group model.

Eq. (3.40) and Eq.(3.55) give

$$\begin{aligned}
\sigma^{\mathrm{SD}}_{\chi-\mathrm{p}} &= \sigma^{\mathrm{SD}}_{\chi-\mathrm{N}}\frac{\mu^2_{\chi-\mathrm{p}}}{\mu^2_{\chi-\mathrm{N}}}\frac{0.75}{\lambda^2 J(J+1)} \\
\sigma^{\mathrm{SD}}_{\chi-\mathrm{n}} &= \sigma^{\mathrm{SD}}_{\chi-\mathrm{N}}\frac{\mu^2_{\chi-\mathrm{n}}}{\mu^2_{\chi-\mathrm{N}}}\frac{0.75}{\lambda^2 J(J+1)}.
\end{aligned} \tag{3.57}$$

where we ignored the contribution of the spins by the nuclei that are not the same type as the unpaired nucleon.

3.3.5 Combining the Results of More Than Two Elements

For a target with two or more elements N_i, total observed count rate R is expressed as

$$R = R'\sigma_{\mathrm{lim}\chi-\mathrm{p}}\sum_{\mathrm{N}_i} f_{\mathrm{N}_i}\mathrm{C}_{\mathrm{N}_i}F^2_{\mathrm{N}_i} \tag{3.58}$$

where f_{N_i} is the mass fraction of the component N_i, $\mathrm{C}_{\mathrm{N}_i}$ is the enhancement factor, $F^2_{\mathrm{N}_i}$ is the form factor, and R' carries other information on the count rate that is independent of N_i. From Eq. (3.58), $\sigma_{\mathrm{lim}\chi-\mathrm{p}}$ is obtained as

(a)unpaired proton				
			$\lambda^2 J(J+1)$	
Isotope	J	Abundance(%)	Odd group	Single particle
^{1}H	1/2	100	0.750	0.750
^{7}Li	3/2	92.5	0.411	0.417
^{19}F	1/2	100	0.647	0.75
^{23}Na	3/2	100	0.041	0.35
^{27}Al	5/2	100	0.087	0.35
^{35}Cl	3/2	75.8	0.036	0.15
^{51}V	7/2	99.8	0.167	0.321
^{69}Ga	3/2	60.1	0.021	0.417
^{71}Ga	3/2	39.9	0.089	0.417
^{75}As	3/2	100	0.000	0.417
^{93}Nb	9/2	100	0.162	0.306
^{107}Ag	1/2	57.8	0.054	0.083
^{109}Ag	1/2	48.2	0.057	0.083
^{127}I	5/2	100	0.023	0.250

(b)unpaired neutron				
			$\lambda^2 J(J+1)$	
Isotope	J	Abundance(%)	Odd group	Single particle
^{3}He	1/2	1.3×10^{-4}	0.928	0.750
^{29}Si	1/2	4.7	0.063	0.750
^{67}Zn	5/2	4.1	0.073	0.179
^{73}Ge	9/2	7.8	0.065	0.306
^{99}Ru	5/2	12.7	0.039	0.350
^{101}Ru	5/2	17.0	0.049	0.350
^{111}Cd	1/2	12.8	0.072	0.750
^{113}Cd	1/2	12.2	0.079	0.750
^{115}Sn	1/2	0.4	0.173	0.750
^{117}Sn	1/2	7.7	0.205	0.750
^{129}Xe	1/2	26.4	0.124	0.750
^{131}Xe	3/2	21.2	0.055	0.150

Table 3.1: Values of $\lambda^2 J(J+1)$ for various isotopes[40, 41]. In the single particle model, only the unpaired nucleon is considered, while all nucleons of the same type as the unpaired nucleon are taken account of in the odd group model.

$$\sigma_{\mathrm{lim}\chi-\mathrm{p}} = \frac{R}{R'} \frac{1}{\sum_{\mathrm{N}_i} f_{\mathrm{N}_i} \mathrm{C}_{\mathrm{N}_i} F^2_{\mathrm{N}_i}} \tag{3.59}$$

If we calculate the limit assuming that all events are due to N_i, we have the following limit:

$$\sigma_{\mathrm{lim}\chi-\mathrm{p}(\mathrm{N_i})} = \frac{R}{R'} \frac{1}{f_{\mathrm{N}_i} \mathrm{C}_{\mathrm{N}_i} F^2_{\mathrm{N}_i}}. \tag{3.60}$$

Using Eq. (3.59) and Eq. (3.60), we have the relation between the neutralino-proton cross section limit $\sigma_{\mathrm{lim}\chi-\mathrm{p}}$ and the limit obtained from the N_i signal as:

$$\frac{1}{\sigma_{\mathrm{lim}\chi-\mathrm{p}(\mathrm{N})}} = \sum_{\mathrm{N}_i} \frac{1}{\sigma_{\mathrm{lim}\chi-\mathrm{p}(\mathrm{N}_i)}}. \tag{3.61}$$

3.3.6 Model Independent Method for the Spin-Dependent Interactions

Using the $\lambda^2 J(J+1)$ values listed in Table 3.1 is a convenient way to compare various experimental results as long as unpaired nucleons are those of the same type and this method has been used in most cases. However, there arise problems when comparing proton-odd(^{19}F, ^{23}Na, ^{27}Al, ^{127}I, ...) and neutron-odd(^{73}Ge, ^{129}Xe,...) targets. Because the ratio $\sigma^{\mathrm{SD}}_{\chi-\mathrm{p}}/\sigma^{\mathrm{SD}}_{\chi-\mathrm{n}}$ are not of the order of unity, when we deal with gaugino-like neutralinos. Here, $\sigma^{\mathrm{SD}}_{\chi-\mathrm{p}}$ and $\sigma^{\mathrm{SD}}_{\chi-\mathrm{n}}$ are spin-dependent neutralino-proton and neutralino-neutron cross sections, respectively. Current method with assuming $\sigma^{\mathrm{SD}}_{\chi-\mathrm{p}}/\sigma^{\mathrm{SD}}_{\chi-\mathrm{n}} = 1$ or $\sigma^{\mathrm{SD}}_{\chi-\mathrm{p}}/\sigma^{\mathrm{SD}}_{\chi-\mathrm{n}} = 2$[38] that are true for higgsino-like neutralinos, would sometimes derive too optimistic result for gaugino-like neutralinos. The ratio for the gaugino-like neutralinos is highly model-dependent and can vary by several orders of magnitude. Fig. 3.2 shows the ratio of $\sigma^{\mathrm{SD}}_{\chi-\mathrm{p}}/\sigma^{\mathrm{SD}}_{\chi-\mathrm{n}}$ in function of the neutralino composition.

D.R. Tovey *et al.* suggested a new method which makes model independent comparison of different experiments possible[42]. With this method, one can derive a model independent results on

- Limits to $\sigma^{\mathrm{SD}}_{\chi-\mathrm{p}}$ and $\sigma^{\mathrm{SD}}_{\chi-\mathrm{n}}$ as a function of M_χ
- Limits in the $\sigma^{\mathrm{SD}}_{\chi-\mathrm{p}} - \sigma^{\mathrm{SD}}_{\chi-\mathrm{n}}$ plane
- Limits in the a_{p}-a_{n} plane

We will show how these results are derived model independently in the following.

- Limits to $\sigma^{\mathrm{SD}}_{\chi-\mathrm{p}}$ and $\sigma^{\mathrm{SD}}_{\chi-\mathrm{n}}$
  In general, $a_{\mathrm{p}}\langle S_{\mathrm{p(N)}}\rangle$ and $a_{\mathrm{n}}\langle S_{\mathrm{n(N)}}\rangle$ can be in opposite sign and similar magnitude, therefore, Eq. (3.51) is to be written as

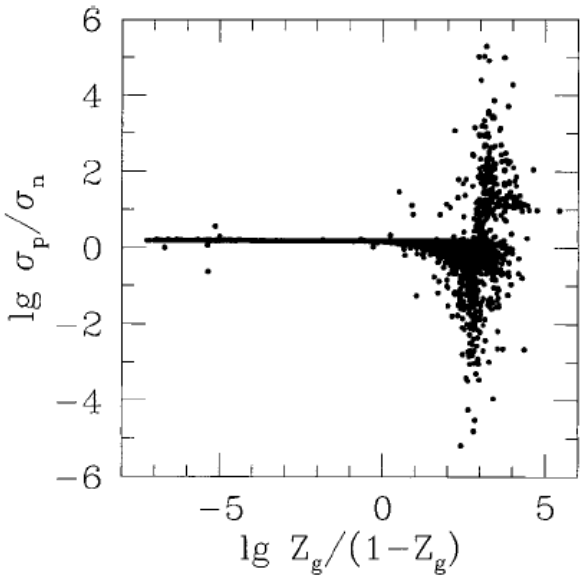

Figure 3.2: The ratio $\sigma^{\rm SD}_{\chi-{\rm p}}/\sigma^{\rm SD}_{\chi-{\rm n}}$ (referred to as $\sigma_{\rm p}/\sigma_{\rm n}$ in the figure.) plotted against neutralino composition $Z_{\rm g}/(1-Z_{\rm g})$. Here $Z_{\rm g}$ is the gaugino fraction. Small values of $Z_{\rm g}/(1-Z_{\rm g})$ correspond to higgsino-like neutralinos and large values correspond to gaugino-like neutralinos. This figure is taken from Ref. [42].

$$C^{\rm SD}_{\rm N} = \frac{8}{\pi}(|a_{\rm p}\langle S_{\rm p(N)}\rangle| \pm |a_{\rm n}\langle S_{\rm n(N)}\rangle|)^2\frac{J+1}{J} \tag{3.62}$$

in a more proper way. Eq. (3.62) shows that spin-dependent enhancement factor $C^{\rm SD}_{\rm N}$ can be reduced for some types of neutralinos and in that case some of the limit would be too optimistic. As protons and neutrons have their own contributions to the nucleus spin, their own spin-dependent enhancement factor are written as:

$$\begin{aligned} C^{\rm SD}_{\rm p(N)} &= \frac{8}{\pi}(a_{\rm p}\langle S_{\rm p(N)}\rangle)^2\frac{J+1}{J} \\ C^{\rm SD}_{\rm n(N)} &= \frac{8}{\pi}(a_{\rm n}\langle S_{\rm n(N)}\rangle)^2\frac{J+1}{J}. \end{aligned} \tag{3.63}$$

We write proton and neutron contribution to the spin-dependent enhancement factor of nucleus N as $C^{\rm SD}_{\rm p(N)}$ and $C^{\rm SD}_{\rm n(N)}$. Eq. (3.63) and Eq. (3.62) gives

$$C^{\rm SD}_{\rm N} = (\sqrt{C^{\rm SD}_{\rm p(N)}} \pm \sqrt{C^{\rm SD}_{\rm n(N)}})^2 \tag{3.64}$$

$C^{\rm SD}_{\rm p(N)}/C^{\rm SD}_{\rm p}$ and $C^{\rm SD}_{\rm n(N)}/C^{\rm SD}_{\rm n}$ values can be calculated as:

$$\begin{aligned}
\frac{C^{\rm SD}_{\rm p(N)}}{C^{\rm SD}_{\rm p}} &= \frac{\frac{8}{\pi}(a_{\rm p}\langle S_{\rm p}\rangle)^2 \frac{\frac{1}{2}+1}{\frac{1}{2}}}{\frac{8}{\pi}(a_{\rm p}\frac{1}{2})^2 \frac{\frac{1}{2}+1}{\frac{1}{2}}} = \frac{4}{3}\langle S_{\rm p(N)}\rangle^2 \frac{J+1}{J} \\
\frac{C^{\rm SD}_{\rm p(N)}}{C^{\rm SD}_{\rm n}} &= \frac{\frac{8}{\pi}(a_{\rm n}\langle S_{\rm n}\rangle)^2 \frac{\frac{1}{2}+1}{\frac{1}{2}}}{\frac{8}{\pi}(a_{\rm n}\frac{1}{2})^2 \frac{\frac{1}{2}+1}{\frac{1}{2}}} = \frac{4}{3}\langle S_{\rm n(N)}\rangle^2 \frac{J+1}{J}
\end{aligned} \tag{3.65}$$

In Eq. (3.65), model dependent value $a_{\rm p}$ and $a_{\rm n}$ are cancelled and therefore this equation leads to a model independent calculation. $C^{\rm SD}_{\rm p(N)}/C^{\rm SD}_{\rm p}$ and $C^{\rm SD}_{\rm n(N)}/C^{\rm SD}_{\rm n}$ values calculated using the odd group model are listed in Table. 3.2.

Limits to $\sigma^{\rm SD}_{\chi-{\rm N}}$, are obtained by experiments and the $\sigma^{\rm SD}_{\chi-{\rm p}}$ and $\sigma^{\rm SD}_{\chi-{\rm n}}$ limits can be set by conservatively assuming that $\sigma^{\rm SD}_{\chi-{\rm N}}$ is dominated by either proton or neutron contribution only. Eq. (3.40) and Eq.(3.65) lead to:

$$\begin{aligned}
\sigma^{\rm SD}_{\chi-{\rm p}} &= \sigma^{\rm SD}_{\chi-{\rm N}} \frac{\mu^2_{\chi-{\rm p}}}{\mu^2_{\chi-{\rm N}}} \frac{C^{\rm SD}_{\rm p}}{C^{\rm SD}_{\rm p(N)}} \\
\sigma^{\rm SD}_{\chi-{\rm n}} &= \sigma^{\rm SD}_{\chi-{\rm N}} \frac{\mu^2_{\chi-{\rm n}}}{\mu^2_{\chi-{\rm N}}} \frac{C^{\rm SD}_{\rm n}}{C^{\rm SD}_{\rm n(N)}}.
\end{aligned} \tag{3.66}$$

Thus one can derive $\sigma^{\rm SD}_{\chi-{\rm p}}$ and $\sigma^{\rm SD}_{\chi-{\rm n}}$ from experimental results with the values in Table. 3.2 and Eq. (3.66).

- Limits in the $\sigma^{\rm SD}_{\chi-{\rm p}} - \sigma^{\rm SD}_{\chi-{\rm n}}$ plane

It is assumed that $\sigma^{\rm SD}_{\chi-{\rm N}}$ is dominated by either proton or neutron contribution only to derive the $\sigma^{\rm SD}_{\chi-{\rm p}}$ and $\sigma^{\rm SD}_{\chi-{\rm n}}$ limits. This is a conservative assumption and we can achieve a more realistic result if we are to set limits in the $\sigma^{\rm SD}_{\chi-{\rm p}} - \sigma^{\rm SD}_{\chi-{\rm n}}$ plane. From Eq. (3.37) and Eq. (3.64),

$$\frac{\sigma^{\rm SD}_{\chi-{\rm N}}}{\mu^2_{\chi-{\rm N}}} = \left(\sqrt{\frac{\sigma^{\rm SD}_{\chi-{\rm p}'} C^{\rm SD}_{\rm p(N)}}{\mu^2_{\chi-{\rm p}} C^{\rm SD}_{\rm p}}} \pm \sqrt{\frac{\sigma^{\rm SD}_{\chi-{\rm n}'} C^{\rm SD}_{\rm n(N)}}{\mu^2_{\chi-{\rm n}} C^{\rm SD}_{\rm n}}} \right)^2 \tag{3.67}$$

is derived, where $\sigma^{\rm SD}_{\chi-{\rm N}}$ is obtained from experimental results. Here we consider both contribution of proton and neutron cross sections to the $\sigma^{\rm SD}_{\chi-{\rm N}}$ and we write them as $\sigma^{\rm SD}_{\chi-{\rm p}'}$ and $\sigma^{\rm SD}_{\chi-{\rm n}'}$ to distinguish them from the neutralino-nucleon cross sections $\sigma^{\rm SD}_{\chi-{\rm p}}$ and $\sigma^{\rm SD}_{\chi-{\rm n}}$ derived assuming either of them dominates the $\sigma^{\rm SD}_{\chi-{\rm N}}$ and ignoring the others.

(a)unpaired proton					
Isotope	J	$\langle S_{\mathrm{p(N)}}\rangle$	$\langle S_{\mathrm{n(N)}}\rangle$	$C^{\mathrm{SD}}_{\mathrm{p(N)}}/C^{\mathrm{SD}}_{\mathrm{p}}$	$C^{\mathrm{SD}}_{\mathrm{n(N)}}/C^{\mathrm{SD}}_{\mathrm{n}}$
^{7}Li	3/2	0.497	0.004	5.49×10^{-1}	3.56×10^{-5}
^{19}F	1/2	0.441	–0.109	7.78×10^{-1}	4.75×10^{-2}
^{23}Na	3/2	0.248	0.020	1.37×10^{-1}	8.89×10^{-4}
^{27}Al	5/2	–0.343	0.030	2.20×10^{-1}	1.68×10^{-3}
^{35}Cl[43]	3/2	–0.059	–0.011	7.73×10^{-3}	2.69×10^{-2}
^{35}Cl[42]	3/2	–0.083	0.004	1.53×10^{-2}	3.56×10^{-5}
^{39}K	3/2	–0.184	0.054	7.20×10^{-2}	5.56×10^{-3}
^{127}I	5/2	0.309	0.075	1.78×10^{-1}	1.05×10^{-2}
(b)unpaired neutron					
Isotope	J	$\langle S_{\mathrm{p(N)}}\rangle$	$\langle S_{\mathrm{n(N)}}\rangle$	$C^{\mathrm{SD}}_{\mathrm{p(N)}}/C^{\mathrm{SD}}_{\mathrm{p}}$	$C^{\mathrm{SD}}_{\mathrm{n(N)}}/C^{\mathrm{SD}}_{\mathrm{n}}$
^{29}Si	1/2	–0.002	0.130	1.60×10^{-5}	6.76×10^{-2}
^{73}Ge	9/2	0.009	0.372	1.32×10^{-4}	2.26×10^{-1}
^{125}Te	1/2	0.001	0.287	4.00×10^{-6}	3.29×10^{-1}
^{129}Xe	1/2	0.028	0.359	3.14×10^{-3}	5.16×10^{-1}
^{131}Xe	3/2	–0.009	–0.227	1.80×10^{-4}	1.15×10^{-1}

Table 3.2: Values of $\langle S_{\mathrm{p(N)}}\rangle, \langle S_{\mathrm{n(N)}}\rangle, C^{\mathrm{SD}}_{\mathrm{p(N)}}/C^{\mathrm{SD}}_{\mathrm{p}}, C^{\mathrm{SD}}_{\mathrm{n(N)}}/C^{\mathrm{SD}}_{\mathrm{n}}$ for various nuclei. Values for Li and F are taken from Ref.[43] and those for Si and Ge are taken from Ref.[44]. Values for Na, I, Xe, and Te are taken from Ref.[45] and those for Al and K are taken from Ref.[46]. Values of $\langle S_{\mathrm{p}}\rangle, \langle S_{\mathrm{n}}\rangle$ for Cl is taken both from Ref. [43] and [42] as they have opposite sign of $\langle S_{\mathrm{p}}\rangle/\langle S_{\mathrm{n}}\rangle$ values. These values are calculated by the odd group model. However, due to the differences of the shell model taken by authors, these vales are not always consistent to the $\lambda^2 J(J+1)$ values listed in Table 3.1.

From Eq. (3.66) and Eq. (3.67), neutralino type independent limit in the $\sigma^{\rm SD}_{\chi-{\rm p}'} - \sigma^{\rm SD}_{\chi-{\rm n}'}$ plane is defined as

$$\left(\sqrt{\frac{\sigma^{\rm SD}_{\chi-{\rm p}'}}{\sigma^{\rm SD}_{{\rm lim}\chi-{\rm p}}}} \pm \sqrt{\frac{\sigma^{\rm SD}_{\chi-{\rm n}'}}{\sigma^{\rm SD}_{{\rm lim}\chi-{\rm n}}}}\right)^2 = 1 \tag{3.68}$$

where $\sigma^{\rm SD}_{{\rm lim}\chi-{\rm p}}$ and $\sigma^{\rm SD}_{{\rm lim}\chi-{\rm n}}$ are the limits derived from Eq. (3.66) and the small proton-neutron mass difference is ignored.

Eq. (3.68) shows that proton and neutron can have a constructive and destructive interference according to the relative sign ambiguity. The sign ambiguity in Eq. (3.68) is due to the sign ambiguity of $a_{\rm p}$ and $a_{\rm n}$ which is the outcoming of the SUSY model. As we have no information on the $a_{\rm p}\langle S_{\rm p}\rangle/a_{\rm n}\langle S_{\rm n}\rangle$ sign, taking the relative minus sign in Eq. (3.68) would give a conservative limit.

- Limits in the $a_{\rm p}$-$a_{\rm n}$(neutralino-nucleon couplings) plane.
  Though setting the limits in the $\sigma^{\rm SD}_{\chi-{\rm p}'} - \sigma^{\rm SD}_{\chi-{\rm n}'}$ plane is a good way of showing model independent result, the result is still conservative because of the sign ambiguity in Eq. (3.68). If we are to set limits in the $a_{\rm p}$-$a_{\rm n}$ plane, the sign ambiguity in Eq. (3.68) is contained in the result and we will have a model independent and not unnecessarily conservative results. Eq. (3.37) and Eq. (3.68) lead

$$\left(\frac{a_{\rm p}}{\sqrt{\sigma^{\rm SD}_{{\rm lim}\chi-{\rm p}}}} \pm \frac{a_{\rm n}}{\sqrt{\sigma^{\rm SD}_{{\rm lim}\chi-{\rm n}}}}\right)^2 = \frac{\pi\hbar^4}{24 G_{\rm F}^2 \mu_{\rm p}^2} \tag{3.69}$$

  $a_{\rm p}$ and $a_{\rm n}$ can have either sign and the relative sign in Eq. (3.69) is determined by the sign of $\langle S_{\rm p}\rangle/\langle S_{\rm n}\rangle$ which we know.

We have shown three ways to derive a model independent results for one element of target only. A generalization to two or more elements in the same target is straightforward. The limits $\sigma^{\rm SD}_{{\rm lim}\chi-{\rm p(Ni)}}$ and $\sigma^{\rm SD}_{{\rm lim}\chi-{\rm n(Ni)}}$ from different nuclei $N_{\rm i}$ in a target N is combined by

$$\frac{1}{\sigma^{\rm SD}_{{\rm lim}\chi-{\rm p}'}} = \sum_{N_{\rm i}} \frac{1}{\sigma^{\rm SD}_{{\rm lim}\chi-{\rm p(Ni)}}} \tag{3.70}$$

$$\frac{1}{\sigma^{\rm SD}_{{\rm lim}\chi-{\rm n}'}} = \sum_{N_{\rm i}} \frac{1}{\sigma^{\rm SD}_{{\rm lim}\chi-{\rm n(Ni)}}} \tag{3.71}$$

The combined limits in the $\sigma^{\rm SD}_{\rm p}$-$\sigma^{\rm SD}_{\rm n}$ plane are obtained by generalizing Eq. (3.68).

$$\sum_{N_{\rm i}} \left(\sqrt{\frac{\sigma^{\rm SD}_{\chi-{\rm p}'}}{\sigma^{\rm SD}_{{\rm lim}\chi-{\rm p(Ni)}}}} \pm \sqrt{\frac{\sigma^{\rm SD}_{\chi-{\rm n}'}}{\sigma^{\rm SD}_{{\rm lim}\chi-{\rm n(Ni)}}}}\right)^2 = 1 \tag{3.72}$$

And the same holds true for the $a_{\rm p}$-$a_{\rm n}$ plane.

$$\sum_{N_{\rm i}} \left(\frac{a_{\rm p}}{\sqrt{\sigma^{\rm SD}_{{\rm lim}\chi-{\rm p(Ni)}}}} \pm \frac{a_{\rm n}}{\sqrt{\sigma^{\rm SD}_{{\rm lim}\chi-{\rm n(Ni)}}}} \right)^2 = \frac{\pi\hbar^4}{24 G_{\rm F}^2 \mu_{\rm p}^2} \tag{3.73}$$

can be used to derive a model independent results from a target with two or more species. Examples of these three results are shown in Fig. 3.3 - Fig. 3.5. An example of the $\sigma^{\rm SD}_{\chi-{\rm p}}$ limits and $\sigma^{\rm SD}_{\chi-{\rm n}}$ limits derived from synthesized NaI data are shown in Fig.3.3[42]. $\sigma^{\rm SD}_{\chi-{\rm p}}$ limits and $\sigma^{\rm SD}_{\chi-{\rm n}}$ limits for 100GeVc^{-2} neutralinos in Fig. 3.3 for a 100GeVc^{-2} neutralino are shown in Table 3.3. We derived limits in the $\sigma^{\rm SD}_{\chi-{\rm p}'} - \sigma^{\rm SD}_{\chi-{\rm n}'}$ plane for 100GeVc^{-2} neutralinos with the values listed in Table 3.3. The limits in the $\sigma^{\rm SD}_{\chi-{\rm p}'} - \sigma^{\rm SD}_{\chi-{\rm n}'}$ plane for a 100GeVc^{-2} neutralino are shown in Fig. 3.4. As is shown in Fig. 3.4, allowed region for destructive interference expands to infinity with single nuclide. An example of the limits in the $a_{\rm p} - a_{\rm n}$ plane derived from the same data is shown in Fig. 3.5. It is seen that one nuclide is not enough to set a finite allowed region in the $a_{\rm p} - a_{\rm n}$ plane.

$\sigma_p^{\rm SD}$(Na)	0.05 pb
$\sigma_p^{\rm SD}$(I)	0.09 pb
$\sigma_n^{\rm SD}$(Na)	9 pb
$\sigma_n^{\rm SD}$(I)	1.5 pb

Table 3.3: Values used in the calculations for Fig. 3.4 and Fig. 3.5.

3.4 F^2, Nuclear Form Factor

When the momentum transfer $q = (2M_{\rm N}E_{\rm R})^{1/2}$ is such that the wavelength h/q is no longer large compared to the nuclear radius, the effective cross section begins to fall with increasing q. Here h is the Planck constant. We call this effect the form factor and in the first Born (plane wave) approximation, the form factor is the Fourier transform of $\rho(r)$, the density distribution of the 'scatterings centers':

$$F(E_{\rm R}) = \int \rho(r) \exp(i \cdot \vec{q} \cdot \vec{r}) d^3\vec{r} \tag{3.74}$$

The cross section $\sigma_{\chi-{\rm N}}$ discussed in the former section is corrected by this form factor as $\sigma(E_{\rm R}) = \sigma_{\chi-{\rm N}} F^2(E_{\rm R})$. A commonly used approximation for small momentum transfer is:

$$F^2(E_{\rm R}) = \exp(-(qr_{\rm n})^2/3). \tag{3.75}$$

where $r_{\rm n}$ is an effective nuclear radius and commonly used approximation is $r_{\rm n} \sim A^{1/3}$fm or, $r_{\rm n} \sim 0.89A^{1/3}$+0.30 fm[47]. More precise studies have been done for spin-dependent and spin-independent interactions.

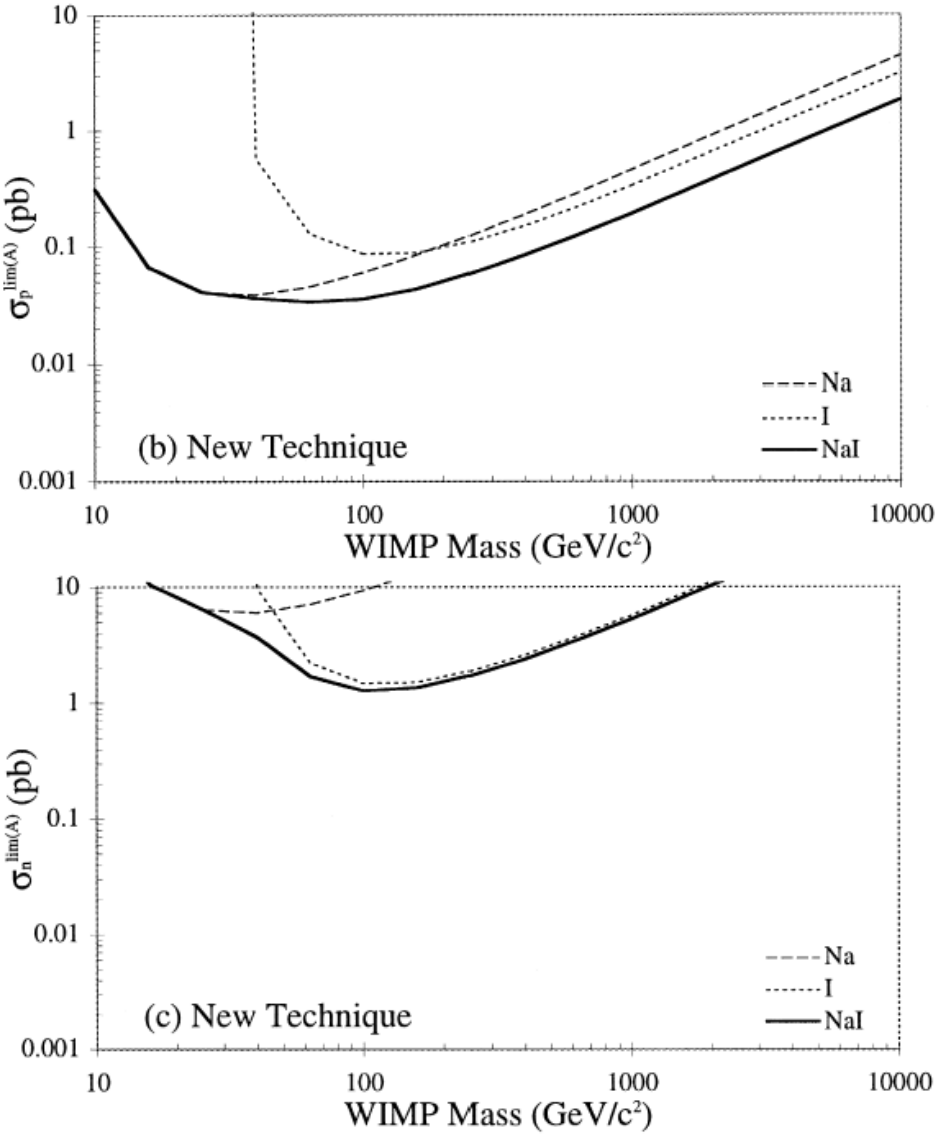

Figure 3.3: An example of $\sigma^{\rm SD}_{\chi-{\rm p}}$ limits and $\sigma^{\rm SD}_{\chi-{\rm n}}$ limits as a function of M_χ. These plots are calculated using synthesized NaI data. Figure (b) and (c) shows the limits $\sigma^{\rm SD}_{\chi-{\rm p}}$ limits and $\sigma^{\rm SD}_{\chi-{\rm n}}$ limits, respectively. In the plot, limit by Na(I) is shown in dashed(dotted) curve, and the combined limit is shown in thick solid curve. These figures are taken from Ref. [42].

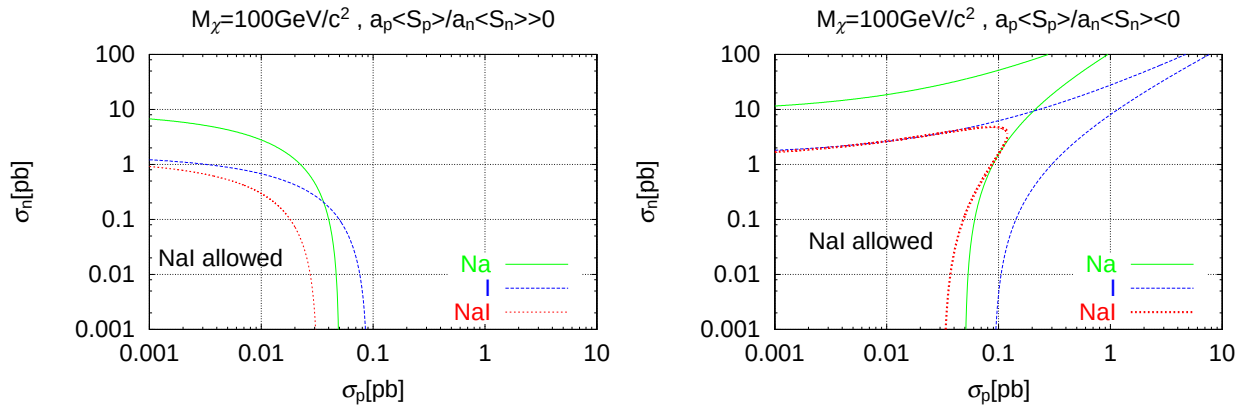

Figure 3.4: An example of limits in the $\sigma_{\rm p} - \sigma_{\rm n}$ plane for $\rm M_\chi = 100 GeVc^{-2}$. Constructive($a_{\rm p}\langle S_{\rm p}\rangle / a_{\rm n}\langle S_{\rm n}\rangle > 0$) and destructive($a_{\rm p}\langle S_{\rm p}\rangle / a_{\rm n}\langle S_{\rm n}\rangle < 0$) interference are shown in the left and the right, respectively. We used $\sigma_{\rm p}$ and $\sigma_{\rm n}$ values in Fig. 3.3 for the calculation. $\sigma_{\rm p}$ and $\sigma_{\rm n}$ values used for this calculation are listed in Table 3.3. It is seen that single nuclide is not sufficient to set a finite allowed region in the $\sigma_{\rm p} - \sigma_{\rm n}$ plane for the destructive case.

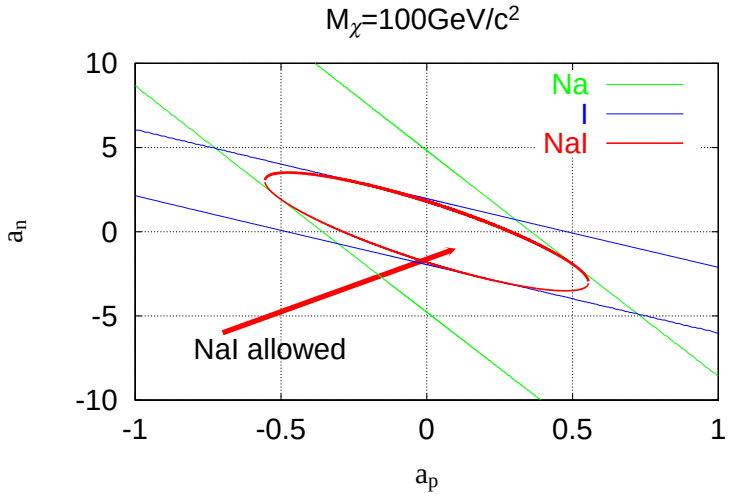

Figure 3.5: An example of limits in the $a_{\rm p} - a_{\rm n}$ plane for $\rm M_\chi = 100 GeVc^{-2}$. As $a_{\rm p}$ and $a_{\rm n}$ can have either sign, the result is shown in one figure. Values used for this calculation are same as those for Fig. 3.4. It is seen that single nuclide is not sufficient to set a finite allowed region in the $a_{\rm p} - a_{\rm n}$ plane.

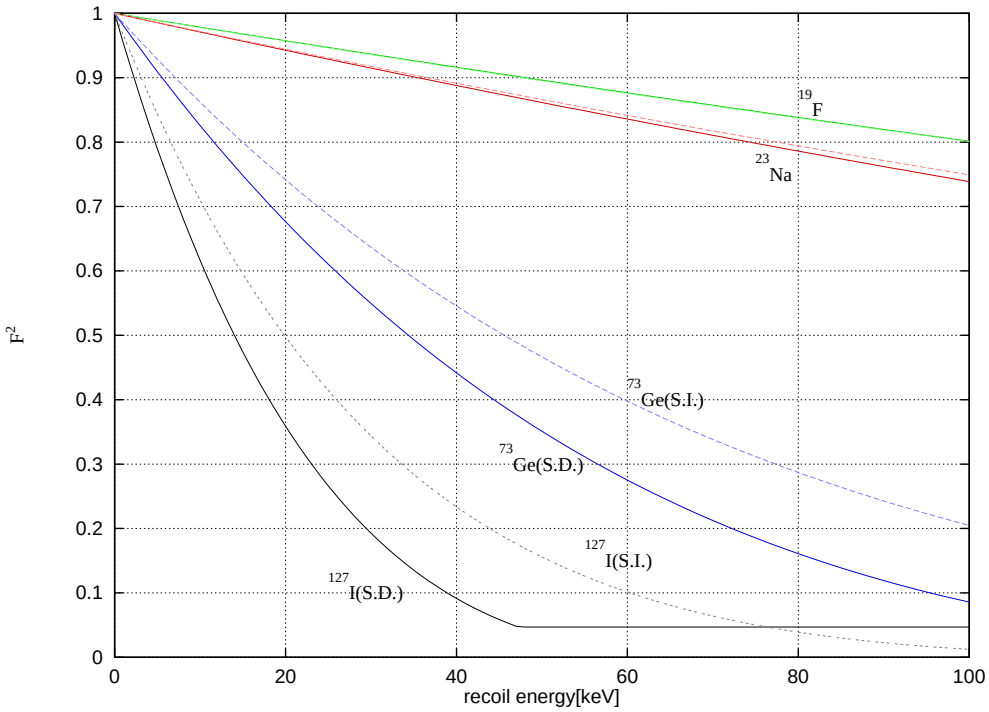

Figure 3.6: Values of the form factor as a function of recoil energy for the SI and SD interactions. Here, dashed and solid lines represent SI and SD interaction form factors, respectively.

For the spin-independent interactions, the form factor is written as:

$$F^2(E_{\rm R}) = \left[\frac{3j_1(qr_{\rm n})}{qr_{\rm n}}\right]^2 \exp[-(qs)^2]. \tag{3.76}$$

where s $\sim$ 1fm is the nuclear skin thickness.

For the spin-dependent interactions, if the single particle model is assumed, the Bessel function is obtained from Eq.(3.74):

$$F^2(E_{\rm R}) = j_0^2(qr_{\rm n}) \tag{3.77}$$

In the case of the odd group model, the form factor is approximated by the Bessel function partially filled with constant value:

$$F^2(E_{\rm R}) = \begin{cases} j_0^2(qr_{\rm n}) & (qr_{\rm n} < 2.55, qr_{\rm n} > 4.5) \\ 0.047(\text{constant}) & (2.55 \leq qr_{\rm n} \leq 4.5) \end{cases} \tag{3.78}$$

Values of the form factor as a function of recoil energy for SI and SD cases are shown in Figure 3.6.

Chapter 4

Bolometer for Dark Matter Search Experiment

The bolometer is a cryogenic particle detector developed in the last few decades and has notable features like high resolution, low threshold, and no quenching. We have developed a LiF bolometer with an NTD Ge thermistor attached to it and have performed some preceding measurements. Our history of the LiF bolometer development is summarized in Table 4.1.

Year	Status	Site	References
-1996	Fabrication of NTD Ge thermistors	Tokyo(surface)	Section 4.2,[60]
-1997	Development of LiF Bolometers	Tokyo(surface)	Section 4.3,[61]
-1999	Pilot Run	Nokogiriyama($\sim$15m.w.e.)	Section 4.4,[29]
2000	Modification	Tokyo(surface)	
2000-	Underground Measurement	Kamioka($\sim$2700m.w.e.)	Section 4.5,[63]

Table 4.1: The history of our dark matter search experiment.

4.1 Bolometer

The bolometer is a particle detector which senses small increase of the temperature of target material caused by an interaction with particles such as photons, electrons, alpha particles, neutrons, and neutralinos. The bolometer often consists of an absorber and a sensitive thermometer attached to it. In some cases, the thermometer is used as the absorber itself. In order to achieve high sensitivity, the bolometer is cooled down to less than 1K so that the heat capacity of the target material becomes small. The heat capacity of an insulator is dominated by that of a lattice because the heat capacity contribution of electrons is negligible at low temperature. The heat capacity of the lattice is calculated as follows.

The energy of the lattice is expressed as

$$\begin{aligned} U &= 3\int_0^{\omega_{\rm D}} d\omega g(\omega) n(\omega) \hbar\omega \\ &= 3\int_0^{\omega_{\rm D}} d\omega \left(\frac{V\omega^3}{2\pi^2 v^3}\right)\left(\frac{\hbar\omega}{e^{\hbar\omega/k_{\rm B}T}-1}\right) \\ &= \frac{3V\hbar}{2\pi^2 v^3}\int_0^{\omega_{\rm D}} d\omega \frac{\omega^3}{e^{\hbar\omega/k_{\rm B}T}-1}. \end{aligned} \tag{4.1}$$

where $g(\omega) = dN/d\omega$ is the density of the mode and $n(\omega)$ is the Planck distribution function and $\omega_{\rm D} = 6\pi^2 v^3 N/V$ is the cutoff frequency. The heat capacity $C(T) = \frac{\delta U}{\delta T}$ is approximated to be

$$\begin{aligned} C({\rm T}) &= \frac{12\pi^4}{5} N k_{\rm B}\left(\frac{T}{\Theta_{\rm D}}\right)^3 \\ &\sim 1\times 10^{18}\left(\frac{T}{\Theta_{\rm D}}\right)^3 {\rm keVcm^{-3}\cdot K^{-1}} \end{aligned} \tag{4.2}$$

where $\Theta_{\rm D} = \hbar\omega_{\rm D}/k_{\rm B}$ is the Debey temperature which corresponds to the cutoff frequency $\omega_{\rm D}$. Debey temperature of some insulators are shown in Table 4.2. As we chose LiF as the target material for several reasons described in Section 3, we shall calculate the heat capacity of LiF here. The heat capacity of a 20g LiF crystal is

$$\sim 2\times 10^4\left(\frac{T}{10{\rm mK}}\right)^3 {\rm keVK^{-1}} \tag{4.3}$$

We can calculate the temperature increase of the LiF crystal to be about 50μK for energy deposition of 10keV.

The bolometer has some features as follows. Here we refer to ionization and scintillation detectors as conventional detectors and we focus on the difference between bolometers and conventional detectors.

- Wide Choice of Materials
  We do not have a wide choice of the materials of the conventional detectors. On the other hand, most of insulators and superconductors have very small heat capacity at low temperature and can be used as an absorber of a bolometer. As we discussed in Section 3, certain materials are said to have large cross section of the elastic scattering with neutralinos and we can make a suitable detector for neutralino detection by choosing them as the target material. We have chosen LiF aiming for the neutralino detection by spin-dependent interaction.

- High Energy Resolution
  Scintillation detectors have poor resolution around the threshold because of the number

Crystal	$\Theta_{\rm D}$(K)
C(diamond)	2230
LiF	732
Fe_2O_3	660
Si	640
CaF_2	510
NaF	492
Ge	370
NaCl	321
Ta	240
InSb	200
NaI	164

Table 4.2: Debye temperature of some insulators[50].

of the photoelectron is very small. In the case of the bolometer, the average energy of thermal phonon is 2μ eV at 20 mK. Therefore, for a given deposited energy the bolometer senses much higher number of quanta than conventional detectors and can in principle has much better energy resolution. In fact, an energy resolution of 133 eV FWHM on the 1.5 keV X-ray of aluminum is reported[51].

- No Quenching
  Response of the conventional detectors to a nuclear recoil is different from that to an electron recoil. The detectors are generally calibrated with gamma ray sources, therefore, the quenching factors:
  $$f_{\rm Q} = E_{\rm n}/E_{\rm e} \tag{4.4}$$
  where $E_{\rm n}$ is the observed energy for a nuclear recoil and $E_{\rm e}$ is the observed energy for an electron recoil of the same energy as the nuclear recoil, have been measured for the proper energy calibration. The quenching factors of conventional detectors are generally less than unity as listed in Table 4.3. On the other hand, the bolometers in principle do not have the quenching. Actually the quenching factor of a bolometer has been measured and reported to be close to unity[52].

- Slow Signal
  Since we observe the temperature increase of the target crystal, the time constant is governed by the thermalisation of the crystal and the thermal coupling with the refrigerator. Typical rise time constant is 5 to 20msec and that of the decay time is 100 to 200msec, which are relatively slow compared with those of conventional detectors. In the early stage of the experiment, the count rate is still high because of the background and this slow signal is sometimes troublesome. However, the expected count rate of the

Detector	Nucleus	f_Q
NaI(Tl)[53]	Na	0.30
	I	0.09
CaF_2(Eu)[54]	Ca	0.08
	F	0.12
CaF_2(Eu)[55]	Ca	0.09
	F	0.11
Ge[56]	Ge	0.25
Si[57]	Si	0.30
Xe[58]	Xe	0.55±0.11

Table 4.3: Measured quenching factors for semiconductor and scintillation detectors.

dark matter is very low and this slow signal is not a problem for a dark matter search experiment in a deep underground site.

- Mass Limit
  For the rare event search, a large detector mass is required. A large mass bolometer, however, leads to small signal to noise ratio because the heat capacity of the absorber is proportional to the mass. However, if we use an array with small mass of bolometers, enough mass can be obtained.

For the features described above, we have chosen the bolometer for the detector of our dark matter search experiment.

4.2 Neutron Transmutation Doped Germanium (NTD Ge) Thermistors

The recoil energy caused by the neutralino-nucleus elastic scattering is in the order of 10keV. As the temperature increase of a LiF crystal with mass of 20g at 20mK is about 50μK for a energy deposit of 10 keV , we need a very sensitive phonon sensor that works at the low temperature of below 1K.

4.2.1 Heavily Doped Semiconductor

In a heavily doped and compensated semiconductor, electrical conductance is dominated by charges 'hopping' from an occupied dopant site to an unoccupied site[59]. The resistance $R(T)$ is written as

$$R(T) \propto \exp\left(\frac{r}{\lambda}\right) \exp\left(\frac{\delta_\epsilon}{k_\mathrm{B}T}\right) \tag{4.5}$$

where r is the distance between the dopants, λ is the characteristic size of the wave function of a charge carrier, δ_ϵ is the energy level of the dopant from the ground state. This is the resistance between the two states. For the conduction of a bulk sample, paths among many states are considered and $R(T)$ is found to have the minimum at

$$\delta_\epsilon = \sqrt{\frac{k_\mathrm{B}T}{a}}. \tag{4.6}$$

Therefore, the temperature dependence of the resistance $R(T)$ is written as

$$R(T) = R_0 \exp\left(\frac{\Delta}{T}\right)^{\frac{1}{2}} \tag{4.7}$$

where R_0 and Δ are constant parameters.

4.2.2 Fabrication

With heavily doped germanium semiconductors, we have fabricated very sensitive thermistors[60]. These thermistors are manufactured by the neutron transmutation doping (NTD) method. The NTD method is a technique to dope semiconductors by the partial transmutation of its stable isotopes to dopant impurities via thermal neutron capture. The relevant reactions are listed in Table 4.4.

Isotope	Abundance [%]	Cross Section [barn]	Reaction	Dopant Type
$^{70}_{32}$Ge	20.5	3.25	$^{70}_{32}\mathrm{Ge(n,\gamma)}^{71}_{32}\mathrm{Ge} \overset{11.2\mathrm{d}}{\rightarrow} {}^{71}_{31}\mathrm{Ga}$	p
$^{72}_{32}$Ge	27.4	1.0	$^{72}_{32}\mathrm{Ge(n,\gamma)}^{73}_{32}\mathrm{Ge}$	-
$^{73}_{32}$Ge	7.8	15	$^{73}_{32}\mathrm{Ge(n,\gamma)}^{74}_{32}\mathrm{Ge}$	-
$^{74}_{32}$Ge	36.5	0.52	$^{74}_{32}\mathrm{Ge(n,\gamma)}^{75}_{32}\mathrm{Ge} \overset{82.8\mathrm{m}}{\rightarrow} {}^{75}_{33}\mathrm{As}$	n
$^{76}_{32}$Ge	7.8	0.16	$^{76}_{32}\mathrm{Ge(n,\gamma)}^{77}_{32}\mathrm{Ge} \overset{11.3\mathrm{h}}{\rightarrow} {}^{77}_{33}\mathrm{As} \overset{38.8\mathrm{h}}{\rightarrow} {}^{77}_{34}\mathrm{Se}$	n

Table 4.4: Reactions of germanium isotopes in NTD method.

As the cross section is small enough for the size our the germanium crystals, NTDGe method provides uniform dopants concentration in the germanium.

Schematic drawing of the fabricated NTD thermistor is shown in Fig. 4.1. We have fabricated thermistors with various $R-T$ curves by changing the exposure of the germanium to the thermal neutrons. Three typical $R-T$ curves are shown in Fig. 4.2. $R-T$ curves of

several NTDGe3 thermistors, which have been used for most of the preceding measurements are shown in Fig. 4.3. The good reproductivity of the thermistor is seen in Fig. 4.3 and this feature gives a significant advantage in constructing a multiple array of the bolometers. Typical characteristic of the NTDGe3 thermistors shown in Fig. 4.3 is expressed by Eq. (4.7) with constant $\Delta = 10.6$K and $R_0 = 1.74 \times 10^{-2}\Omega$.

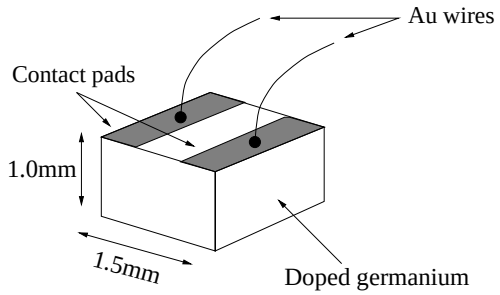

Figure 4.1: Schematic drawing of the fabricated NTD thermistor. The Au wires are 50 μm diameter.[60]

4.3 Development of the LiF Bolometer at a Surface Laboratory

We had developed a bolometer consisting of a 21g LiF crystal and an NTD Ge thermistor by the year 1997. Then we made a test run at the surface laboratory in the Hongo campus of the University of Tokyo. We adopted a shield of 10cm-thick lead. Details are described in Ref. [61]. We have obtained the spectrum shown in Fig. 4.4. The $\sigma^{\rm SD}_{\chi-{\rm p}}$ limits as a function of M_χ obtained in the surface run are shown in Fig. 4.8.

We have then developed a bolometer array consisting of 8 pieces of LiF bolometers with mass of 21g each before the next step.

4.4 Pilot Runs at a Shallow Depth Site

After the development at the surface laboratory, we moved the detector system to Nokogiriyama underground cell in 1998. Nokogiriyama underground cell is located 60km to the south of Tokyo and has at least 10 m.w.e. of overburden[62]. We used a bolometer array consisting of 8 LiF bolometers with mass of 21g each for the measurement at Nokogiriyama

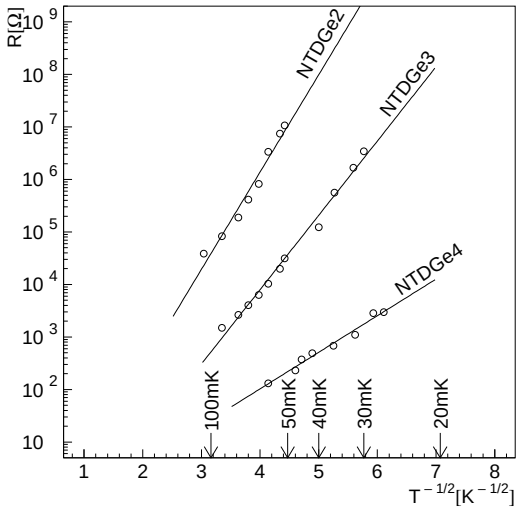

Figure 4.2: Three R-T curves of the NTDGe thermistors. R-T curves differ according to the total exposure to thermal neutrons.[60]

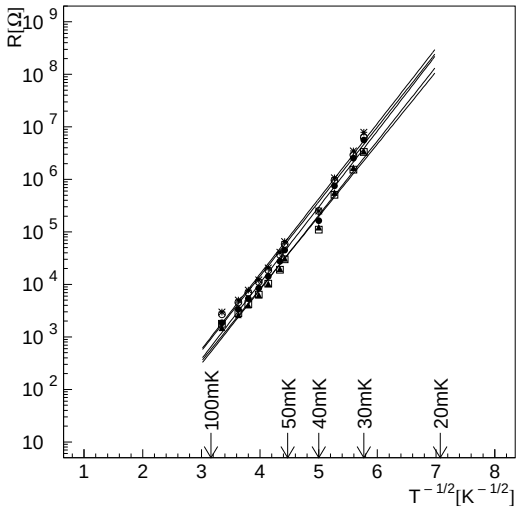

Figure 4.3: Five R-T curves of the NTDGe3 thermistors that are used for the dark matter search experiments at the surface and underground.[60]

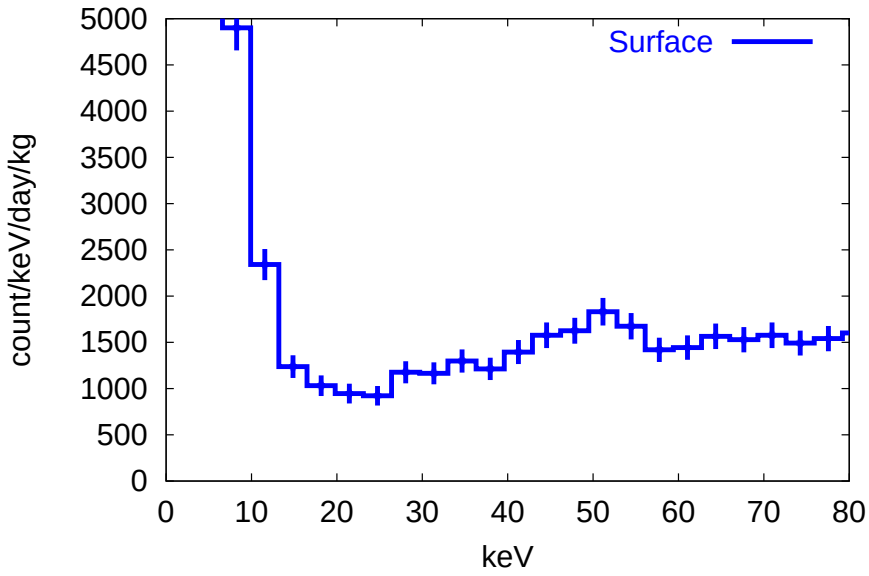

Figure 4.4: Energy spectrum obtained with a LiF bolometer at the surface laboratory. An exposure is 0.025 kg·days[61]

.

underground cell. Details are described in Ref.[19]. In the pilot run we have adopted a more stringent shields than those of the test run in the surface laboratory. The shields consist of 10cm-thick OFHC copper layer, 15cm-thick lead layer, 1g/cm^2-thick boric acid layer, and 20cm-thick polyethylene layer. Materials for the shields are previously radio-assayed with HPGe γ-ray spectrometer[62]. The energy spectrum obtained with one of the LiF bolometers(D3) is shown in Fig. 4.5. The $\sigma^{\rm SD}_{\chi-{\rm p}}$ limits as a function of M_χ obtained in the pilot run are shown in Fig. 4.8. In this pilot run, we have obtained a world-best $\sigma^{\rm SD}_{\chi-{\rm p}}$ limits for the neutralinos lighter than 5GeVc^{-2}[29].

4.5 Preliminary Underground Measurement(Kamioka-run4)

In November, 1999, we moved the detector system to Kamioka Observatory and started preliminary measurement in 2000. Kamioka Observatory is at Kamioka-cho, Gifu, Japan and has 2,700 m.w.e. of overburden. Details of the preliminary underground measurement are described in Ref. [63]. As we still suffered from the microphonic noise, the measurement was performed without the helium liquefier and re-filling the liquid helium every day. The spectrum obtained with one of the detectors(D8) is shown in Fig. 4.6. Comparison with the previous runs are shown in Fig. 4.7. Counting rate averaged between 20keV and 80keV has decreased by a factor of 7 compared to the pilot run at Nokogiriyama underground cell. The $\sigma^{\rm SD}_{\chi-{\rm p}}$ limits as a function of M_χ obtained in the preliminary underground run are shown in Fig. 4.8. Although we have improved the sensitivity to the neutralinos heavier than 20 GeVc^{-2} compared to the pilot run, the sensitivity to the lighter neutralinos has got worth than the pilot run. We found that microphonic noise and radioactive contamination in the LiF crystals are setting limit to the sensitivity. We have done some improvements as described in Section 5.2 and started the underground measurement in November, 2001.

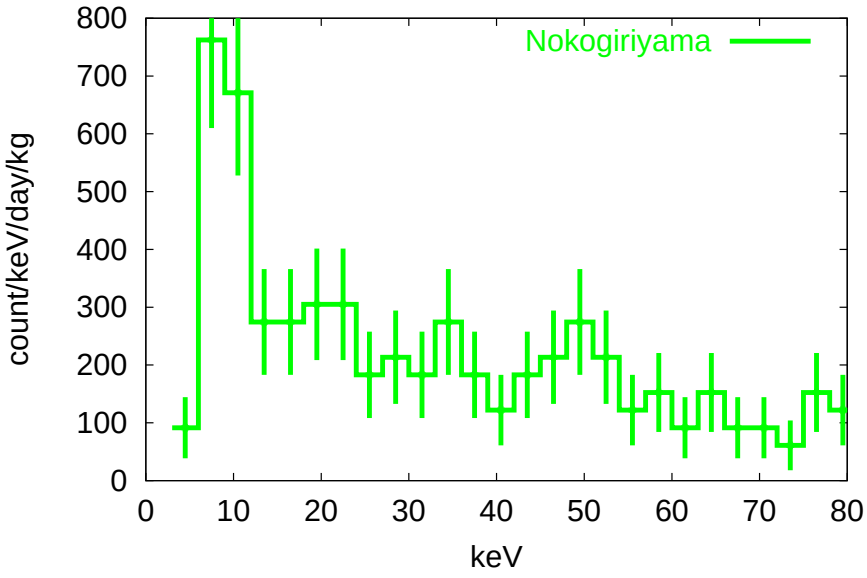

Figure 4.5: Energy spectrum obtained with one of the LiF bolometers(D3) in the pilot run at Nokogiriyama underground cell. The exposure is 0.011 kg · days[19].

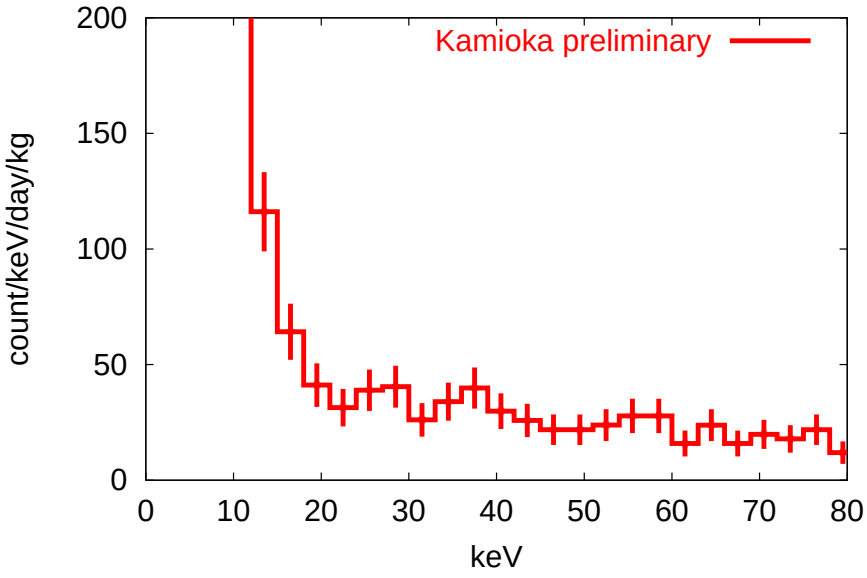

Figure 4.6: Energy spectrum obtained one of the detectors(D8) in the preliminary underground measurement at Kamioka Observatory. The exposure is 0.151 kg · days[63].

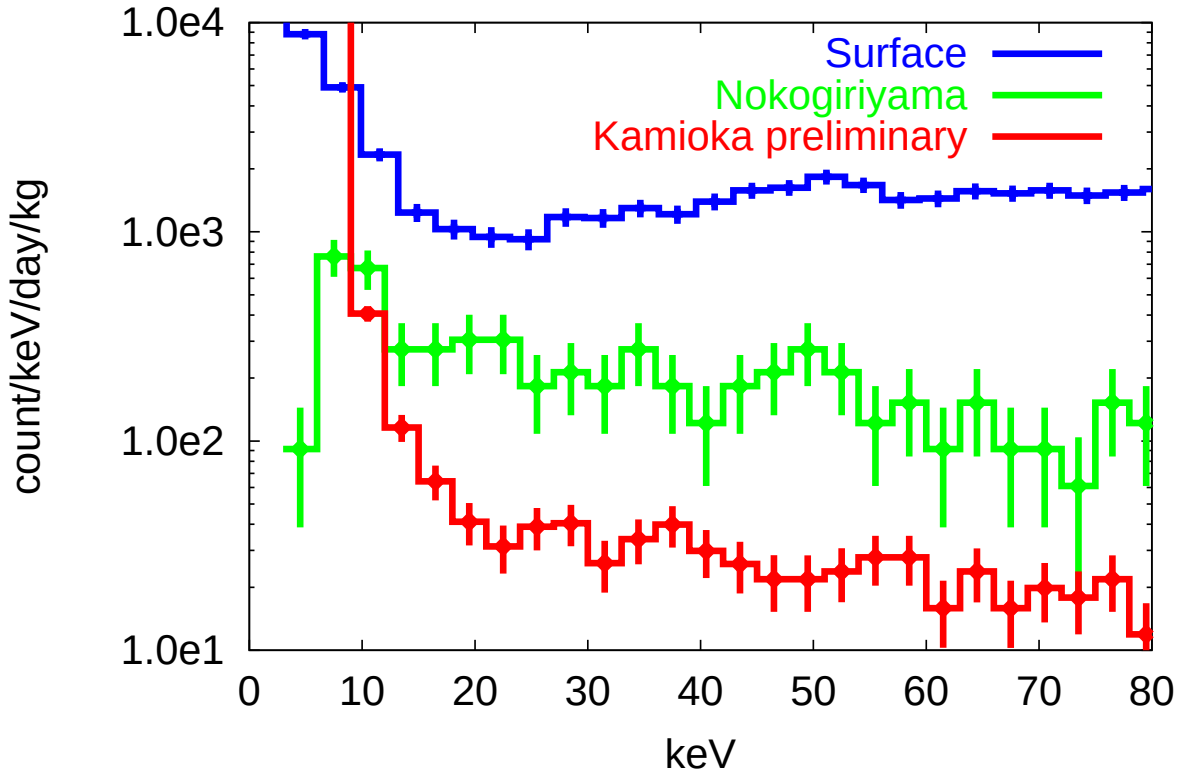

Figure 4.7: Energy spectra obtained in the test run at the surface[61], pilot run at Nokogiriyama underground cell[29], and the preliminary underground measurement at Kamioka Observatory[63]. The spectrum obtained in the test run at the surface is shown in blue(Surface). The spectrum obtained with one of the detectors(D3) in the pilot run at Nokogiriyama underground cell is shown in green(Nokogiriyama). The spectrum obtained with one of the detectors(D8) in the preliminary underground run at Kamioka Observatory is shown in red(Kamioka preliminary).

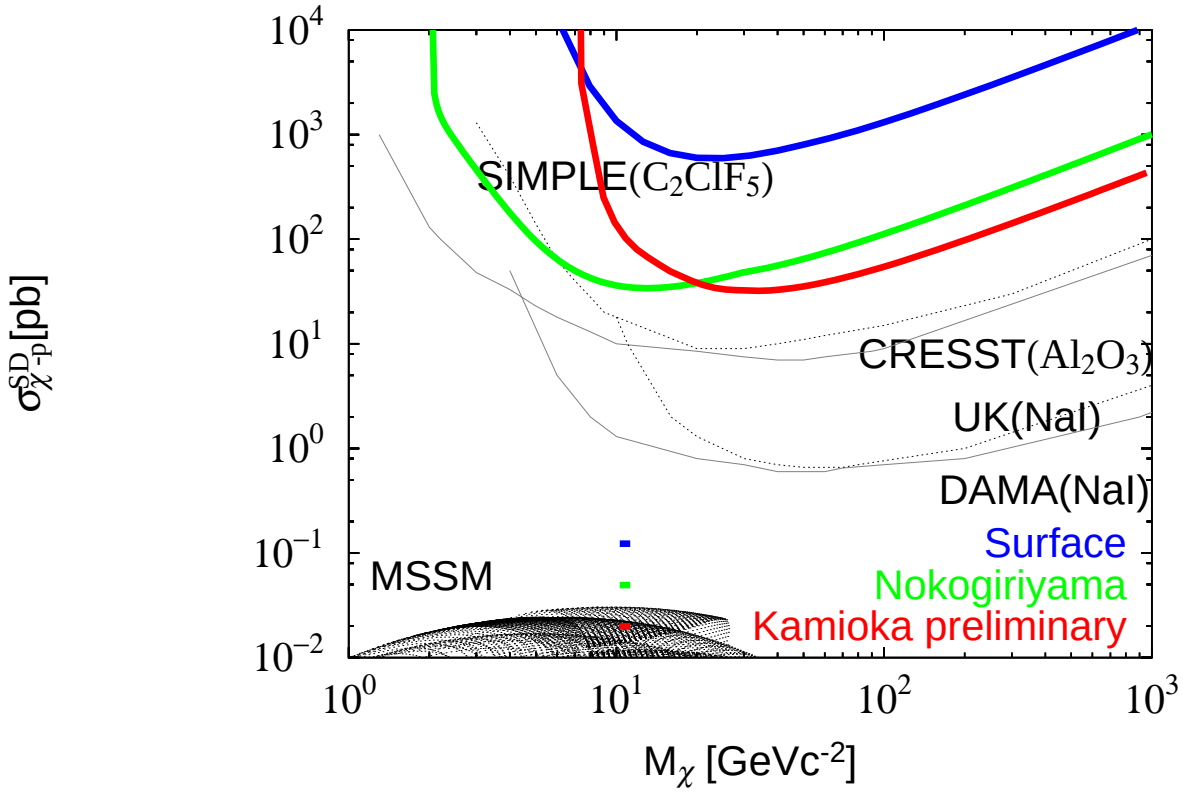

Figure 4.8: $\sigma^{\mathrm{SD}}_{\chi-\mathrm{p}}$ limits as a function of M_χ. The region above the curve is excluded at 90 % C.L. The result of the surface run is shown in blue(Surface), the result of the pilot run is shown in green(Nokogiriyama), and the result of the preliminary underground run is shown in red(Kamioka preliminary). For comparison the limits shown in [28, 30, 53, 64] are also plotted.

Chapter 5

Dark Matter Search Experiment in a Deep Underground Laboratory

We performed several test runs after the preliminary underground measurement at Kamioka Observatory and made several improvements as described in Section 5.2. Then we started our underground measurement(Kamioka-run9) in October 2001.

5.1 Detectors

5.1.1 Underground Laboratory at Kamioka Mine

The laboratory for this dark matter search experiment is newly caved about 50m away from Super-Kamiokande, which is placed at Mozumi Mine of the Kamioka Mining and Smelting Co. located at Kamioka-cho, Gifu, Japan. The laboratory is at the depth of 2,700 m.w.e. and the muon flux is reduced about five orders of magnitude compared to the surface laboratory. The neutron flux is also smaller than the surface laboratory by more than two orders of magnitude. The radon concentration in the air, however, is rather high and have a seasonal change according to the direction of the wind in the tunnel. Typical environmental background sources at Kamioka Observatory are shown in Table 5.1.

	surface	Nokogiriyama	Kamioka
muon[$cm^{-2}s^{-1}$]	1.1×10^{-2}	3.4×10^{-3}	$\sim 10^{-7}$
neutron[$cm^{-2}s^{-1}$]	8×10^{-3}	6×10^{-4}	2×10^{-5}
Rn(summer)[Bq/m^3]	40		1200
Rn(winter)[Bq/m^3]	40		40

Table 5.1: Typical background sources at Kamioka Observatory[62, 65, 66]

5.1.2 Cryogenics

We achieve the low tempreture of below 10mK for the measurement with LiF bolometers with several apparatus described bellow.

- Dilution refrigerator
  The dilution refrigerator is a refrigerator the cooling of which is achieved by the dilution of ^{3}He from the ^{3}He concentrated phase into the ^{3}He dilute phase. Continuous cooling is achieved by the circulation of the ^{3}He and this is important for a long term stable measurement like dark matter search experiment.

  We made a dilution refrigerator dedicated for this dark matter search experiment by ourselves, because commercially available dilution refrigerators are not free from radio active materials such as aluminum, stainless steel, and fiber reinforced plastics. Instead of these materials, OFHC(Oxygen Free High Conductivity) copper is used as much part as possible. The picture of this dilution refrigerator is shown in Fig. 5.1. The cooling power of our dilution refrigerator is calculated to be 2μW at 20mK and we can achieve the temperature of below 10mK with this refrigerator. The temperature is monitored by a CMN($2Ce(NO_3)_3 \cdot 3Mg(NO_3)_2 \cdot 24H_2O$) magnetic thermometer with superconducting quantum interferometric device(SQUID) read out.

- Helium liquefier
  For the long term uninterrupted measurement, we have installed a helium liquefier which liquefies helium evaporated from the dilution refrigerator system. This helium liquefier can make about $20l$ liquid helium a day.

- Liquid nitrogen generator
  We have some cold traps of liquid nitrogen temperature in the helium circulation of the dilution refrigerator and the helium liquefier in order to trap the air sneaking into the system. A liquid nitrogen generator that generates liquid nitrogen out of the air and transfers the nitrogen to the traps automatically is installed to the cryogenic system. This liquid nitrogen generator can generate about $30l$ of liquid nitrogen a day.

5.1.3 Shields

As the expected count rate caused by neutralino is extremely low, shields are inevitable for a dark matter search experiment. We have adopted a set of shield as listed in Table 5.2.

The polyethylene and the boric acid sheets act as the neutron moderator and absorber, the OFHC copper and the lead act as the shields against γ and β rays, and the air tight bag with nitrogen gas purges the radon gas inside the heavy shields. The inner shield is made of the old lead and is set in the 10mK stage. Since the inner lead plays an important role for this experiment, details are described in Section 5.2.1. The schematic view of the shields is shown in Fig.5.2.

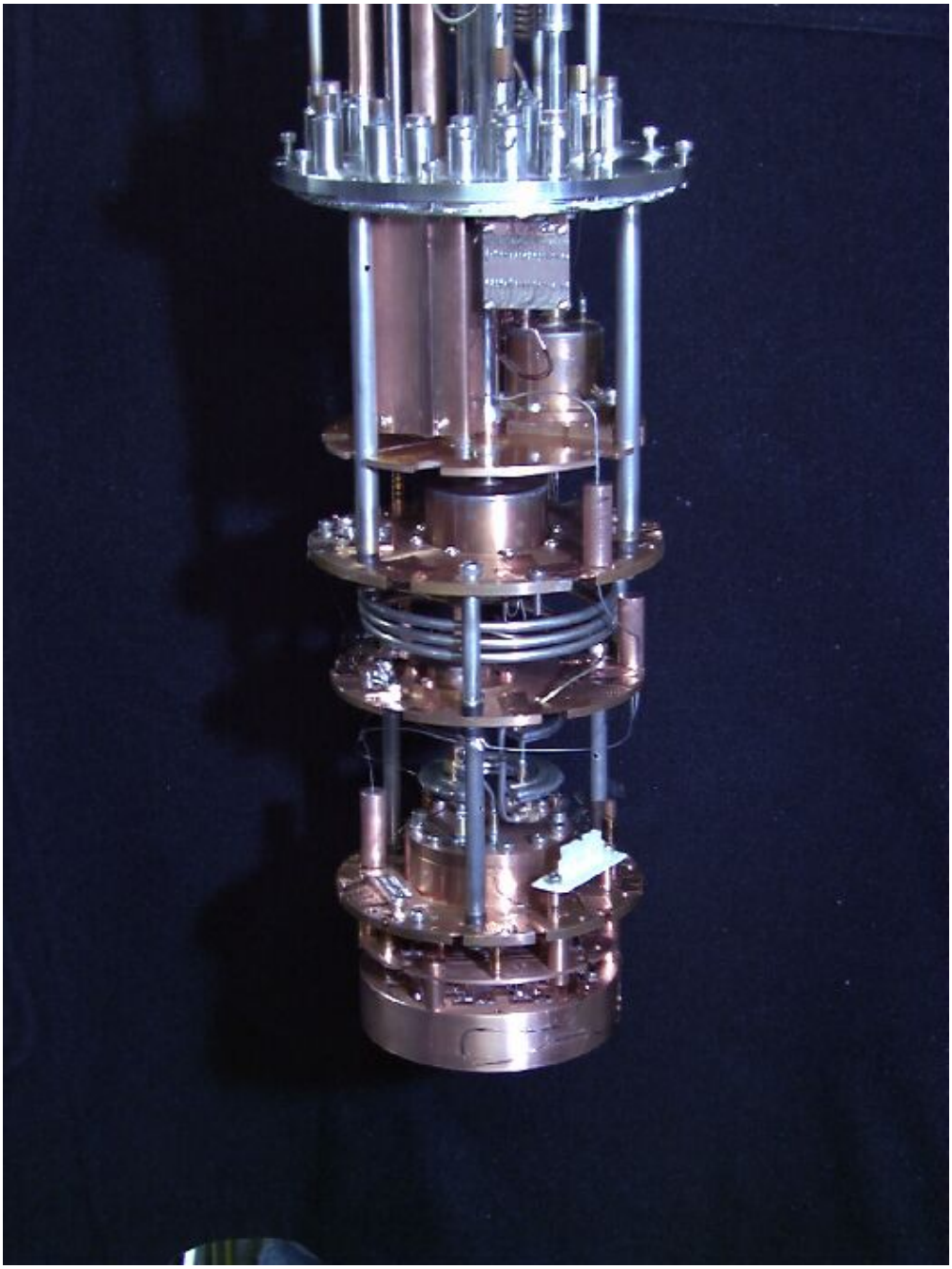

Figure 5.1: Picture of the dilution refrigerator made for this experiment.

material	thickness	purpose
polyethylene	20cm	fast moderator
boric acid sheet	1g/cm^2	thermal neutron capture
lead	15cm	γ and β rays
OFHC copper	10cm	γ and β rays
Air tight bag+nitrogen gas		Rn purge
inner shield	2cm	γ and β rays

Table 5.2: Material of the shield, thickness and its purpose. Listed from the outside.

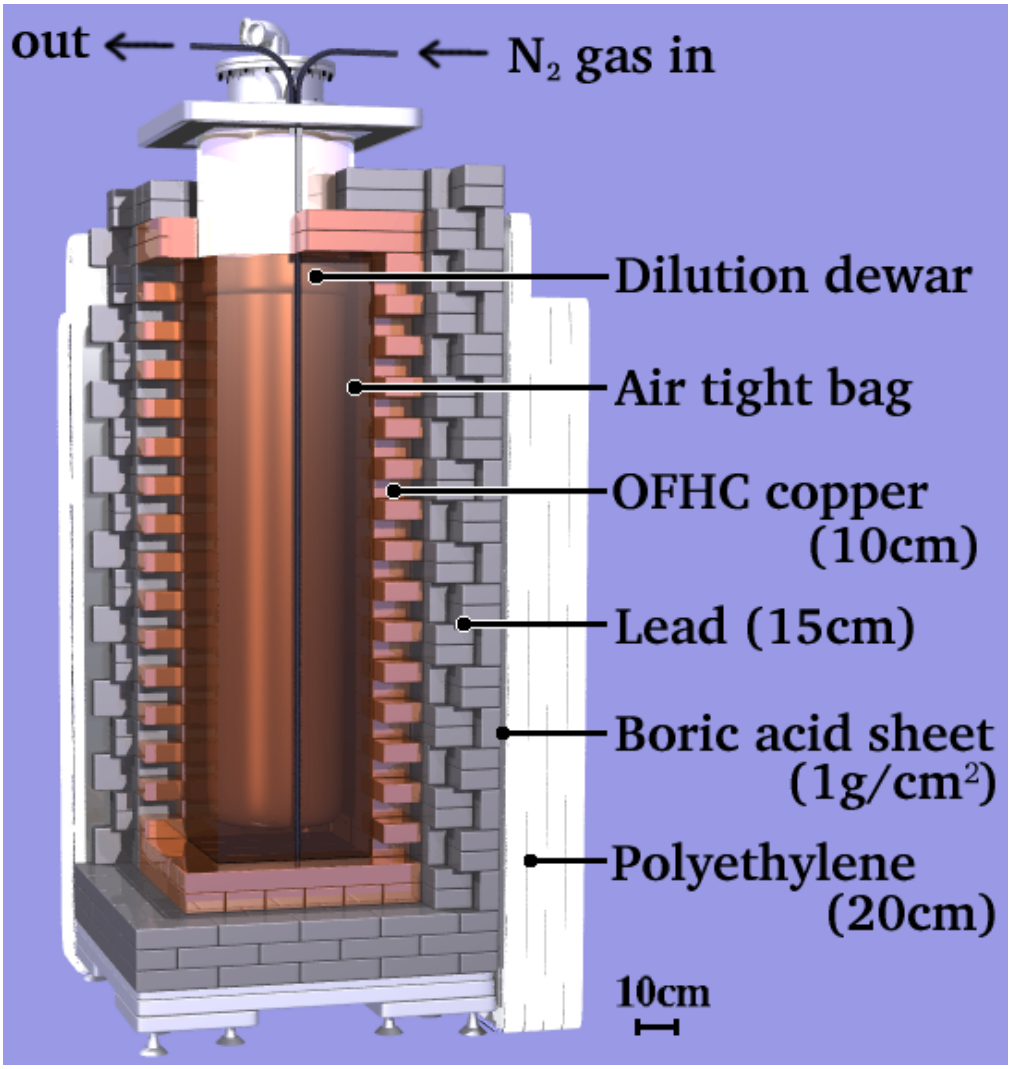

Figure 5.2: Schematic view of the shields[67].

5.1.4 Data Acquisition System

The block diagram of the data acquisition system for this experiment is shown in Fig. 5.3. Signals from the eight bolometers are amplified in the cold-stage pre-amplifier(Fig.5.4) and fed to the amplifier in the room tempreture(Fig. 5.11). The amplified signal is then put through the low pass filter(Fig. 5.12) and multiplexed by a 32-channel VXI multiplexer(DBS8720) together with the signals from the Rn detector and the status data of the cryogenics. The multiplexed data is then digitized by a 400kHz VXI digitizer with 16-bit resolution(DBS8701) and stored in the computer. The data size is 74M bytes per hour.

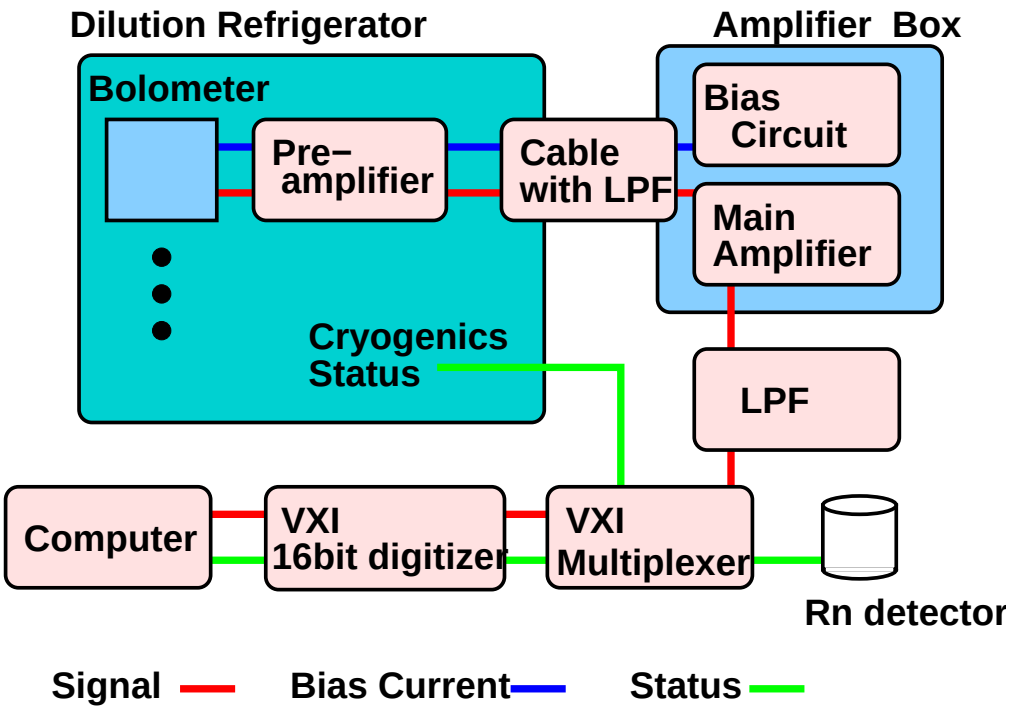

Figure 5.3: Block diagram of the data acquisition and status monitoring system.

All of the data are continuously taken without any triggers so that complete offline analysis is performed. The sampling rate is 1kHz per a bolometer channel and 100Hz per the Rn detector and the status channel. Monitored status data of the cryogenics are listed in Table 5.3. As the measurement is performed in the mine, the cryogenic status can be monitored from the outside by a computer and also by a cellular phone. The status of the cryogenics is monitored by a program which will send e-mails when the cryogenics have some troubles.

status	alert
^{3}He pressure before the cold trap in the dilution refrigerator system	*
^{3}He pressure after the cold trap in the dilution refrigerator system	*
liquid Helium bath pressure	*
remaining liquid Helium	*
pressures of the Helium liquefier	
cold stage temperature	
room temperature	

Table 5.3: Monitored cryogenic status.

5.1.5 Electronics

We have developed a electronic circuit dedicated for this experiment. This system is designed to achieve low noise by taking the merit of the slow time constant of the bolometer.

- Cold Stage Amplifier(pre-amplifier)
  NTDGe thermistor is DC-biased through a 100MΩ load resistance and the temperature rise of the bolometer causes the voltage change across the thermistor. The voltage change is fed to a voltage sensitive amplifier shown in Fig. 5.4. This amplifier is placed at the 4K cold stage in order to keep the high resistance bolometer signal lines($\sim$ 10MΩ) as short as possible. A junction field effect transistor(J-FET), NEC 2SK163 is used and the gain of this amplifier is ten. Since J-FET 2SK163 does not work at 4K, the FET is thermally decoupled from the cold stage. Schematic drawings of the mounting of the J-FET are shown in Fig. 5.5. The gate of the J-FET is connected by a stainless steel tube(0.31mm outer diameter, 0.09mm thickness, and 2cm length) that also make mechanical support, and source and drain of the J-FET are connected by manganin wires of 60μm diameter. A picture of the eight channel cold stage amplifier is shown in Fig. 5.6.

- Cable with Low Pass Filter
  As the bolometer signals are amplified by 4.8×10^3 with two stages of the amplifier, we need to take special care to the bias circuit. Therefore, the bias cable that connects the dilution refrigerator and the amplifier box needs to be a low noise cable and resistant to the microphonics and other noises. We adopted a low noise coaxial cable whose inner insulator is coated with semiconductor(shown in Fig. 5.7)[68]. Properties of the low noise coaxial cable are listed in Table 5.4. This cable generates little noises in vibration. The bias line, furthermore, has a low pass filter($f_c = 1.6$Hz) that is tightly attached to the dilution refrigerator. The schematic of this cable is shown in Fig. 5.8.

- Bias Current Supply

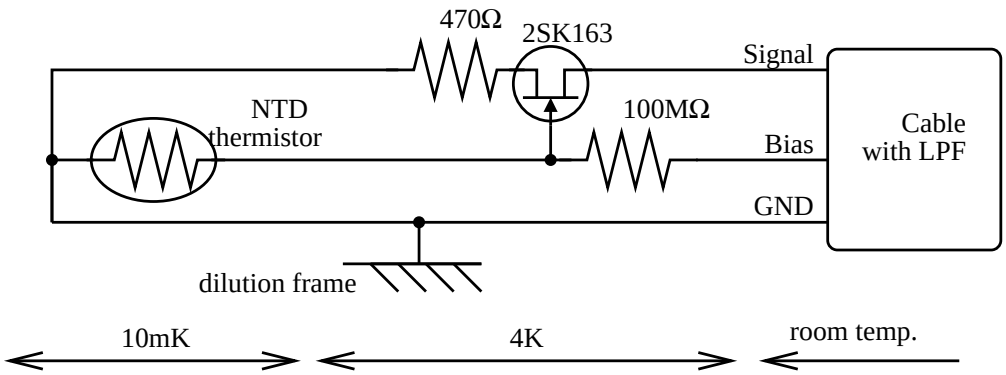

Figure 5.4: Schematic of the electrical circuit of the cold stage amplifier.(referred to as pre-amplifier in Fig. 5.3)

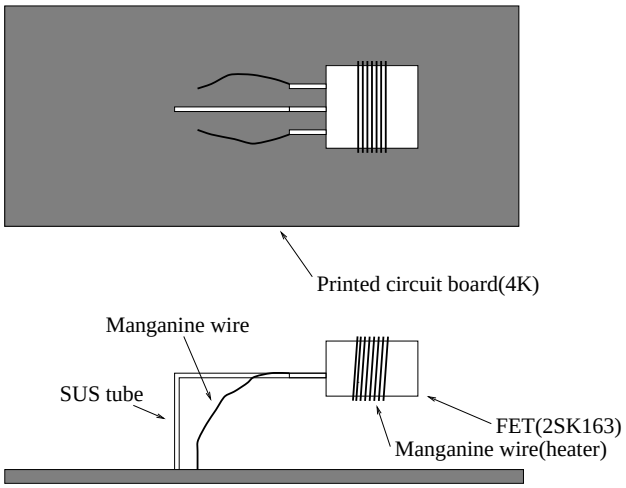

Figure 5.5: Schematic drawing of mounting of the J-FET to the circuit plate. The gate of the J-FET is connected by a stainless steel tube, while the others are connected by manganin wires.

Jacket	FEP	0.05mm^{t}
Inner conductor	tin coated copper	$0.1\text{mm}\phi \times 1$
Insulator	FEP	0.12mm^{t}
Outer conductor	tin coated copper	$0.1\text{mm}\phi \times 14$
Charge noise	< 5pc	10mm amplitude of vibration, 20Hz(JIS C 3501)

Table 5.4: Properties of the low noise coaxial cable used for the cable connecting the dilution refrigerator and the amplifier box. FEP stands for Fluoro Ethylene Propylene.

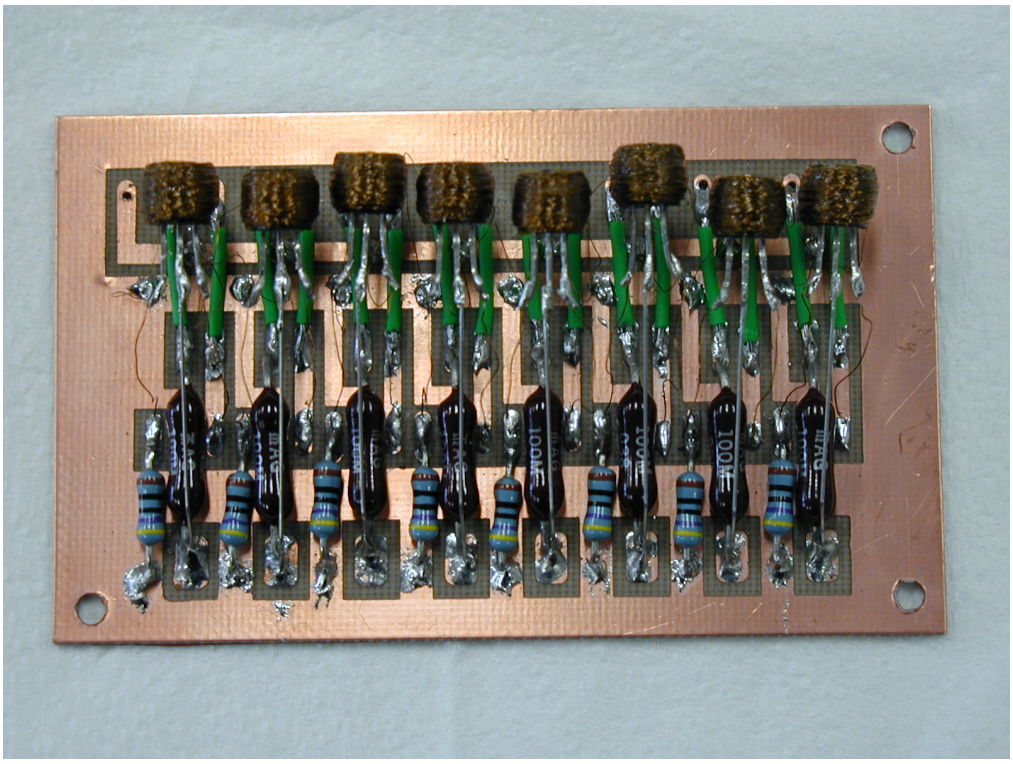

Figure 5.6: Picture of the cold stage amplifier.

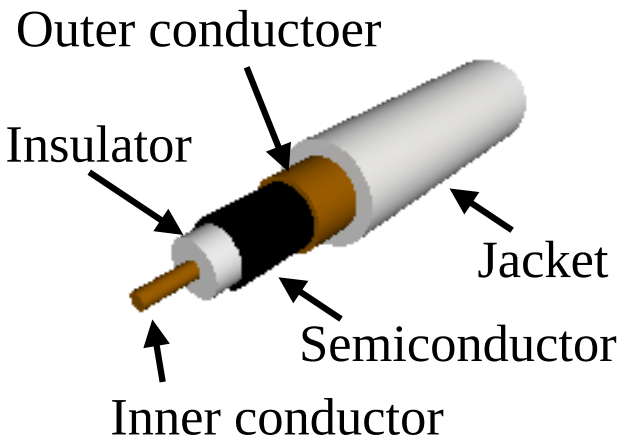

Figure 5.7: Schematic drawing of the low noise cable.

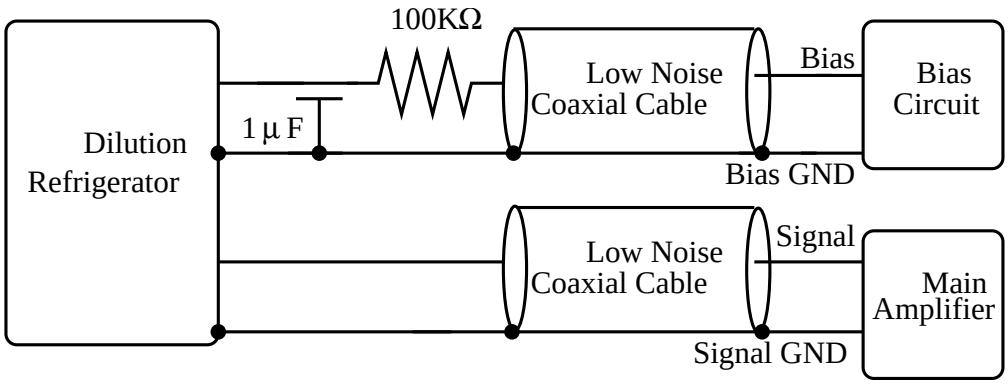

Figure 5.8: Schematic of the electrical circuit of the cable that connects the dilution refrigerator and the amplifier box.(referred to as cable with LPF in Fig. 5.3)

DC bias to the NTDGe thermistor is supplied by the bias current circuit in the room temperature. The schematic of the bias current supply is shown in Fig. 5.9. DC +12V is supplied by the NIM bin and filtered by 2SC1815. The current is adjustable by 200kΩ/2.2kΩ switch and the 1kΩ variable resistance and can be monitored by measuring the voltage across the 10MΩ resistance. The circuit contains a low pass filter with cutoff frequency of 3.4Hz.

As is shown in Fig. 5.4 and Fig. 5.9, we realize a semi-constant current power supply with a high impedance load resistor placed at the 4K stage instead of using a real constant current power supply for the bias current in order to reduce unexpected electric noise. We use a 100MΩ load resistor and the load resistance is inferred to be about 300MΩ at the low temperature. The resistance of the thermistor at 30mK is about 10MΩ and this is not negligible compared to the load resistance. As the load resistor is in series with the thermistor, the response to a $\Delta R_{\rm NTD}$ is expressed as

$$\frac{\Delta R_{\rm NTD}}{R_{\rm load} + R_{\rm NTD}}. \tag{5.1}$$

The responses differ about 3% between the case with $R_{\rm NTD} = 10\mathrm{M}\Omega$ and $R_{\rm NTD}$ is negligibly small. Here, we used $R_{\rm load} = 300\mathrm{M}\Omega$ as a typical value. Thus the ambiguity of the energy due to the non-linearity is estimated to be about 3%.

- Room Temperature Amplifier(main amplifier)
  The signal amplified by the cold stage amplifier is fed to the room temperature amplifier. The schematic of the electrical circuit of this amplifier is shown in Fig. 5.11. The amplifier consists of two stages: A low-noise operational amplifier LT1028 is adopted for the first stage and TL074 for the second. Total noise density of LT1028 as a function of unmatched source resistance is shown in Fig. 5.10. The intrinsic noises of

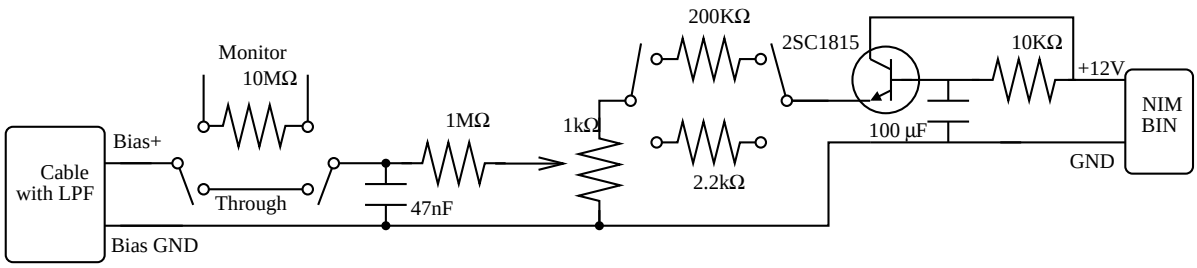

Figure 5.9: Schematic of the electrical circuit of bias current supply. (referred to as bias circuit in Fig. 5.3)

source	Noise density[nV/ $\sqrt{\text{Hz}}$]	Noise level[mV]
$R_{\rm D}$ Nyquist noise	8.8	1.4×10^{-2}
LT1028 noise	$\sim$70	0.1
$R_{\rm NTD}$Nyquist noise	1.1	1.7×10^{-2}
others	2.3	3.7×10^{-2}

Table 5.5: Intrinsic noise contributions of the electric circuit of the bolometer signal. $R_{\rm D}$ = 4.7kΩ is the load resistor of the J-FET. Equivalent rms noise level over Δf=11Hz at the main amplifier output is listed as the 'noise level'. The noise of the J-FET 2SK163 and circuit noises are contained in 'others'[19].

the bolometer circuit are listed in Table 5.5. The voltage gain is 4.86×10^2. The circuit contains the voltage supply and the load resistor of the J-FET voltage amplifier.

- Low Pass Filter
  The bolometer signals amplified by the room temperature amplifier contains noises with frequencies higher than those of the bolometer signal. In order to achieve the low threshold, the signal undergoes through a low pass filter with cut off frequency of 11Hz. The schematic of the electrical circuit of the low pass filter(LPF) is shown in Fig. 5.12. The output of this low pass filter is fed into the VXI multiplexer as shown in Fig.5.3.

5.1.6 LiF Bolometer Array

The bolometer array consists of 8 pieces of LiF crystals. Each crystal is $2 \times 2 \times 2$cm^3 cube and weighs approximately 21g. We refer to each crystal as D1,D2 ..., and D8. Crystals are purchased from two companies for this experiment: D1-D4 are from BICRON Co. Ltd. and D5-D8 are from OHYO KOKEN KOGYO Co. Ltd. The surfaces of the crystals are chemically etched as described in Section 5.2.3. An NTD Ge thermistor is glued to each LiF crystal. NTDGe3 thermistors are used for 6 bolometers and NTDGe2 and NTDGe4 for one

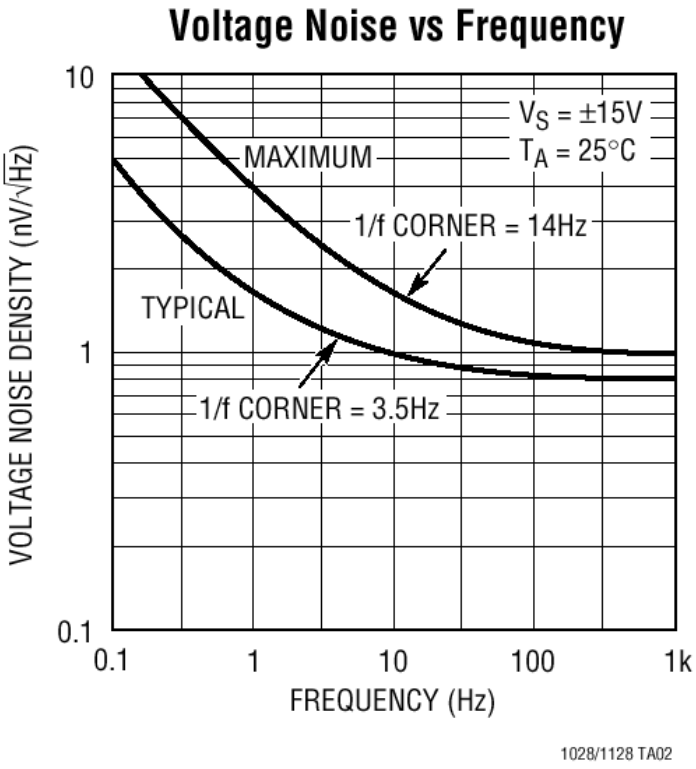

Figure 5.10: Total noise density of LT1028 as a function of unmatched source resistance.

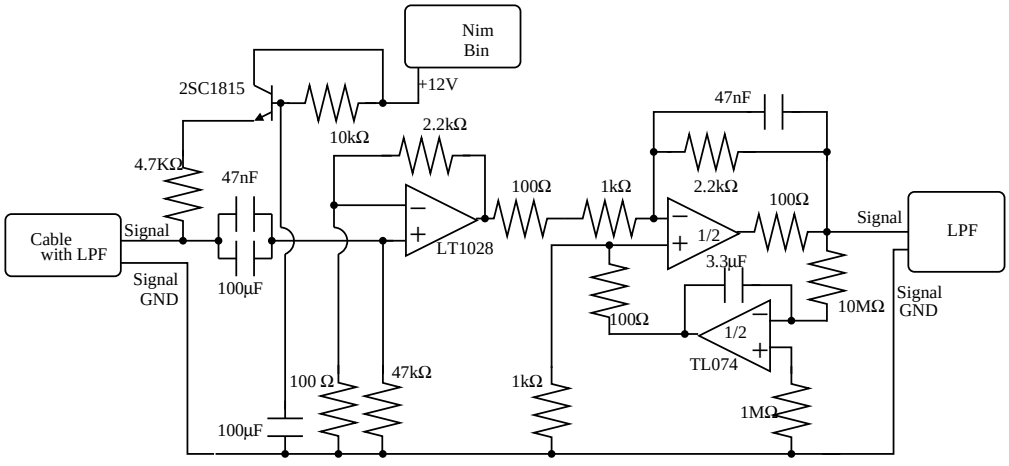

Figure 5.11: Schematic of the electrical circuit of the amplifier at the room temperature.(referred to as main amplifier in Fig. 5.3)Total voltage gain is 4.86×10^2.

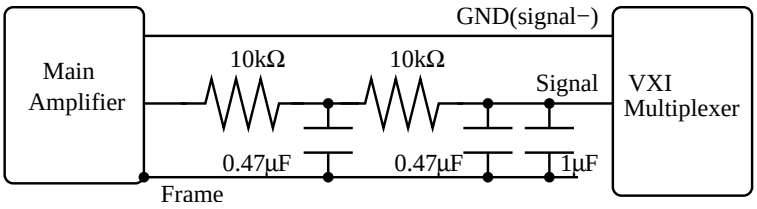

Figure 5.12: Schematic of the electrical circuit of the low pass filter(LPF) for the bolometer signal. (referred to as LPF in Fig. 5.3) Cut-off frequencies of the first and second stage are 33Hz and 11Hz, respectively.

Detector	mass(g)	Etching(μm)	LiF ID	NTDGe ID
D1	20.98	21	BIC1	NTD2-1i
D2	20.98	22	BIC2	NTD3-9r
D3	20.99	26	BIC3	NTD3-4
D4	20.92	29	BIC4	NTD3-7
D5	21.09	22	OK2	NTD4-3i
D6	21.07	24	OK3	NTD3-3r
D7	21.01	27	OK4	NTD3-6
D8	21.00	30	OK5	NTD3-16

Table 5.6: LiF bolometers used for this underground measurement. The etching technique is described in Section 5.2.3.

bolometer, each. The $R-T$ curves are shown in Fig. 4.2. NTDGe3 had been used for all the previous measurements and are considered to have ideal characteristics. In this experiment, NTDGe2 and NTDGe4 are used to check their performances for the future experiments. Precise mass of each detector, depth of the chemical etching, the identifications of the LiF crystal, and the NTD Ge thermistors are listed in Table 5.6. Schematic drawings and the picture of the LiF bolometer array are shown in Fig. 5.13 and Fig. 5.14, respectively. Bolometers in the same stage face to each other over the delrin balls with a diameter of 3.2mm. Thermal connections to the OFHC copper holder are achieved by annealed OFHC copper ribbons of 1cm width and 0.1mm thick.

The LiF crystals are previously checked with low-background Germanium spectrometer and no detectable radioactive contamination is found. The contaminations of the uranium and thorium is further checked by mass spectrometry[69]. The results of the measurement with Ge spectrometer and the mass spectrometry are summarized in Table 5.7.

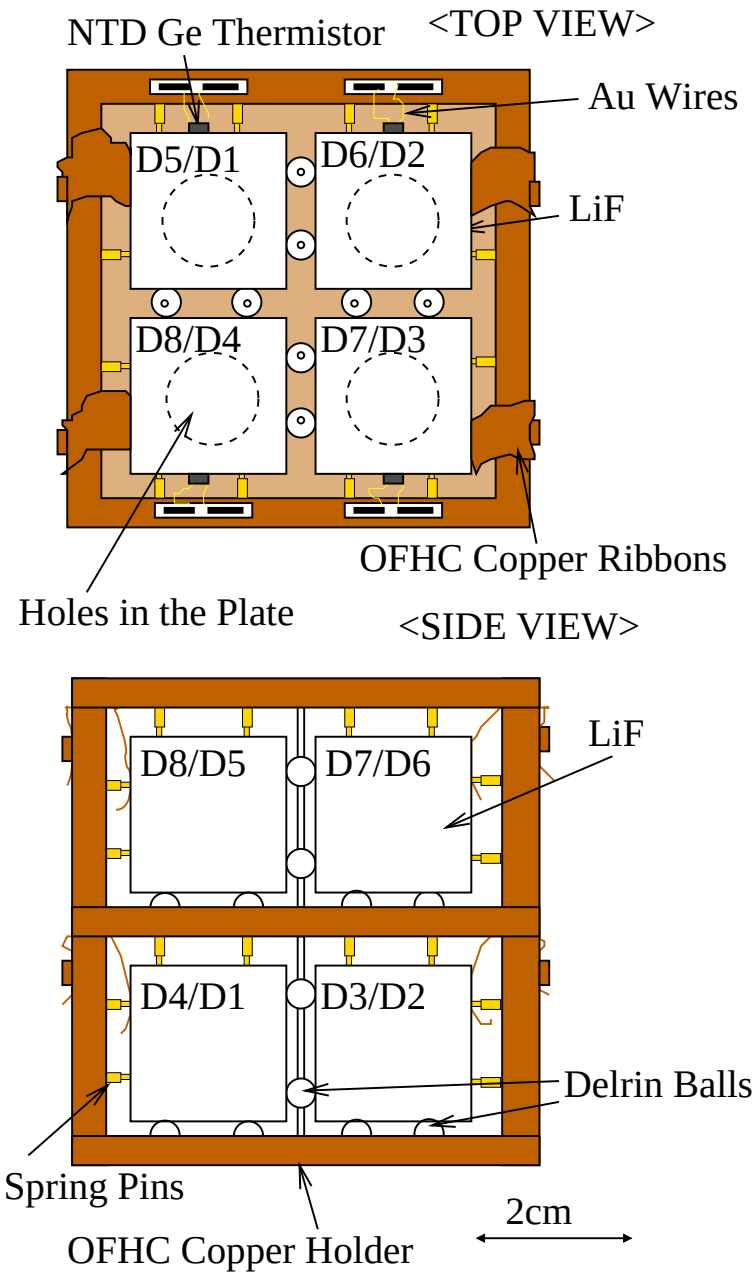

Figure 5.13: Schematic drawings of the bolometer array. D1-D4 are mounted in the lower stage, while D5-D8 are mounted in the upper stage. Bolometers in the same stage face to each other over the delrin balls. There are holes in the copper plate between the two stages.

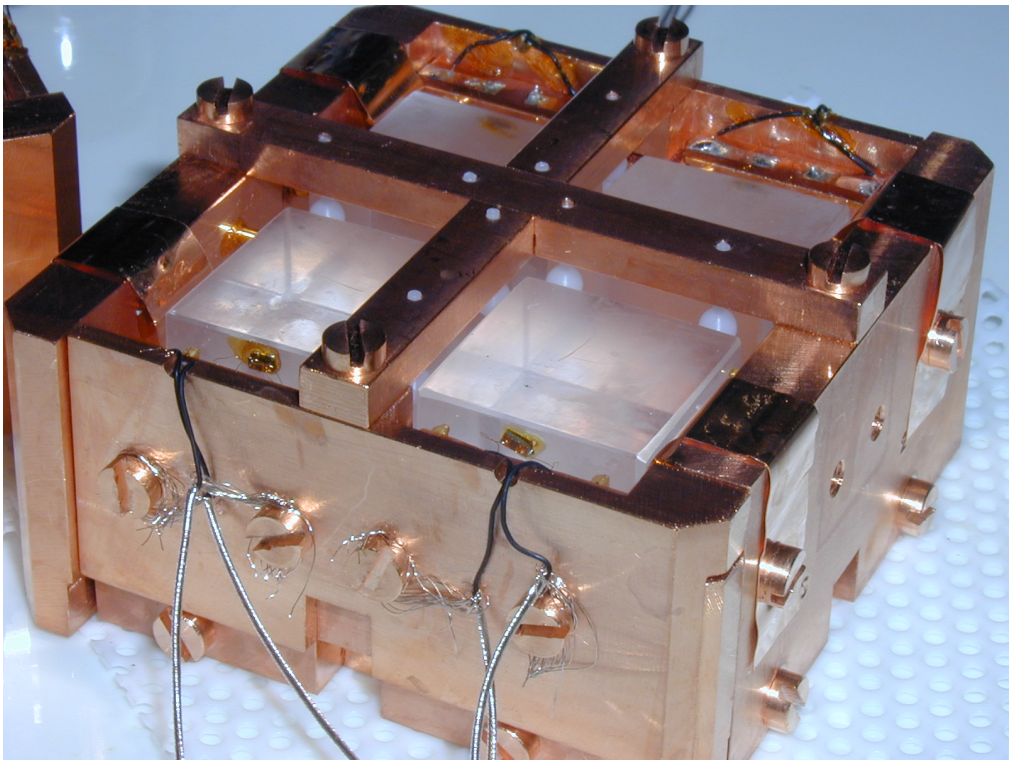

Figure 5.14: Picture of the LiF bolometer array. This is one of the two stages and holds four LiF crystals. NTD Ge thermistors are seen on the side of the LiF crystals. Delrin balls are between the LiF crystals.

Company	Method	^{238}U[ppt]	^{232}Th[ppt]	K[ppm]
OHYO KOKEN KOGYO Co. Ltd.	HPGe	< 200	< 1200	< 2
OHYO KOKEN KOGYO Co. Ltd.	ICP-MS[69]	20	4	-
BICRON Co. Ltd.	HPGe[70]	< 130	< 1700	< 20
BICRON Co. Ltd.	ICP-MS[69]	5	4	–

Table 5.7: Radioactive contamination in the LiF crystals. Note that these values are those before the chemical etching described in Section 5.2.3.

5.2 Techniques for Low Background and Low Threshold Measurement

We made several improvements of the detector for this experiment. These improvements are especially aimed at the low background and low threshold measurement.

5.2.1 Inner Shield

Dilution refrigerators are usually longer than 1 meter and it is not easy to shield them. There are several ways to apply dilution refrigerators for low background measurements[30, 72].

We have designed the 'outer'(room-temperature) shields as shown in Fig.5.2 and also have '4K' shields above the detector. Though the detector is not exposed to the outside directly, the gamma rays back-scattered in the outer shields can reach the detector. It is known that these stray gamma-rays would be the dominant background, when the background due to the cosmic ray becomes negligible in a deep underground laboratory[62].

We have decided to install a 4π 'inner' shield surrounding the detector at the 10mK stage. As we do not have much experimental volume, the thickness of this inner shield is restricted to be less than 2cm. A copper shield would not be enough with a thickness of 2cm, while we can expect a reduction of more than two orders of magnitude with a 2cm lead shield in the energy range of interest.

However, lead has a radioactive isotope ^{210}Pb with half life time of 22.3years as shown in Fig. 5.15. Radioactive isotopes cannot be removed by chemical process: we need to wait for them to decay out. Fortunately we managed to obtain 20kg of old lead that is more than 200 years old[1]. As this lead is from Kanazawa Castle, we refer to this lead as 'Kanazawa lead.'

We checked the radioactive contamination of the Kanazawa lead with HPGe spectrometer. Obtained spectrum is shown in Fig. 5.16. Fluorescent X-rays are not seen in the spectrum of the Kanazawa lead, while those of normal low background lead (Lead C:used for the outer shield) are clearly seen. These X-rays are induced by the gamma and beta rays from the ^{210}Pb contamination.

We have furthermore surveyed the Kanazawa lead by mass spectrometry and the results are shown in Table 5.8.

We fabricated the inner shield with Kanazawa lead by ourselves. Schematic drawings and the picture of inner shield are shown in Fig. 5.17 and Fig. 5.18. The shield consists of three part: the top plate, cylindrical part, and the bottom part. Total mass of the inner shield is approximately 12kg.

[1]Professor Komura at Kanazawa University possessed some old lead used for the Kanazawa Castle and have kindly provided us with 20kg of this precious lead for this experiment.

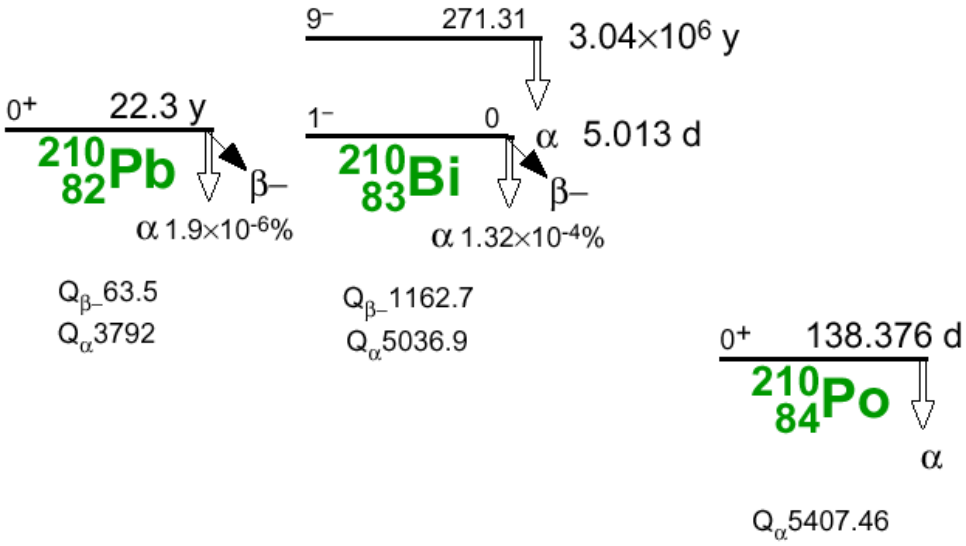

Figure 5.15: Decay scheme of ^{210}Pb.[71]

^{238}U[ppb]	^{232}Th[ppb]	K[ppm]	^{210}Pb[pCi/g]	Method
< 0.1	1.4	-	-	ICP-MS[73]
< 0.5	< 0.5	-	-	ICP-MS[74]
-	-	< 1	-	GDS[75]
		-	< 0.05	HPGe

Table 5.8: Radioactive contamination in Kanazawa lead.

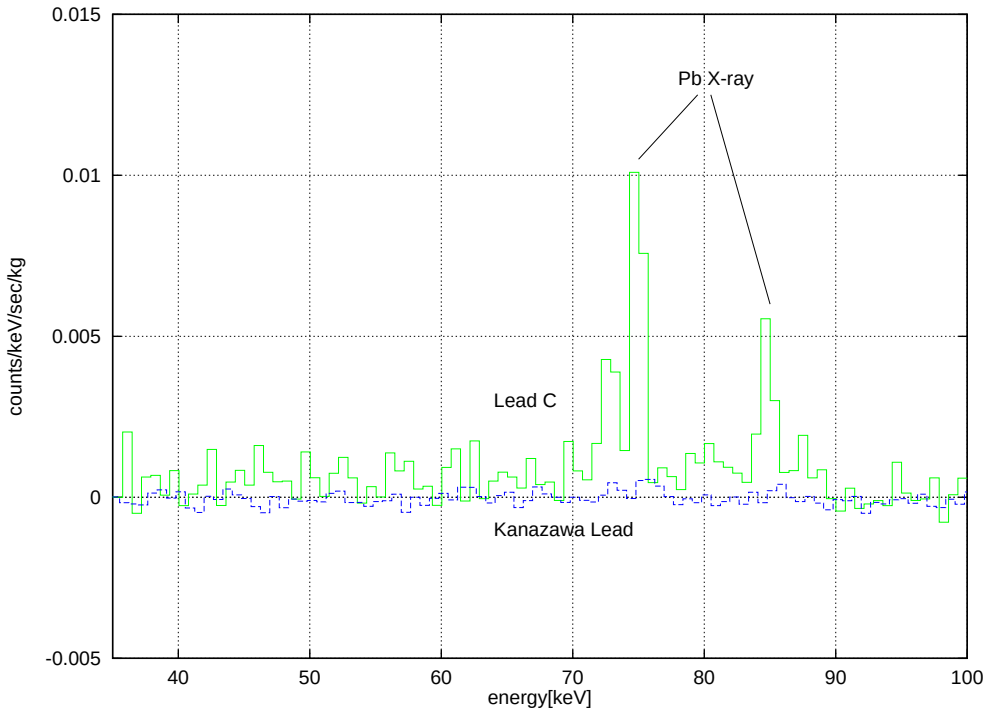

Figure 5.16: Spectrum of Kanazawa lead obtained with HPGe spectrometer. The spectrum of the normal low background lead (Lead C) used for the outer shield is also shown.

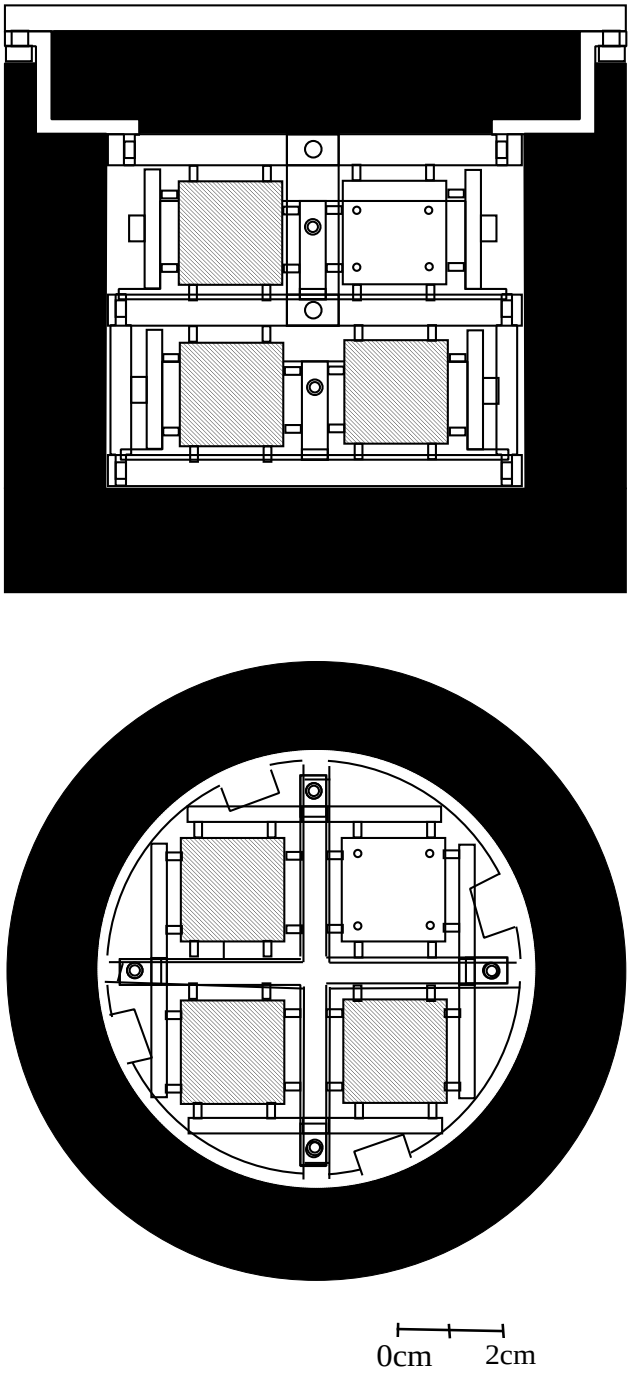

Figure 5.17: Schematic drawings of the inner shield. The shield is shown in black in the drawings.

Figure 5.18: Picture of the inner shield. The bolometer array is encapsulated in the Kanazawa lead of 2cm thick.

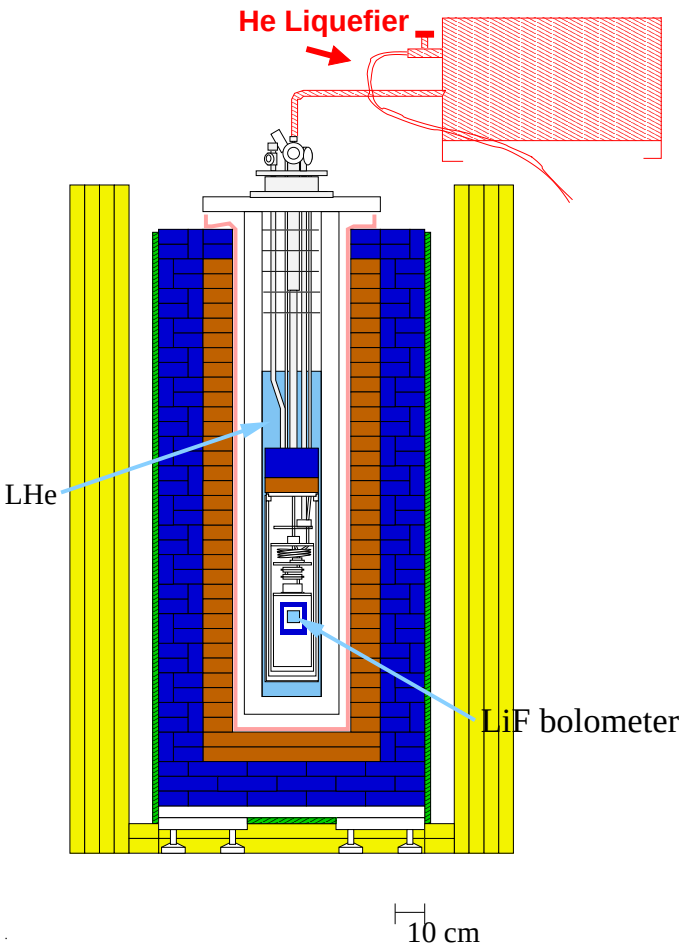

Figure 5.19: Schematic drawing of the detector set up. The helium liquefier is shown in red.

5.2.2 Suspending the Bolometer Array with Kevlar Cords

We have installed the inner shield and found that vibration noise became much more serious than before. The bolometer array with the crystal holder weighs about 1.5kg without the inner shield. As the inner shield weighs 12kg, the detector becomes one order of magnitude heavier with the inner shield. The bolometer array and the inner shield is screwed to the bottom of the 1.5m-long dilution refrigerator. The dilution refrigerator is bolted only on the top to avoid unnecessary heat leak, so the dilution refrigerator acts like a pendulum. The heavier the mass, the more sensitive to the vibration.

The most serious source of the vibration is the helium liquefier settled above the dilution refrigerator. The configuration is shown in Fig. 5.19. The disturbance of the bolometer signal by the helium liquefier is shown in Fig. 5.20.

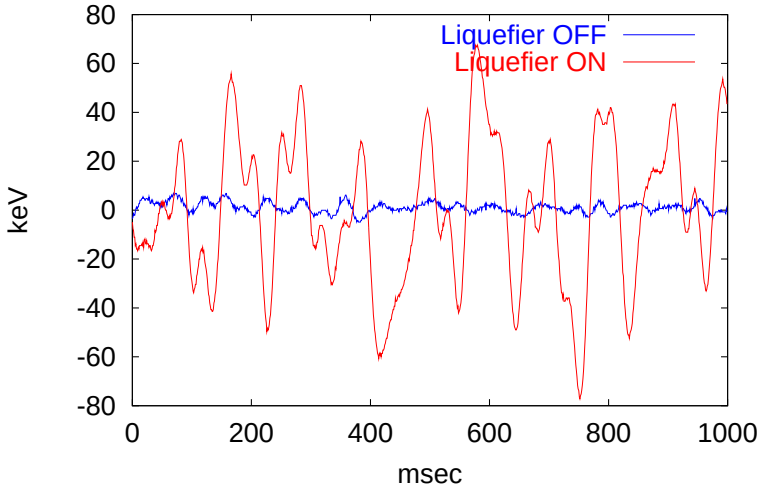

Figure 5.20: Bolometer signals with helium liquefier on and off. Bolometer array is simply screwed to the bottom of the dilution refrigerator. Signal to noise ratio gets worse by more than 1 order of magnitude.

The signal to noise ratio becomes worse by more than 1 order of magnitude when we run the helium liquefier. We were not able to take data with helium liquefier running in the preliminary measurement at Kamioka Observatory(Kamioka-run4), therefore we stopped the helium liquefier and took data re-filling the helium bath every day. The data shown in Section 4.5 were taken without the helium liquefier.

We knew that we need to operate helium liquefier to take long-time and uninterrupted data. Attempts of reducing the vibration noise were done in the test runs at Kamioka Observatory, which didn't make much effect(Section A.5 and Section A.6). Then we decided to suspend the bolometer array from the bottom of the dilution refrigerator with kevlar cords. Properties of the kevlar cord adopted for this experiment are listed in Table 5.9.

As the experimental volume is restricted, the length of the kevlar cords was determined to be 8cm. The resonance frequency is 1.8 Hz for the horizontal oscillation, which is low enough for the bolometer signal, and more than three orders of magnitude reduction is expected for the 10 Hz vibration. For the vertical vibration, the spring constant becomes smaller by more than two orders of magnitude compared to the former method of screwing the bolometer array to the dilution refrigerator.

Schematic drawing of suspended bolometer array is shown in Fig. 5.21. The bolometer array is suspended with three kevlar cords of 0.8mm diameter and thermal link is achieved by annealed 4 OFHC copper ribbons of 10mm $\times$ 120mm $\times$ 0.15mm each.

This improvement was first adopted for Kamioka-run8 (summarized in Appendix A.8). Signals of the bolometer in Kamioka-run8 with the helium liquefier on and off are shown in

Diameter(mm)	0.8
Breaking load (kg)	75
Tensile Modulus (GPa)	59-124
Tensile Strength (MPa)	2760
Acids - concentrated	Poor
Acids - dilute	Fair
Alcohols	Good
Alkalis	Good
Greases and Oils	Good
Ketones	Good

Table 5.9: Physical and chemical properties of the kevlar cord adopted for this experiment[76].

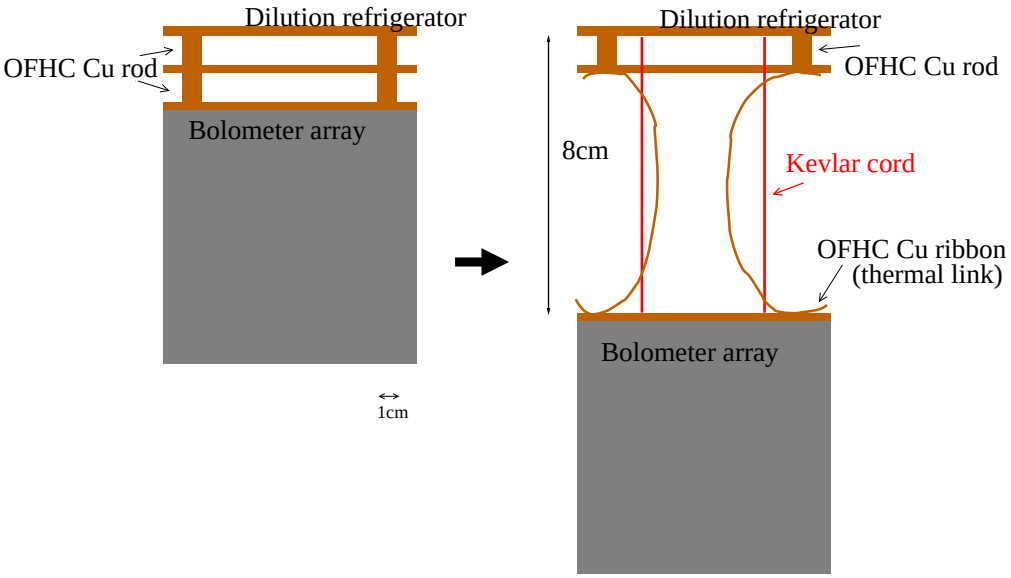

Figure 5.21: Schematic drawings of the simply screwed bolometer array(left) and suspended bolometer array(right). Kevlar cords are shown in red.

Figure 5.22: Picture of the bolometer array (only the inner shield is seen) suspended with kevlar cords. Three kevlar cords of yellow color are seen and copper ribbons are seen in the center. The signal lines are seen is the very left.

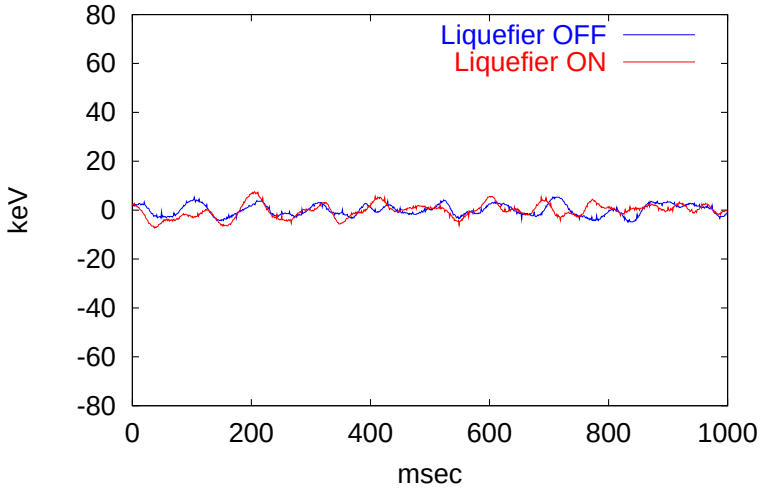

Figure 5.23: Bolometer signals with helium liquefier on and off. Bolometers are suspended with kevlar cords. No difference is seen between the two signals.

Polishing powder	U[10^{-9}g/g]	Th[10^{-9}g/g]	K[10^{-6}g/g]
OK-1(Morundum AZ)	131±1.8	94.4±3.1	1.1±0.21
OK-2(diaslurry)	0.36±0.15	0.63±0.33	<0.44
BICRON	< 22.0	0.31 ± 0.21	6.92 ± 0.34

Table 5.10: Contamination of U, Th, and K in the polishing powders[79]. OK-1 is used first and then OK-2 is used for the finishing at OHYO KOKEN KOGYO Co. Ltd., while only BICRON is used at BICRON Co. Ltd.

Fig. 5.23. No difference is seen between the data with the helium liquefier on and off.

Another date show the effect of this improvement. Details are described in Appendix C.

5.2.3 Chemical Etching of the LiF Crystals

From the preliminary measurement at Kamioka Observatory, we found that the background level of our detector is still high for the dark matter detection (shown in Fig.4.8). High energy spectrum obtained by one of the detectors (D8) in the preliminary underground measurement is shown in Fig. 5.24. Clear peaks due to α decays of ^{238}U and ^{232}Th chains are seen.

We surveyed the polishing powder used for the manufacturing process with HPGe spectrometer and a significant amount of contamination is detected as listed in Table 5.10.

We found by simulation that if grains of this polishing powder remain on the surface of the LiF crystal, they would be enough source to explain the background in the low energy

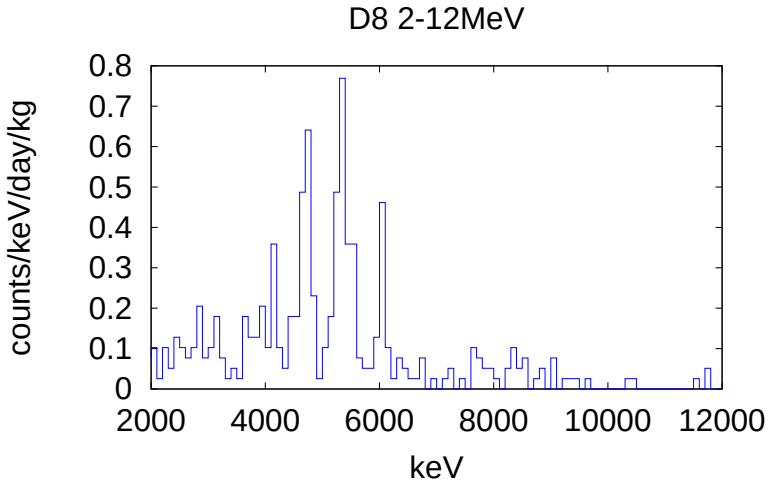

Figure 5.24: High energy spectrum obtained by one of the detectors(D8) in the preliminary measurement at Kamioka Observatory. The exposure is 0.27 kg·days.

region[79].

In order to know if the contamination is really on the surface, we etched the surface of the LiF crystals with perchloric acid ($HClO_4$) and performed a test run (Kamioka-run5:summarized in Appendix A.5). The depth of the etching is about $2\mu m$. Pictures of the LiF crystal before and after the etching are shown in Fig. 5.25. Transparency of the crystal is lost by the etching.

In the test run with etched LiF crystals, we confirmed that they work as bolometers properly and the obtained spectrum with one of the detectors(D5) is shown in Fig. 5.26. Effect of the etching is confirmed as the peaks are reduced, while it is found that 2 μm depth might not be enough.

Considering the result of the test run, we etched all the LiF crystals used for this underground experiment. Perchloric acid, TAMAPURE-AA-100 in which each metallic impurity level is guaranteed to be 100 ppt or less, is used for the etching. The etching was performed with Teflon instruments as shown in Fig. 5.27. Depth of the etching for each crystal is listed in Table 5.6.

5.2.4 Radon Purge

The mine air contains radon gas that is radioactive and could be a serious background source. Special care was taken against the radon gas. The detector system is shielded by two layers of radon shield: the laboratory atmosphere and the nitrogen gas. Radon concentration in the mine air are high and have a seasonal change. As the bolometer crystals are exposed to

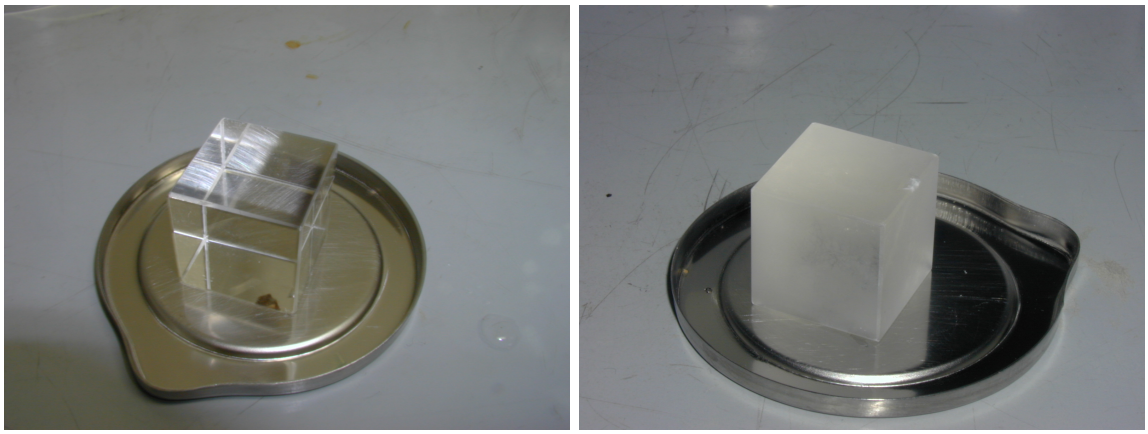

Figure 5.25: Pictures of the LiF crystal before(left) and after(right) the etching with perchloric acid.

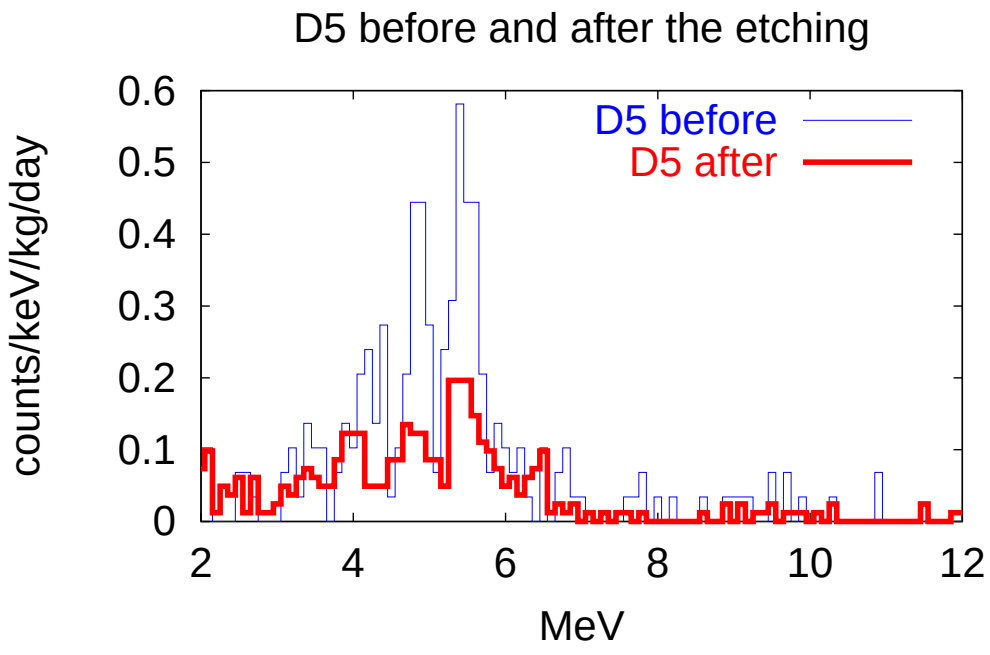

Figure 5.26: Spectra obtained by one of the detectors(D5) before and after the etching. The exposure is 0.27 kg·days and 0.78 kg·days for the before and after measurement, respectively. α peaks are reduced.

Figure 5.27: Etching the LiF crystals with perchloric acid.

the room atmosphere during the assembly, we don't want the mine air in the laboratory. Air from outside the mine is taken through pipes and is blown into the laboratory with rate of $1\mathrm{m}^3/\mathrm{min}$.

Some of the air from outside of the mine is fed into a radon free air generator to remove still remaining radon gas in it. The output of the radon free air generator is released in front of the liquid nitrogen generator. Liquid nitrogen are generated from the radon free air and the evaporated nitrogen gas are used to purge the space between the heavy shield and the dilution refrigerator.

Radon concentration of the room air and the nitrogen gas are monitored throughout the measurement. Radon concentration in the room air and nitrogen gas throughout the measurement was between 10 and 50 Bq/m^3 and less than 0.2 Bq/m^3, respectively.

5.3 Measurements

With the detector system described in Section 5.1 and 5.2, we performed the dark matter search experiment (Kamioka run 9, or this underground dark matter experiment) at Kamioka Observatory. Run data of the measurement are summarized in Table 5.11.

As our dilution refrigerator needs a maintenance every 5-7 days, typical 'one-set' of dark matter measurement consists of 5 short 'periods' as shown in Table 5.12. We calibrate the detector with $^{137}\mathrm{Cs}$ before and after one dark matter period. Linearity is confirmed with $^{60}\mathrm{Co}$ for every dark matter period. The running status through the whole measurement period is

Refrigeration Start	October 12, 2001
Measurement Start	November 22, 2001
Shutdown	January 12, 2002

Table 5.11: Run data of this dark matter search experiment.

shown in Fig. 5.28.

period	time
^{60}Co Calibration	$\sim$ 15hours
^{137}Cs Calibration	$\sim$ 7hours
Dark Matter Run	3-5days
^{137}CsCalibration	$\sim$ 5hours
Maintenance	1-2hours

Table 5.12: Typical 'one-set' of a dark matter search measurement.

5.4 Detector Response

5.4.1 Bolometer Signals

Typical signals of the eight bolometers are shown in Fig. 5.29. D5 has poor signal to noise ratio, because NTDGe4, whose resistance is small as shown in Fig. 4.2, is used for the test. As D5 cannot be calibrated, we'll not use this detector for the following discussions.

Each detector has its own time constant according to the thermal coupling between the crystal and the thermistor, the crystal and the refrigerator, and other mounting conditions. These conditions further cause the differences of the gains, resolutions, and thresholds among the eight bolometers, which are shown in the following sections.

5.4.2 Bias Current and Signals of the Detectors

We detect the resistance decrease of the thermistor as the voltage change by supplying constant bias current. The voltage change is proportional to the bias current at the low bias current, while the dependency reverses at the high bias current, because the resistance becomes small by the Joule's heat. Therefore there is an optimum value of the bias current according to the mounting conditions. The bias current is measured with KEITHLEY MODEL 2002 multimeter by the voltage across the 10MΩ 'Monitor' resistance in Fig.5.11. The bias dependence of the signal to noise ratio is shown in Fig. 5.30. Here the signal is the pulse height

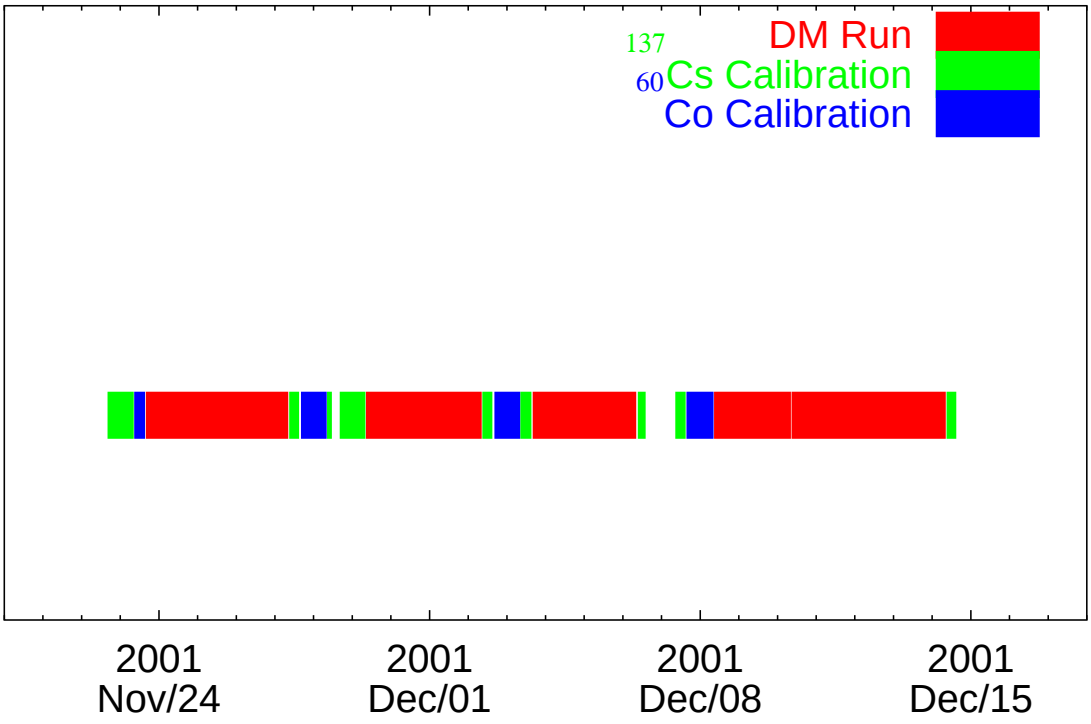

Figure 5.28: Running status through the whole measurement period.

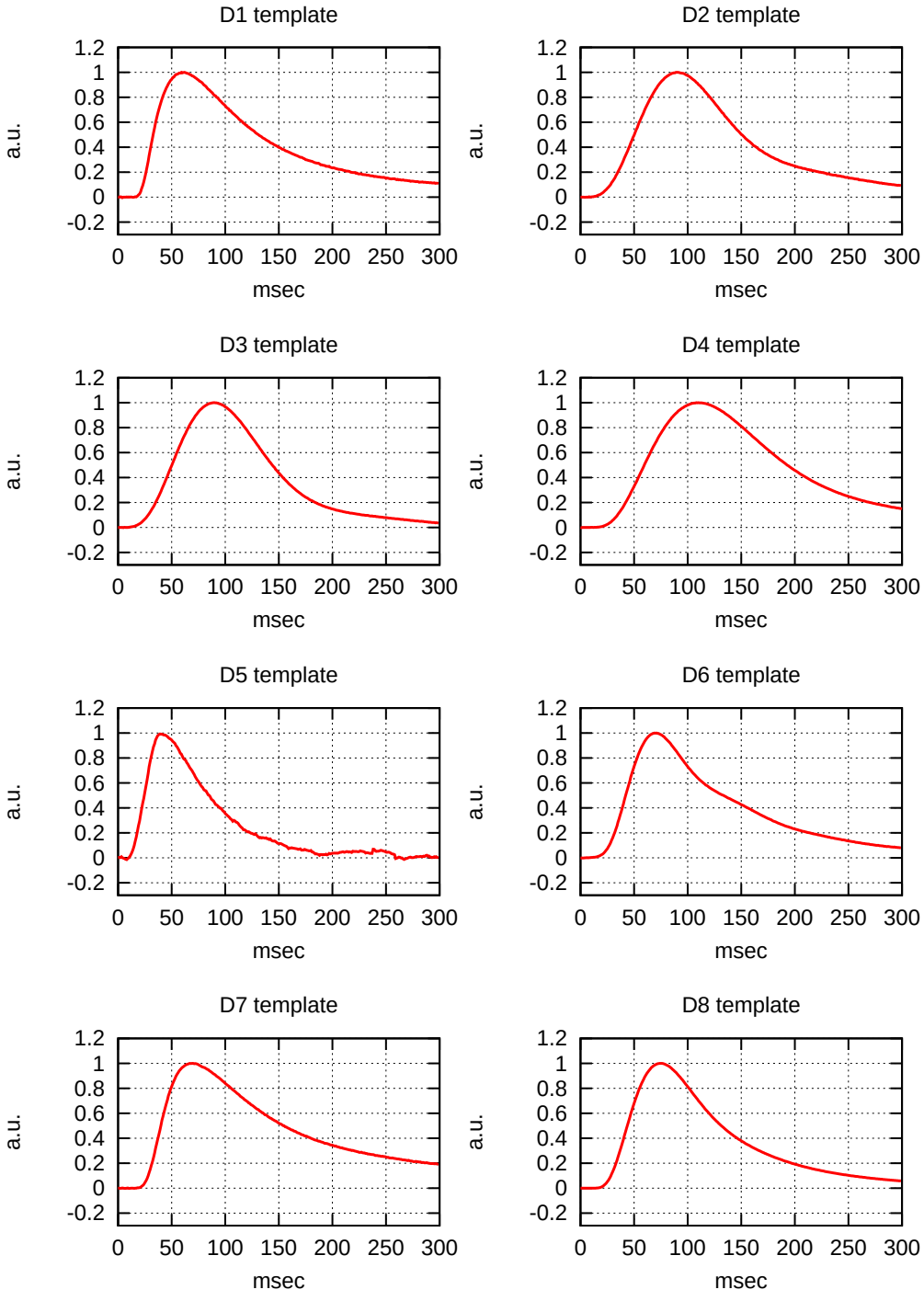

Figure 5.29: Typical signals of the eight bolometers.

corresponding to the Compton edge of the γ-ray from the ^{60}Co source and the trigger level with 1Hz of event rate is taken as the noise level.

Values of the bias current used for the measurement are listed in Table 5.13.

Detector	D1	D2	D3	D4	D6	D7	D8
Bias Current[nA]	0.1	0.05	0.04	0.05	0.05	0.09	0.07

Table 5.13: Bias current of the eight bolometers. Values are also shown in Fig. 5.30 by the red arrows.

5.4.3 Calibration

Calibration of the bolometers are carried out by irradiating γ-ray sources suspended between the heavy shield and the dilution refrigerator. Schematic drawing of the calibration is shown in Fig.5.31.

γ-ray sources used for the calibration are listed in Table 5.14. Compton edges are used for the calibration as γ-rays with these energies do not make enough photoelectoric absorption peaks due to the small atomic numbers of LiF.

source	γ-ray energy[keV]	Compton edge[keV]
^{137}Cs	662	478
^{60}Co	1178	963
	1333	1119

Table 5.14: γ-ray sources used for the calibration. Compton edge energies are also shown.

Calibration data are analyzed by the same manner as the data of the dark matter run. Precise description on the analysis is described in Section 6. Obtained energy spectra with the sources are shown in Fig. 5.32 and 5.33. Clear Compton edges and good agreements with the simulation are seen. The slight differences between the simulation results and the obtained spectra at the lower energy regions are due to the pile up events that are not estimated by simulations well. Calibration lines are obtained from these results and are shown in Fig. 5.34. Good linearities are seen for all of the seven detectors. Linearity down to 60 keV is previously confirmed by mounting the radiation source in the cryogenics[61]. Obtained gains are listed in Table 5.15. Gains are within the range of factor 7 except D1 whose thermistor is NTDGe2.

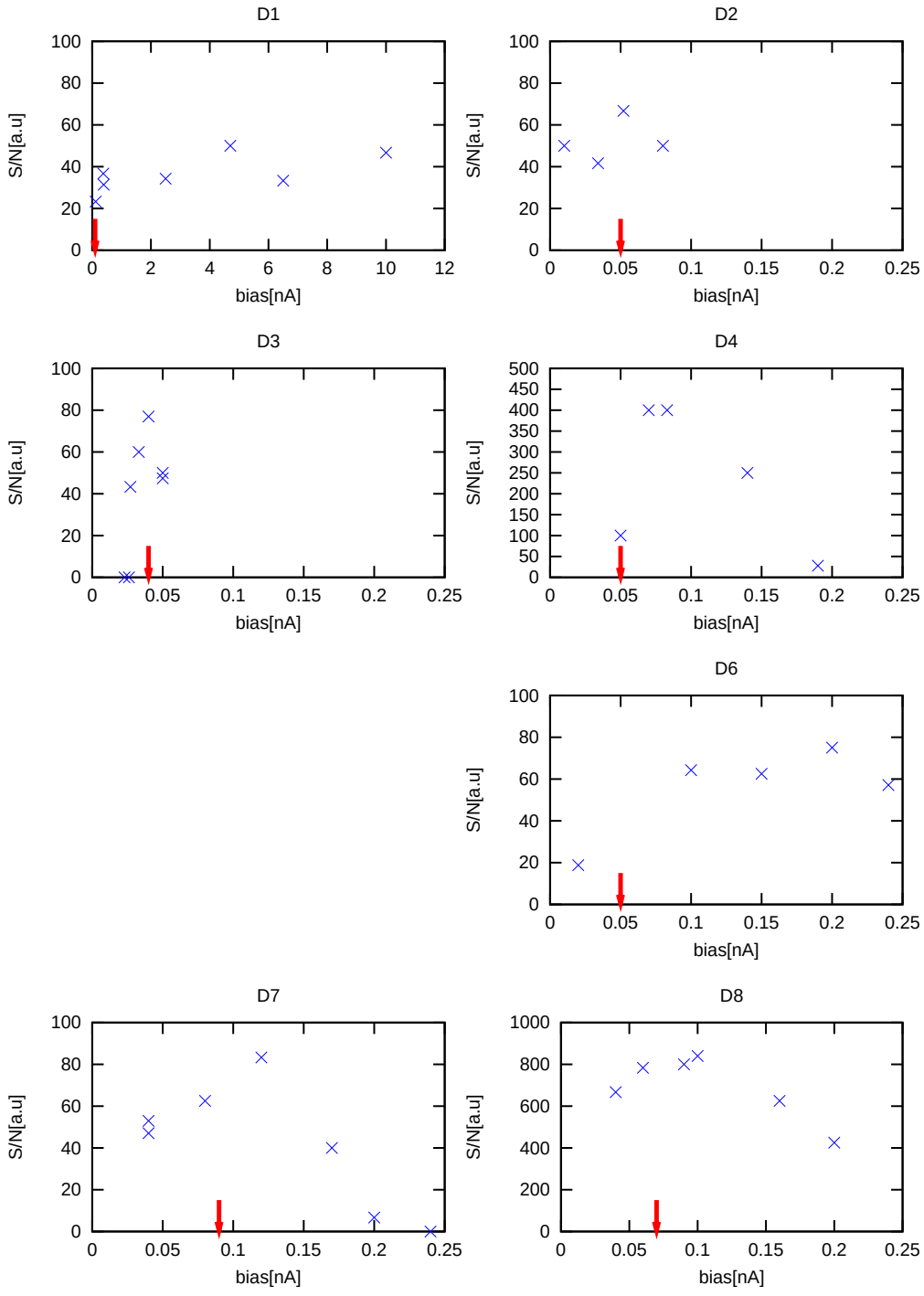

Figure 5.30: Bias current dependence of the signal to noise ratio. Values of the bias current used for the measurement are shown in red arrow. Some bolometers are set to the bias which are smaller than the best value in the figure for the sake of the stability.

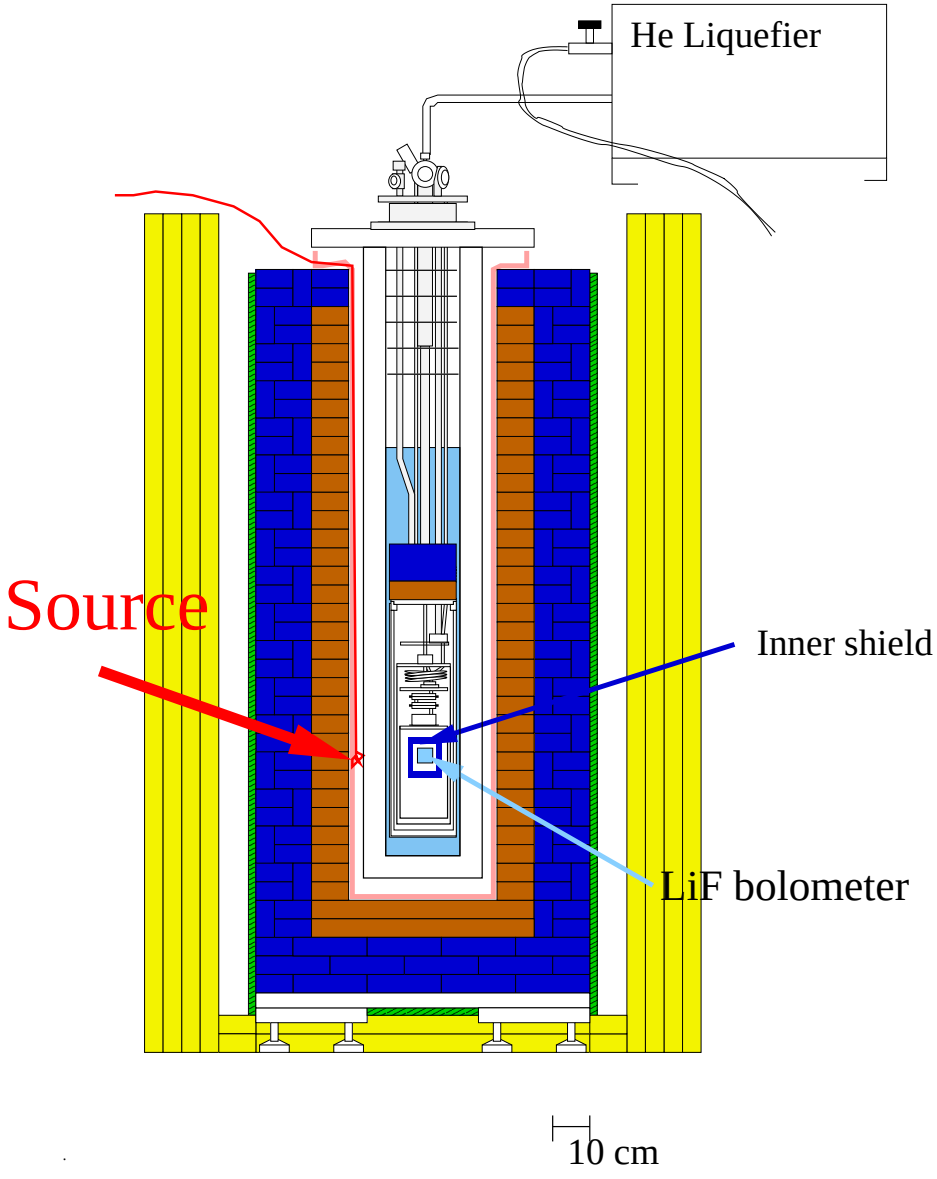

Figure 5.31: Schematic drawing of irradiating the γ-ray source.

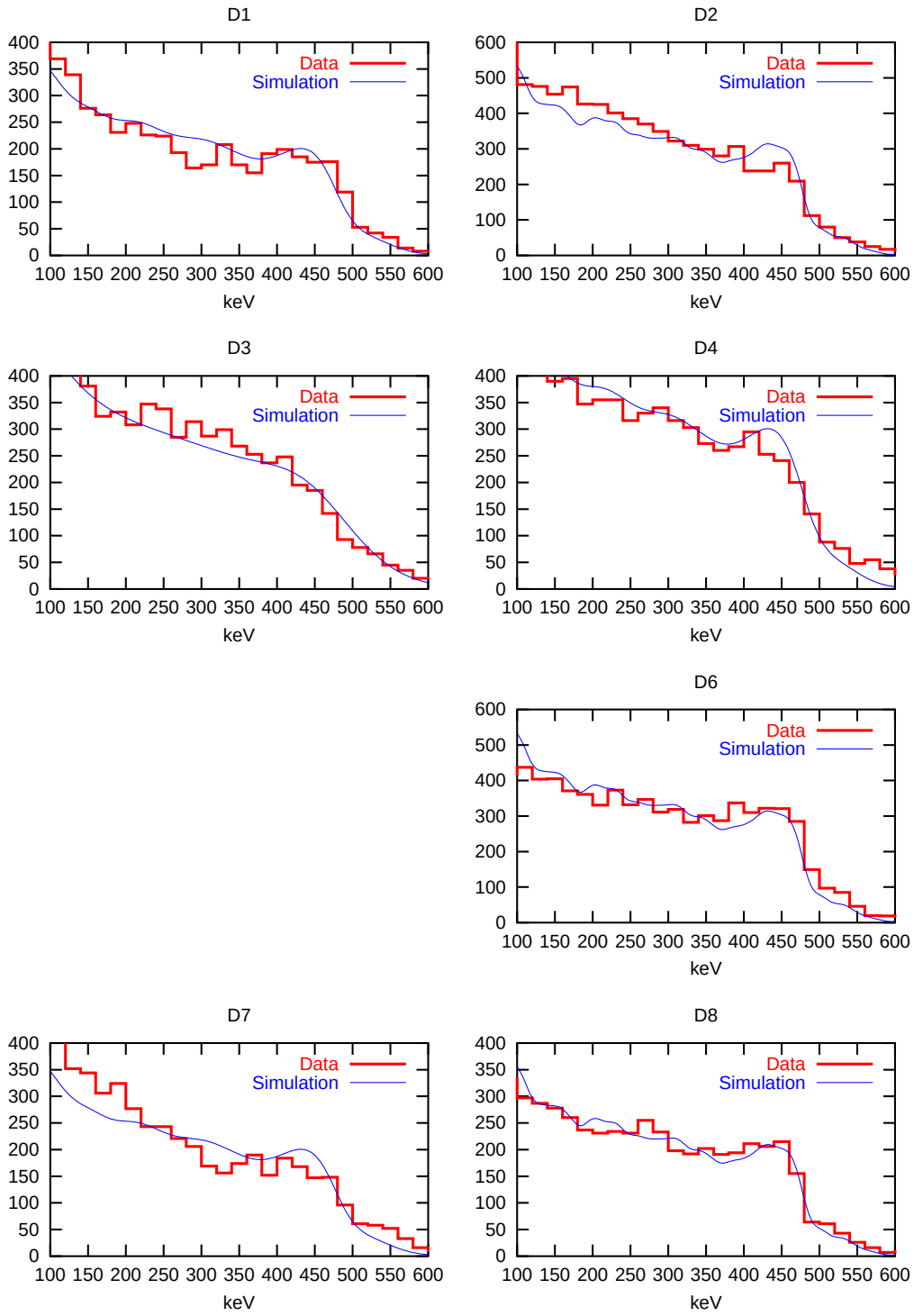

Figure 5.32: Obtained energy spectra with ^{137}Cs source. Simulation results are also shown in blue lines[79].

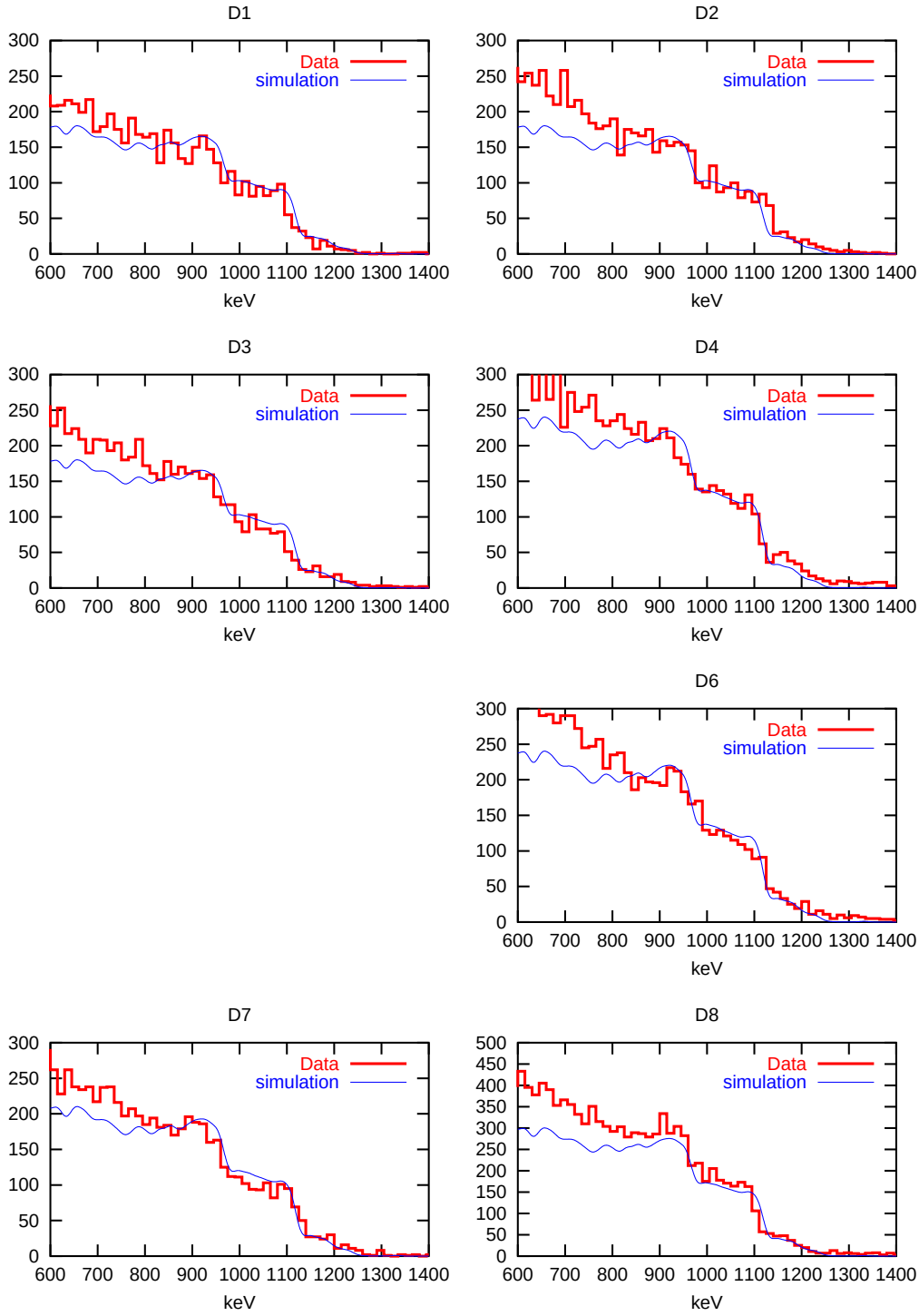

Figure 5.33: Obtained energy spectra with ^{60}Co source. Simulation results are also shown in blue lines[79].

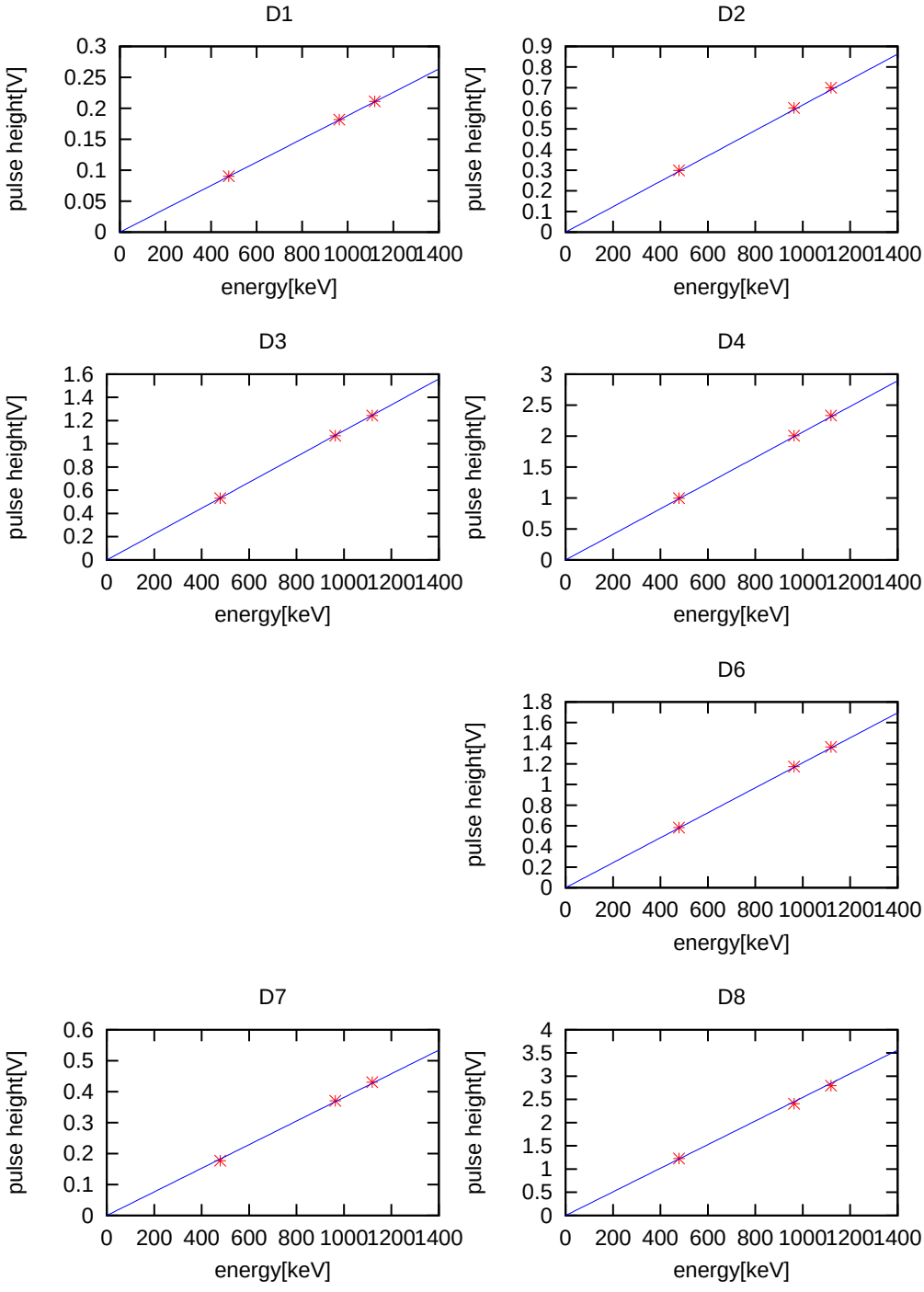

Figure 5.34: Obtained energy calibration lines. Good linearities are seen.

Detector	D1	D2	D3	D4	D6	D7	D8
Gain[V/MeV]	0.18	0.62	1.1	2.1	1.2	0.38	2.5

Table 5.15: Gains of the seven bolometers.

5.4.4 Energy Resolution

As the bolometer is shielded by 2cm thick inner shield, it is hard to irradiate the bolometers with low energy γ-rays. As the resolution of the bolometer is in principle governed by the baseline fluctuation, the energy resolution can be estimated by adding scaled template pulses to the raw data. Typical simulation results near the thresholds are shown in Fig. 5.35 and resolutions for various energies are shown in Fig. 5.36. Averaged values of the estimated resolution are shown in Table 5.16.

Detector	D1	D2	D3	D4	D6	D7	D8
Resolution(FWHM)[keV]	45	13	8.0	10	3.5	7.8	1.9

Table 5.16: Estimated resolution near the threshold.

5.4.5 Stability of the Bolometers

The stability of the bolometer is confirmed by calibrating the bolometer constantly throughout the measurement time. The result of the stability checks is shown in Fig.5.37. We can see the good stabilities of the bolometer gains within $\pm 5\%$.

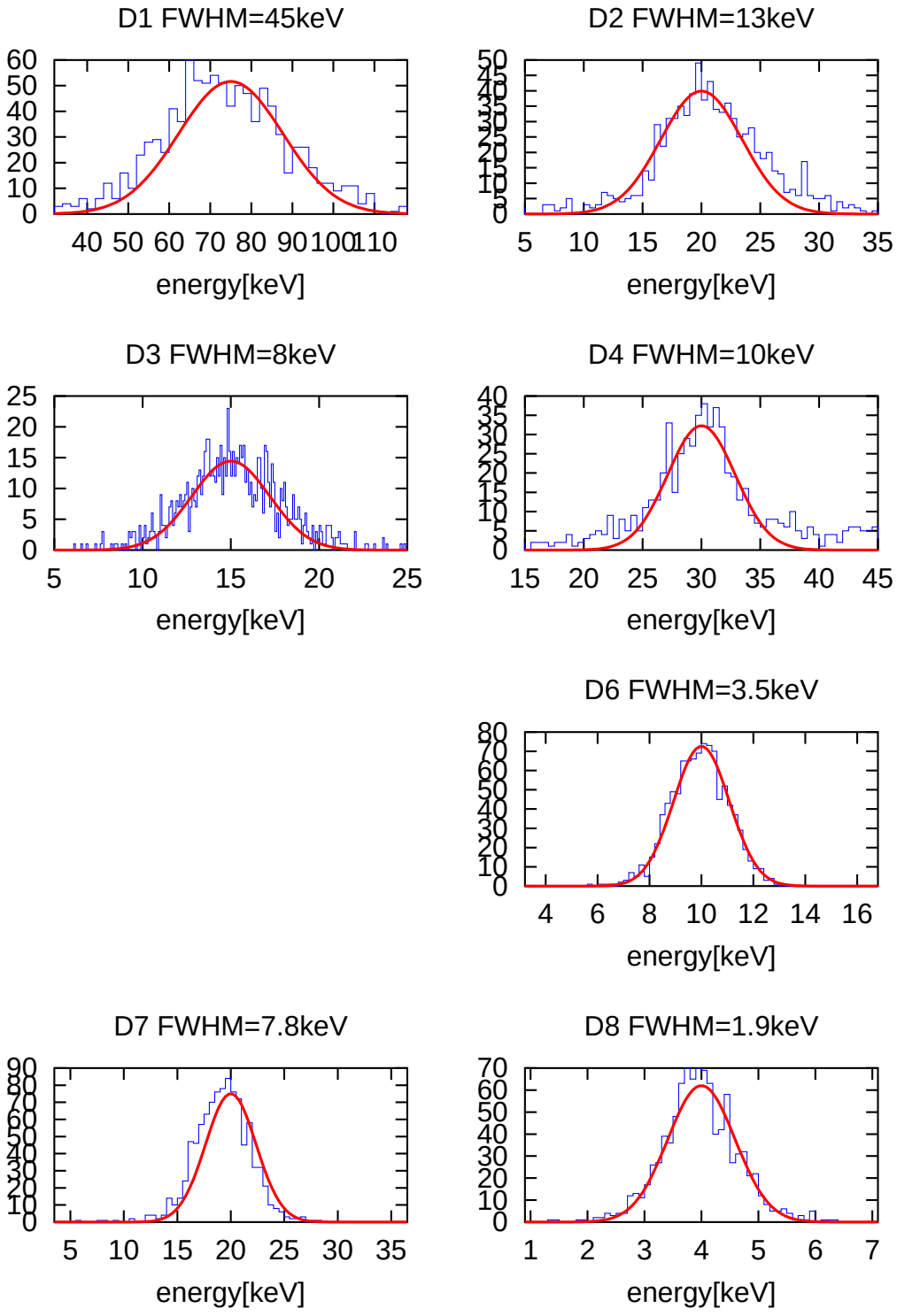

Figure 5.35: Typical simulated resolutions near the threshold. Best fit gaussians are shown in red.

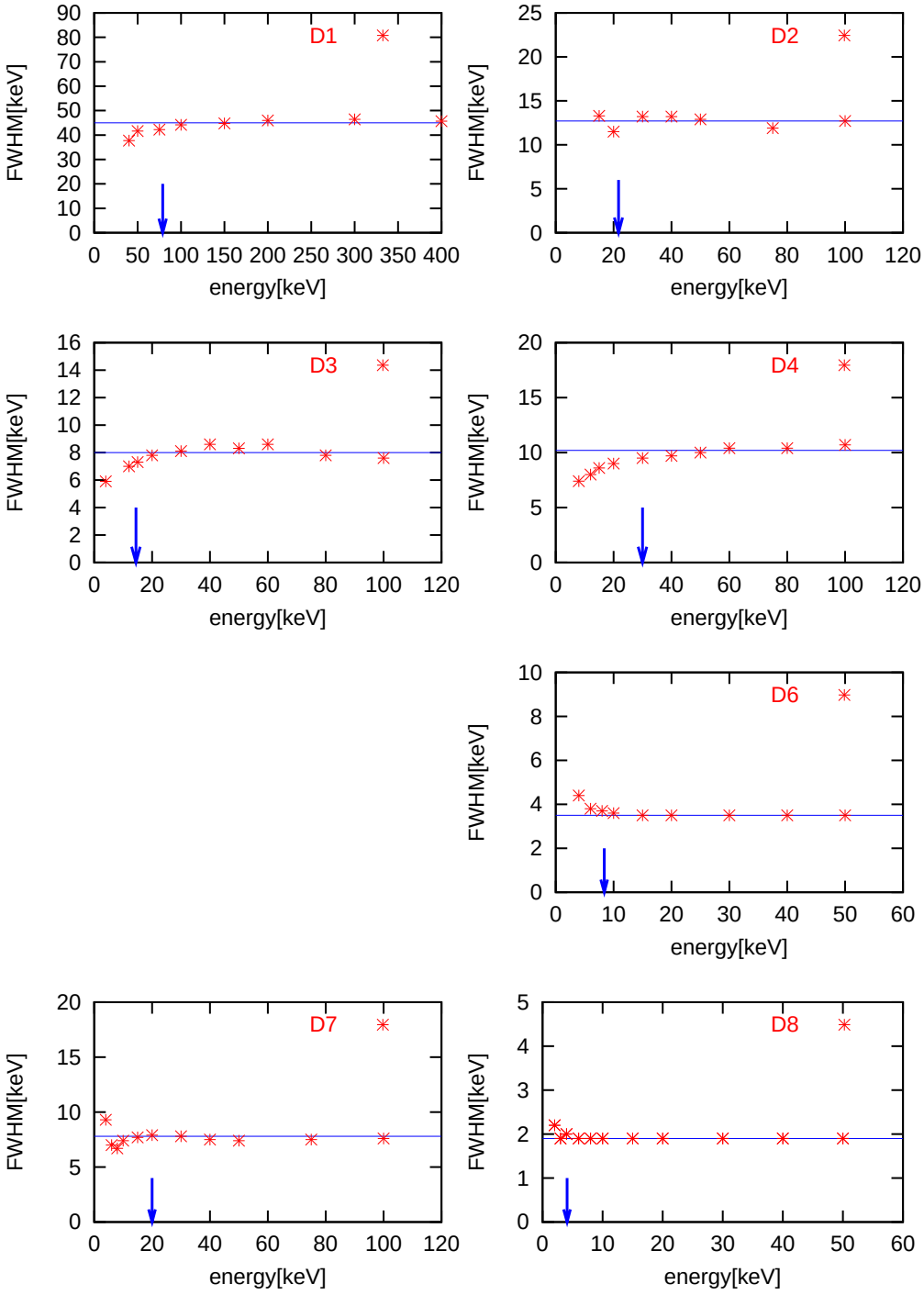

Figure 5.36: Simulated resolutions near the threshold. Thresholds(listed in Table 6.6) are shown in blue arrows and averaged values are shown in blue lines.

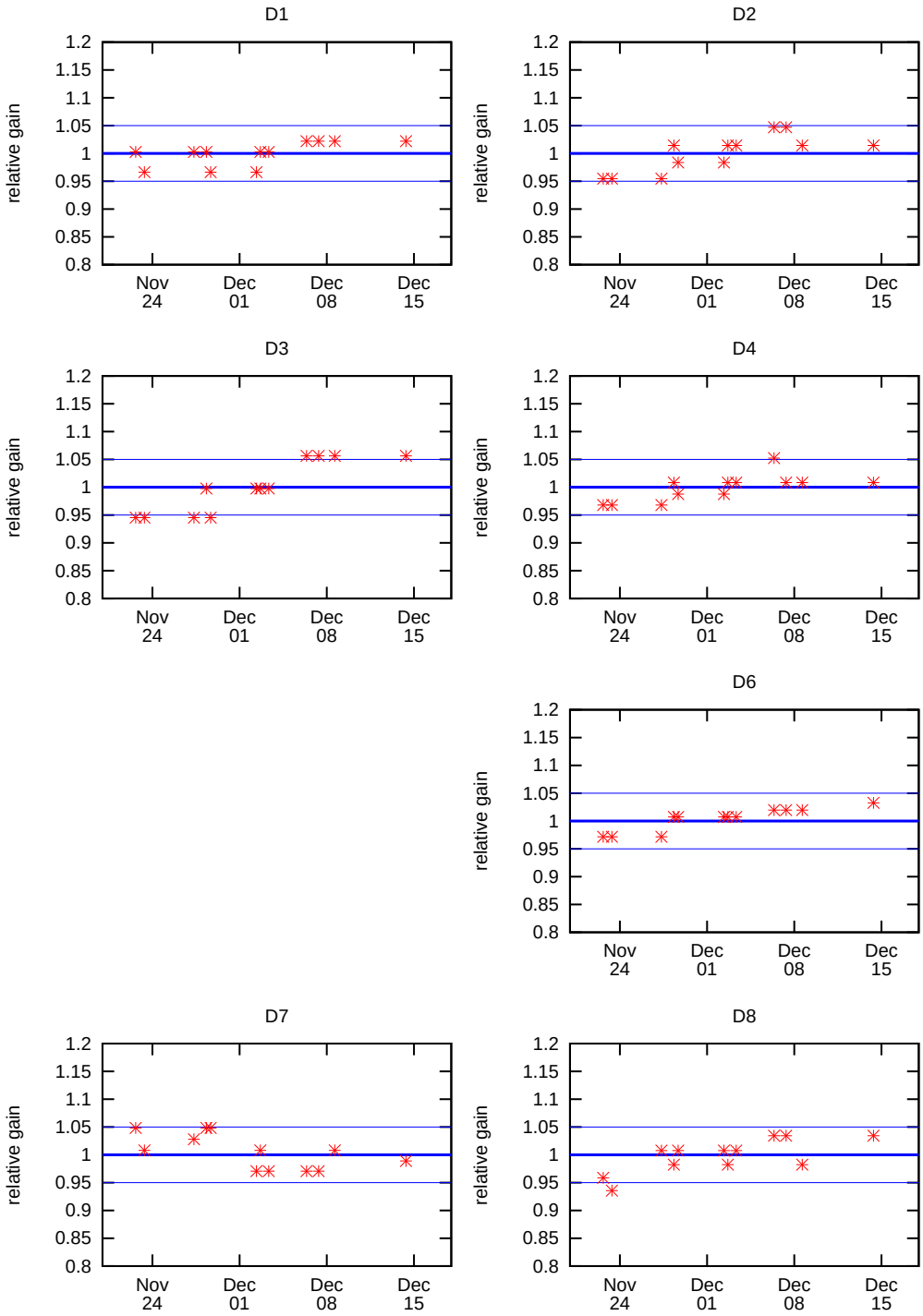

Figure 5.37: Stability of the seven bolometers. We show the gains normalized to the average during the measurement. Lines corresponding to the average and those corresponding to $\pm 5\%$ are also show.

Chapter 6

Analysis and Results

6.1 Trigger and Fitting

6.1.1 Trigger

The data are taken without any online triggers with a sampling rate of 1kHz as described in Section 5.1.4 so we start with the off line trigger. Typical raw data of the bolometers are shown in Fig. 6.1 together with signals averaged over ±10 msec. Simple level trigger is applied to the data averaged over ±10 msec. The baselines are determined by averaging the data for 200 msec before the trigger time and 250 msec of dead time is set after each trigger. Trigger levels are determined so that the trigger rate is less than 1 Hz. Trigger levels used for the analysis are listed in Table 6.1.

Detector	D1	D2	D3	D4	D6	D7	D8
Trigger level[V]	0.006	0.007	0.008	0.012	0.006	0.003	0.005
Trigger level[keV]	32	11	7.3	5.8	5.0	7.9	2.0
Trigger rate [Hz]	0.17	0.27	0.095	1.1	0.0064	0.38	0.25

Table 6.1: Trigger levels and typical count rates for the seven bolometers. Trigger levels normalized in units of keV are also listed.

6.1.2 Fitting

For the triggered events, pulse heights are obtained by fitting the scaled template signals shown in Fig. 5.29 to the raw signals.

We took three free fitting parameters: pulse height, baseline, and event time. Best fit

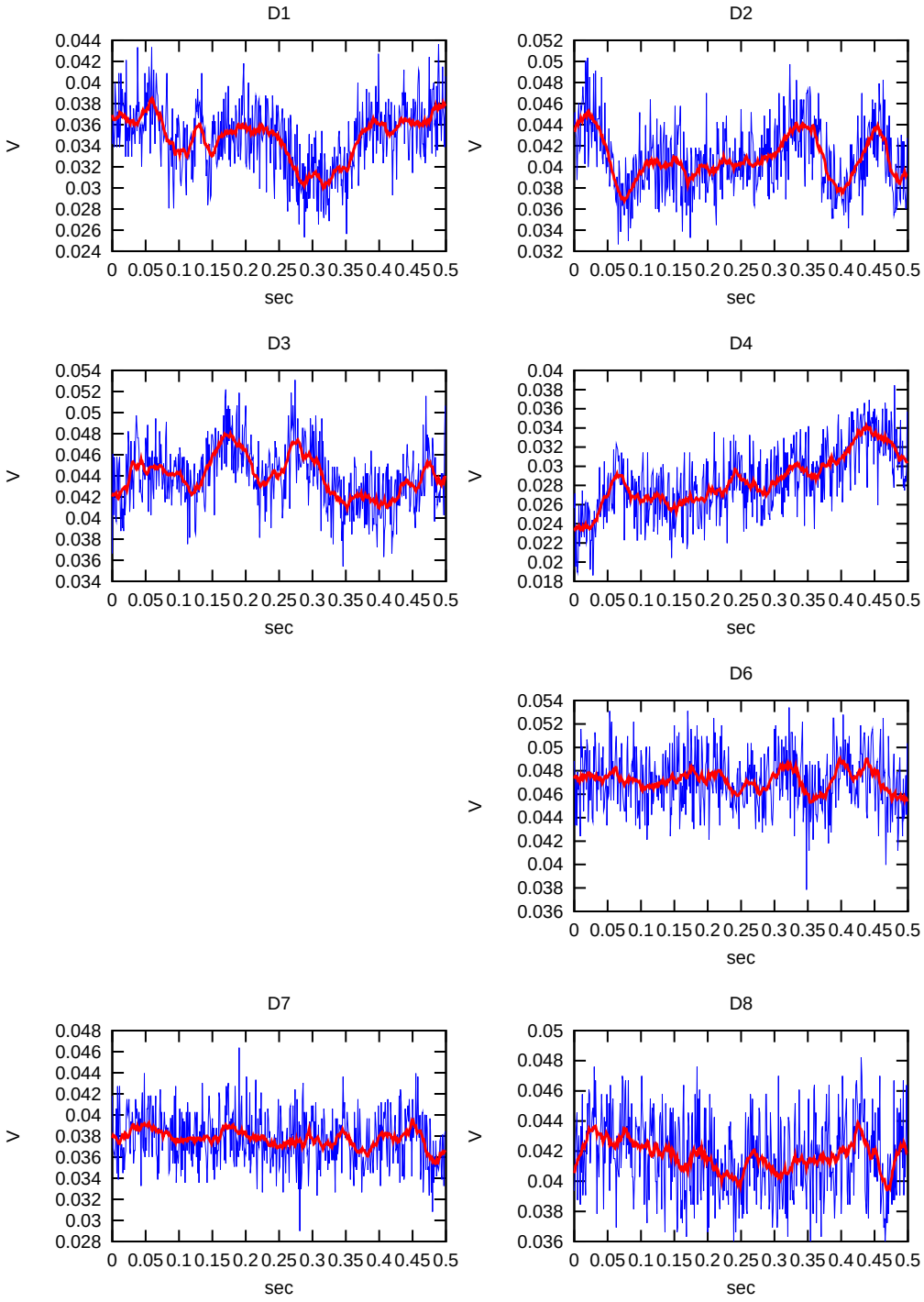

Figure 6.1: Typical raw data of the bolometer signals(blue). Signals averaged over ±10 msec are overdrawn in red.

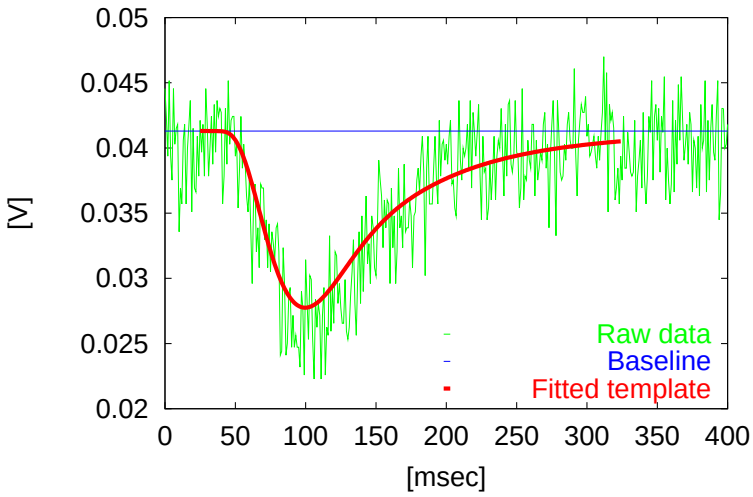

Figure 6.2: Typical low energy(5.5keV) signal of one of the detectors(D8). Scaled template signal and the baseline are also shown.

values are obtained by minimizing the χ^2 defined as

$$\chi^2 = \sum_{i=0}^{TL} \left(\frac{(v_{i+T}^{\mathrm{raw}} - (PH \cdot v_i^{\mathrm{Template}} + BL))}{\Delta v_{i+T}} \right)^2 \tag{6.1}$$

where TL is the length of the template listed in Table 6.2, v^{raw} is the raw data, T is the fitting parameter 'event time', PH is the fitting parameter 'pulse height', v^{Template} is the normalized template, BL is the fitting parameter 'base line'. As the error of each data point is in principle determined by the base line noise, the error Δv_{i+T} is thought to have a constant value. We simply used $\Delta v_{i+T} = cnst = 1$. Thus the χ^2 values have no other meaning than finding the best fit parameters.

	D1	D2	D3	D4	D6	D7	D8
Length[msec]	300	300	300	400	300	300	300

Table 6.2: Template lengths used for the analysis.

An example of the fitting process result is shown in Fig. 6.2.

6.2 Event Selection

After the fitting process, event selections are performed to the whole data. The event selection consists of the three steps listed in Table 6.3.

Step	Selection	Section
1	Noise Elimination	6.2.1
2	Threshold Cut	6.2.2
3	Multi Hit Cut	6.2.3

Table 6.3: Event selections.

6.2.1 Noise Elimination

The first step of the event selection is the noise elimination. Those events that satisfy the following two criteria are selected as real bolometer events.

1. Ratio of the pulse height of the raw data to the fitted pulse height is in a defined acceptance region.

2. Ratio of the integrated pulse area to the fitted pulse height is in a defined acceptance region.

Events that are thought to be occurred in the NTD Ge thermistor('thermistor events') are eliminated by the first selection, while the electronic noise in the low energy region is eliminated by the second. Details on the two steps of the noise elimination are described below.

- Thermistor Event Elimination
  Typical event that is thought to have occurred in the thermistor is shown in Fig.6.3. The time constant is shorter than the template, because the heat capacity of the thermistor is small and the thermal impedance to the dilution refrigerator is small. Therefore the pulse height of the raw signal and the fitted pulse height differ as shown in Fig.6.3. We use the ratio of Raw P.H. to the Fitted P.H. in Fig.6.3 to eliminate the thermistor events.

  The ratio of Raw P.H. to Fitted P.H. are plotted against the energy which is calculated from the latter in Fig. 6.4. Two bands are clearly seen: thermistor events and LiF events. Events with the ratio between 0.8 and 1.1 are selected as real bolometer events in this event selection.

- Electric Noise Elimination
  Fluctuations of the base line often mimic the low energy bolometer signals. Typical

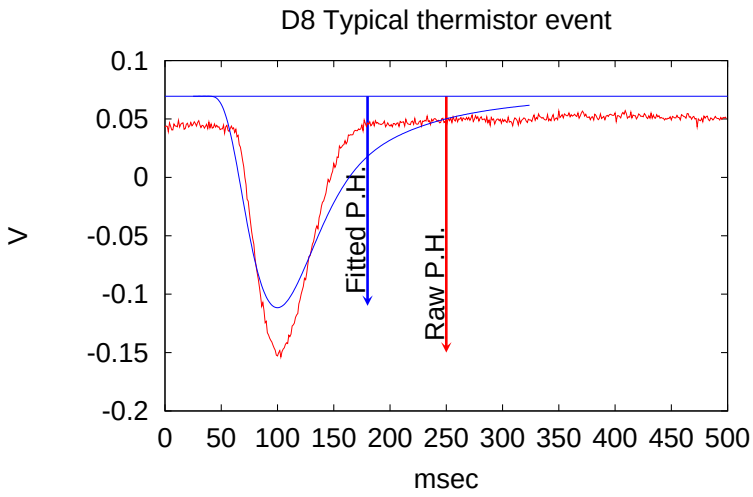

Figure 6.3: Typical thermistor event. Red and blue lines show the raw signal and fitted template, respectively.

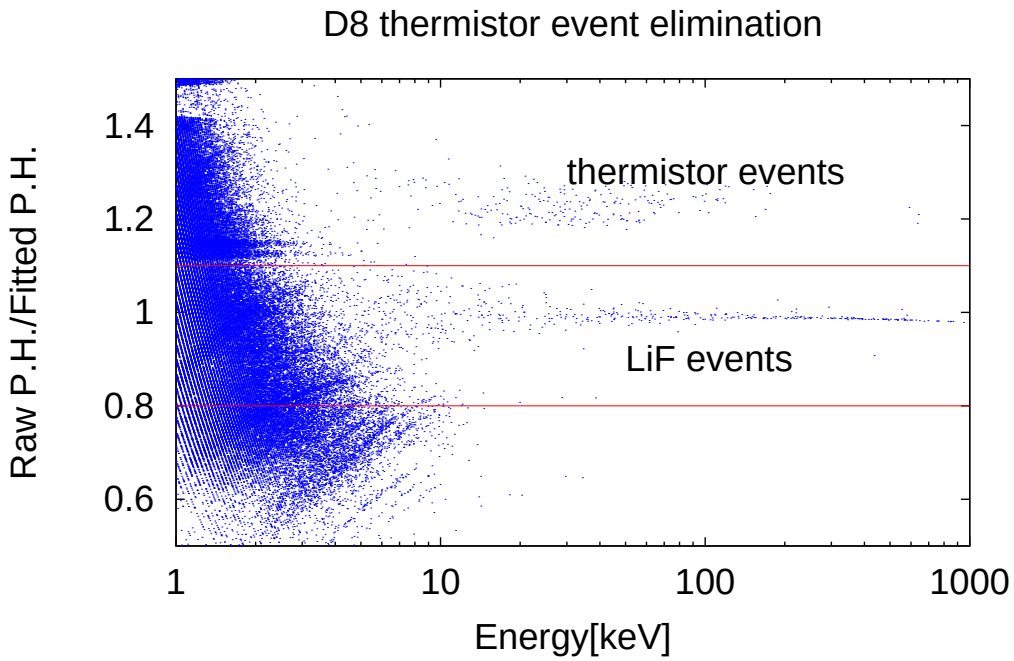

Figure 6.4: Ratio of raw P.H. to fitted P.H. is plotted as a function of the energy. Events in the region between the two line are selected.

electric noise is shown in Fig. 6.5. These events can be separated from the real bolometer signals by the ratio of integrated pulse area to the fitted pulse height. The integrated pulse area is defined as

$$\text{Integrated area} = \frac{\sum_{i=0}^{TL}(v_{i+T}^{\text{raw}} - BL)\Delta t}{A} \tag{6.2}$$

where Δt=1 msec is the sampling rate and A is the constant for the normalization. Other notations are same as Eq. (6.1). The normalization constant A is determined for each bolometer so that the integrated area for the real bolometer event becomes dimensionless value 1 and is listed in Table 6.4.

	D1	D2	D3	D4	D6	D7	D8
A[V·msec]	122	122	105	153	115	140	110

Table 6.4: Normalization constants of the integrated area for the seven bolometers.

In Fig. 6.6, the ratios of integrated pulse area to the fitted pulse height are plotted as a function of the energy. We take the events in the region between 0.9 and 1.1 as real bolometer signals. Some of the low energy real bolometer events are lost together with electric noises by this cut, and the efficiency of this cut is well estimated as discussed in Section 6.2.2.

6.2.2 Trigger and Event Selection Efficiency

Efficiency and stability of the bolometer could be checked by a heat pulse to the bolometer with a heater attached to the crystal or with an IR pulse sent through optical fibers[81, 82]. It is, however, difficult to use this method since the thermal couplings of the crystal and the refrigerator would change and the performance of the bolometer might be affected. We have instead adopted an alternative method: for the stability check, we constantly calibrate the detector with radioactive check sources and efficiency is checked by the following method.

As we record all of the data, we can estimate the trigger and event selection efficiencies by adding a simulated pulse of a known energy to the raw data and analyzing them in the same manner as the real data. Estimated efficiencies of the seven bolometers near the threshold are shown in Fig. 6.7. Efficiency curve is fitted with a function

$$\text{Efficiency(x)} = \text{a} + \text{b}\tanh((\text{x} - \text{c})/\text{d}) \tag{6.3}$$

where x is the energy in keV, a,b,c,d are fitting parameters. We fixed a=b=0.5 and fitted the function with c and d as free parameters. As we only take the events with efficiency greater than 0.5, the fitting was performed to have the best fit in the energy region with efficiencies larger than 0.5. Fitting results are listed in Table 6.5.

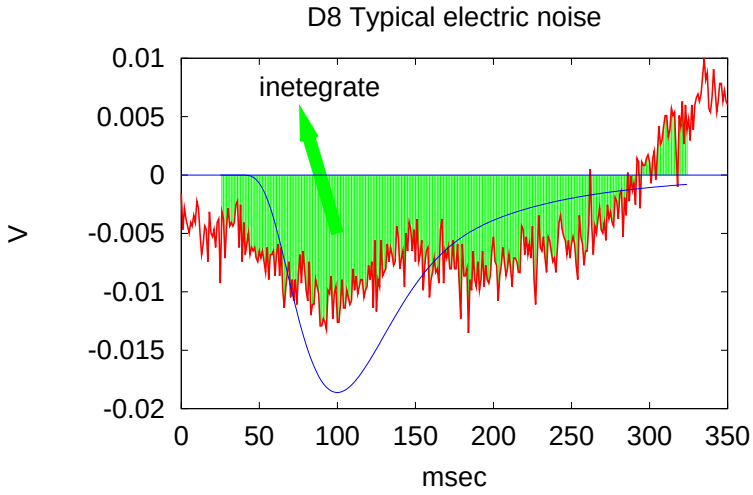

Figure 6.5: Typical electric noise. Red and blue lines show the raw signal and fitted template, respectively. Integrated area is shown in green. This event is eliminated as the ratio is less than 0.9.

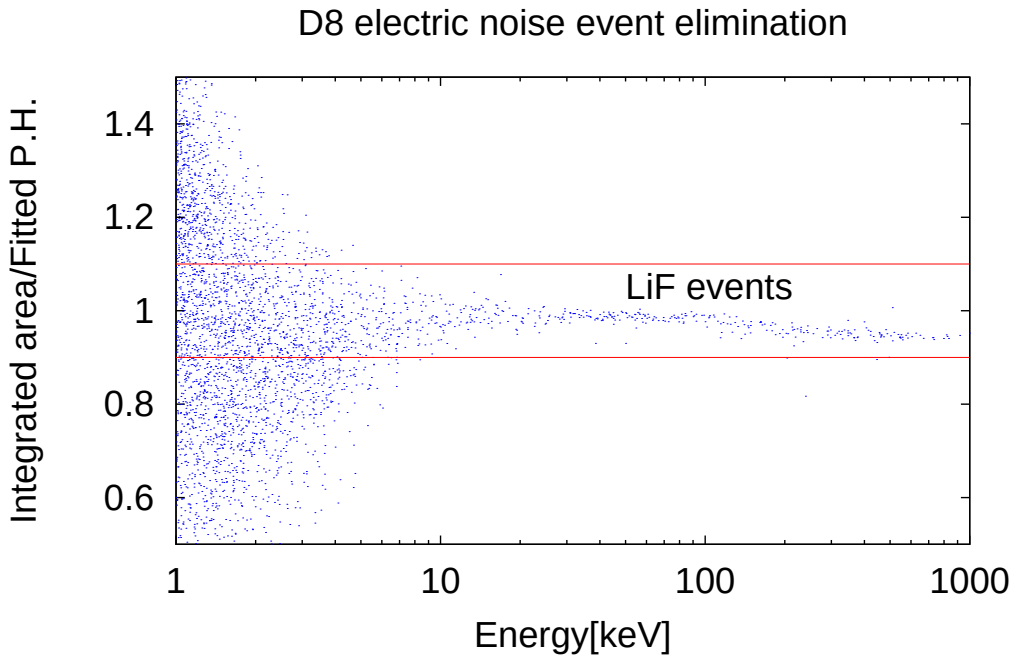

Figure 6.6: The ratio of integrated pulse area to fitted P.H. is plotted against the energy. Events in the region between the two line are selected.

Detector	c	d
D1	78.8	78.7
D2	21.7	24.0
D3	14.4	13.8
D4	30.2	54.0
D6	8.4	8.4
D7	20.4	19.4
D8	4.1	4.5

Table 6.5: Results of the fitting of the efficiency function. c and d are the parameters in Eq. 6.3.

- Threshold Cut
  The threshold is determined to be the energy where the efficiency equals to 0.5. The thresholds of the seven bolometers are listed in Table 6.6. We used the events that exceed the threshold for the further discussions.

Detector	D1	D2	D3	D4	D6	D7	D8
threshold[keV]	78.8	21.7	14.4	30.2	8.4	20.4	4.1

Table 6.6: Thresholds of the seven bolometers. These values are equal to c in Table 6.5. We used the events that exceed the thresholds for the further discussion.

6.2.3 Multi-Hit Cut

We finally cut the multi-hit events for the real bolometer events that exceed the threshold. We cut an event that has a coincident event in any of the other bolometers within ± 10 msec as dark matters never interact with two or more detectors simultaneously. Typical multi-hit event is shown in Fig 6.8. The events left after the multi-hit cut were used for the analysis of the dark matter limit and the discussions as a final sample.

6.3 Results

6.3.1 Final Sample

The event rates after each cut, the real times, and the live times are listed in Table 6.7.

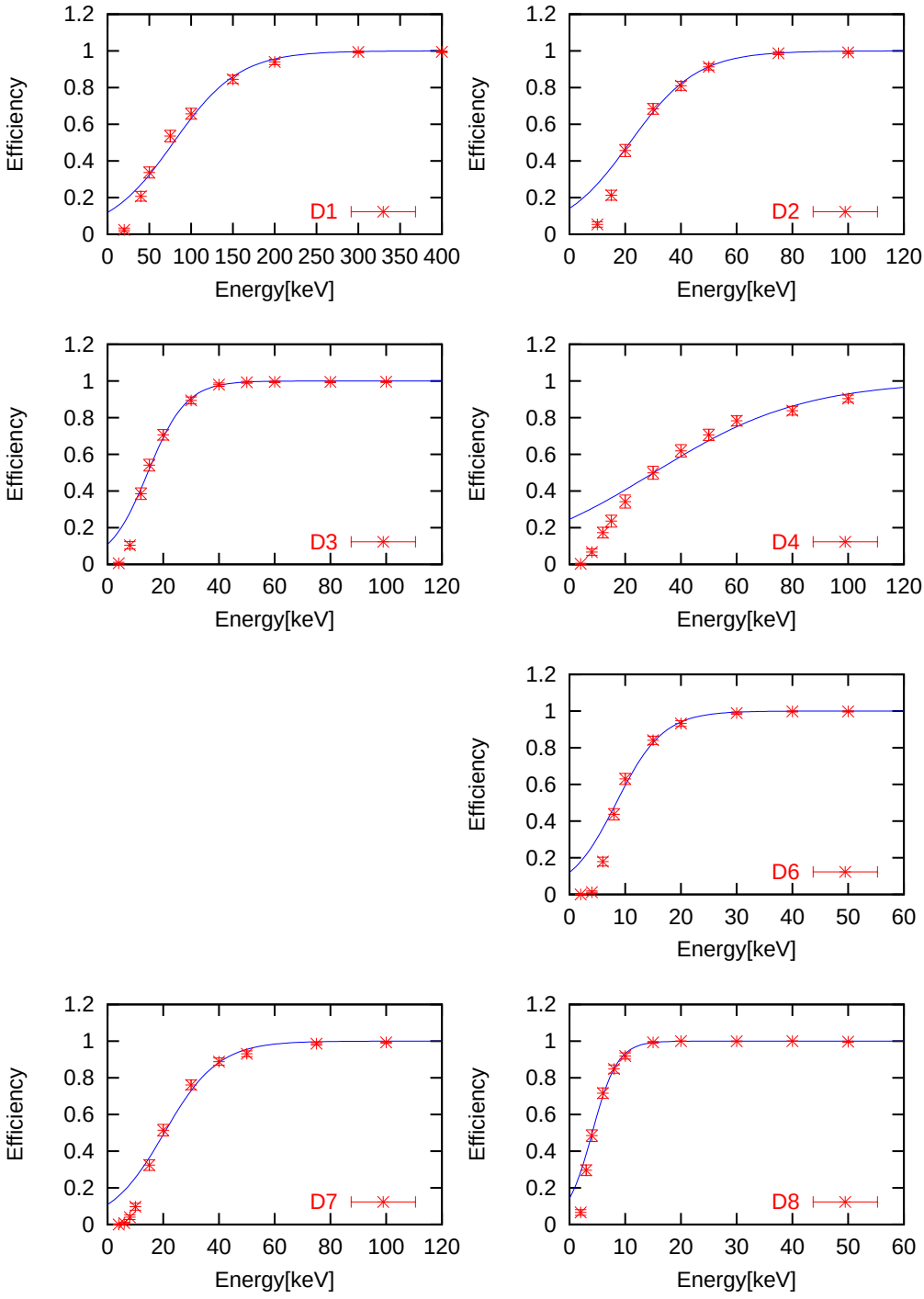

Figure 6.7: Simulated efficiencies near the threshold. Best fit functions for efficiencies larger than 0.5 are drawn in blue. Fitting result of D4 is not very good because the time constants of the signal are different from others.

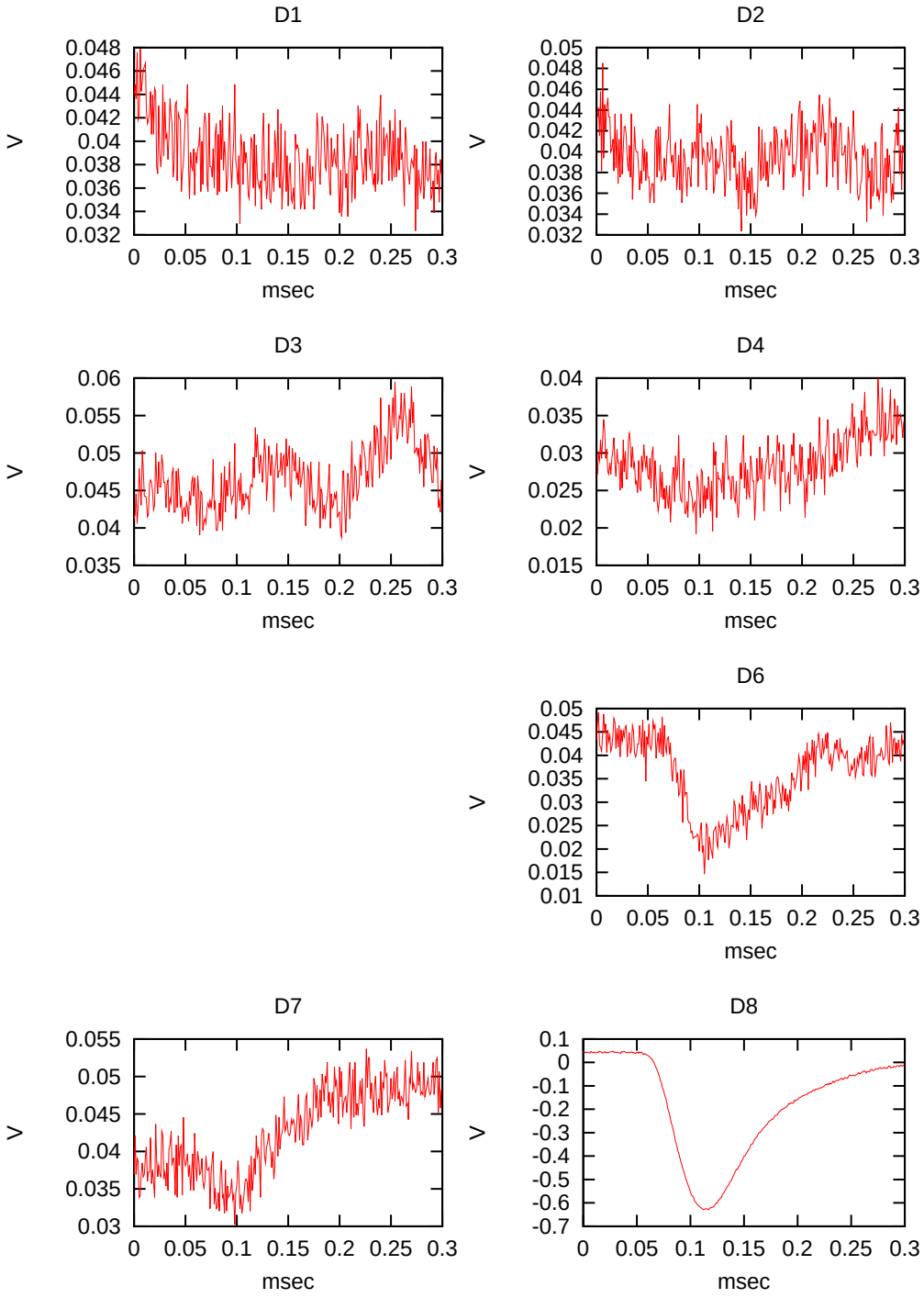

Figure 6.8: Typical multi-hit event. Here, 20keV signal on D6 and 300keV on D8 are seen simultaneously.

Detector		D1	D2	D3	D4	D6	D7	D8
Raw	[Hz]	0.17	0.27	0.095	1.1	0.0064	0.38	0.25
Thermistor Cut	[10^{-2}Hz]	5.5	5.4	1.9	10.1	0.11	0.37	9.32
Electric Noise Cut	[10^{-2}Hz]	3.3	0.80	6.0	8.8	0.11	0.19	5.74
Threshold Cut	[10^{-2}Hz]	0.056	0.46	0.18	0.17	0.10	0.068	1.7
Multi-Hit Cut(Final data set)	[10^{-2}Hz]	0.054	0.45	0.18	0.16	0.094	0.065	1.65
Real Time	[days]	14.8	14.8	14.8	14.8	14.8	14.8	14.8
Live Time	[days]	14.2	13.9	14.5	11.5	14.8	13.6	14.0

Table 6.7: Count rate after each event selection.

6.3.2 Obtained Spectra

We obtained the energy spectra for the seven bolometers from the final data set shown in Table 6.7. We normalized the observed number of events $N_{n,k}$ in a data bin by

$$S_{n,k} = N_{n,k}/t/\Delta E/m/\mathrm{eff}(E_{\mathrm{R}}), \tag{6.4}$$

where n denotes the detector number and k does the energy bin number. $S_{n,k}$ is the normalized count rate in the given energy bin (n,k), t is the live time in days, ΔE is the bin width of the energy bin in keV, m is the detector mass in kg, and $\mathrm{eff}(E_{\mathrm{R}})$ is the efficiency at the lower edge E_{R} energy of the energy bin.

Low energy spectra of the seven bolometers are shown in Fig. 6.9 together with the result of the pilot run at Nokogiriyama underground cell. Energy spectra of D6, D7, and D8 are compared with the the result of the preliminary measurement at Kamioka in Fig. 6.10. It is seen that the backgrounds of D6, D7, and D8 are about one tenth of the result of pilot run at Nokogiriyama underground cell and they are lower than the result of the preliminary run. The steep rises in the spectra of D6 and D8 below 10 keV are due to real bolometer signals, while those of other detectors are caused by the electric noises. D4 has rather high background because of the fluctuation of the baseline.

6.3.3 Neutralino-Nucleus Limits $\sigma_{\chi-\mathrm{N}}$

From the obtained spectra shown in Fig. 6.9 we derived $\sigma_{\chi-\mathrm{N}}$ limits as described in Section 3.1 and Section 3.2 with the astrophysical and nuclear parameters listed in Table 6.8.

We derived the limits by the same manner as presented in Ref.[27]. We conservatively assumed that all the signals are caused by the neutralino and compared the obtained spectra shown in Fig. 6.9 to the spectra expressed as Eq. (3.24) smeared with the resolution σ of the detector listed in Table 5.16 for a given neutralino mass M_χ and nucleus component $N(N$=Li,F). Here we write the left term of Eq. (3.24) as dR/dE_{R} and then the spectrum

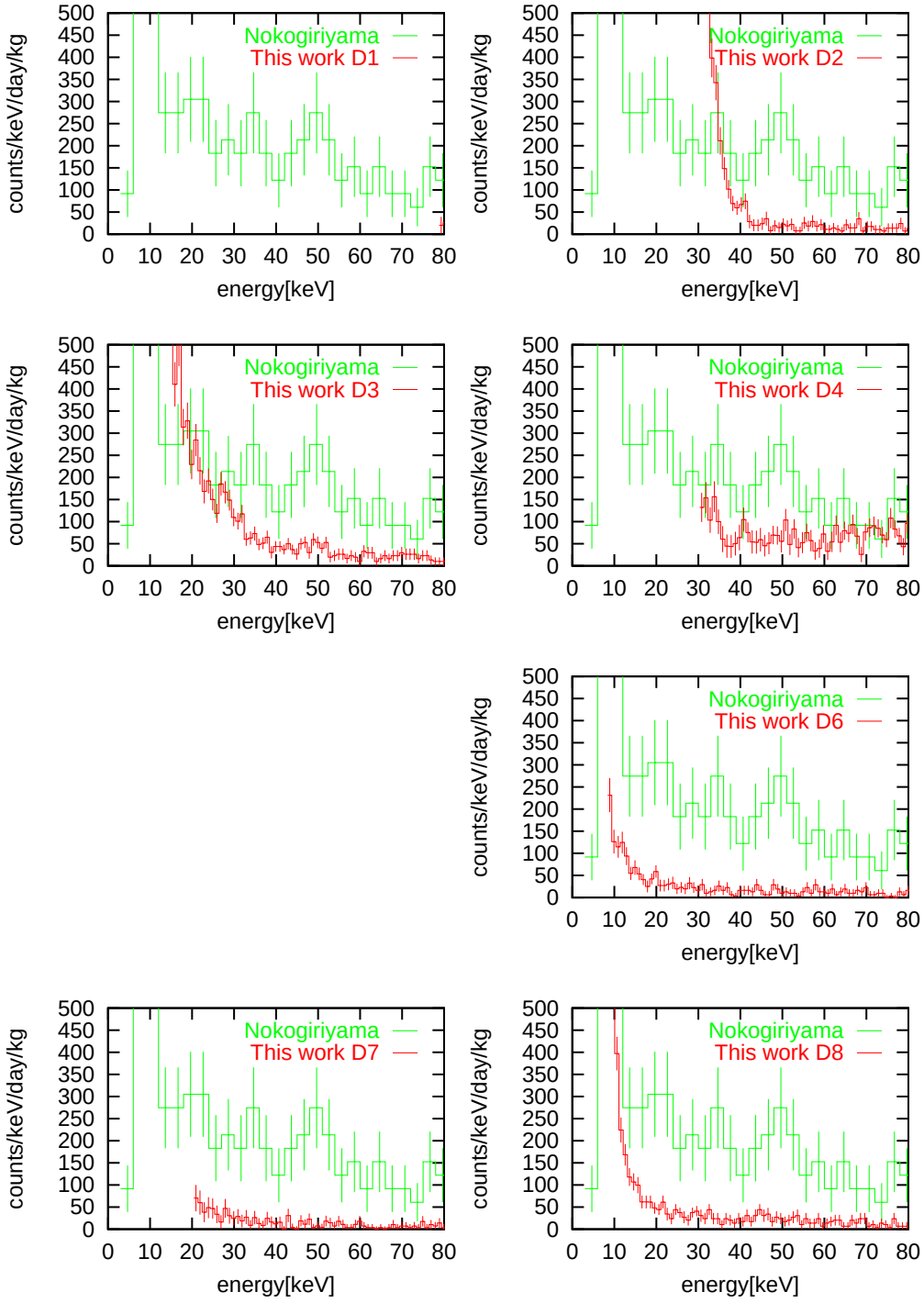

Figure 6.9: Low energy spectra obtained with the seven bolometers. Result of the pilot run is drawn in green(Nokogiriyama) and result of this experiment is drawn in red(this work).

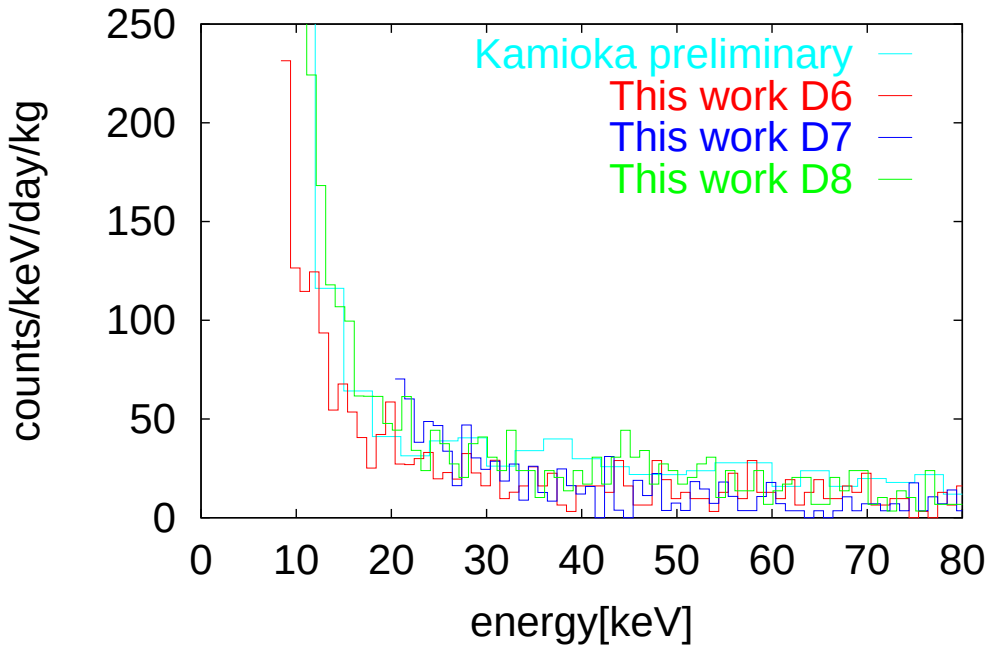

Figure 6.10: Comparison of the low energy spectra between this experiment and the preliminary run at Kamioka. The spectra of D6, D7, and D8 of this experiment and the result of the preliminary run at Kamioka(D8) are shown.

smeared with the resolution σ is written as

$$\frac{dR(\sigma)}{dE_{\rm R}} = \int_0^\infty g(E_{\rm R} - E)\frac{dR}{dE}dE, \tag{6.5}$$

where

$$g(x) = \frac{1}{\sqrt{2\pi}\sigma}\exp(-\frac{x^2}{2\sigma^2}) \tag{6.6}$$

is the Gaussian distribution. The 90(95)% confidence level upper limit count rate of each bin of the spectra, $S_{n,k}$ is obtained by

$$S_{n,k}^{90(95)\%{\rm CL}} = N_{n,k}^{90(95)\%{\rm CL}}/t/\Delta E/m/{\rm eff}(E_{\rm R}) \tag{6.7}$$

where $S_{n,k}^{90(95)\%{\rm CL}}$ is the 90(95)% confidence level upper limit count rate, $N_{n,k}^{90(95)\%{\rm CL}}$ is the 90(95)% confidence level upper limit of the observed events. $N_{n,k}^{90(95)\%{\rm CL}}$ is defined by the observed events $N_{n,k}$ as

$$N_{n,k}^{90\%{\rm CL}} = N_{n,k} + 1.28 \cdot \sqrt{N_{n,k}} \tag{6.8}$$

$$N_{n,k}^{95\%{\rm CL}} = N_{n,k} + 1.64 \cdot \sqrt{N_{n,k}} \tag{6.9}$$

for $N_{n,k} > 10$. For $N_{n,k} \leq 10$, we use the Poisson upper limits listed in Table 6.9[83]. Then we use

$$S_{n,k}^{90(95)\%CL}\Delta E = \int_{\Delta E}\frac{dR(\sigma)}{E_{\rm R}}f_N F^2(E_{\rm R})dE_{\rm R} \tag{6.10}$$

and Eq. (3.10) to derive the upper limit of the cross section of the neutralino-nucleus interactions with zero-momentum transfer, $\sigma_{0(n,k)}$, where f_N is the mass fraction of the nucleus. The lowest value among the obtained limits among all n, k for a given neutralino mass M_χ and nucleus N is adopted as the combined limit $\sigma_{\chi-{\rm N}}$.

Dark matter density $\rho_{\rm D}$	$0.3{\rm GeVc}^{-2}{\rm cm}^{-3}$
Velocity distribution	Maxwellian
Most probable velocity of the Maxwellian v_0	$230{\rm kms}^{-1}$
Escape velocity $v_{\rm esc}$	$475{\rm kms}^{-1}$
Earth velocity $v_{\rm E}$	$244{\rm kms}^{-1}$
shell model	odd group model

Table 6.8: Astrophysical and nuclear parameters used to derive the limit.

N	90%	95%
0	2.30	3.00
1	3.89	4.74
2	5.32	6.30
3	6.68	7.75
4	7.99	9.15
5	9.27	10.51
6	10.53	11.84
7	11.77	13.15
8	13.00	14.44
9	14.21	15.71
10	15.41	16.96

Table 6.9: Poisson upper limits for observed event N[83].

6.3.4 $\sigma_{\chi-\mathrm{p}}$ Limits with Conventional Method

From the obtained neutralino-nucleus cross sections limit $\sigma_{\chi-\mathrm{N}}$, we derived neutralino-nucleon cross sections with the conventional method described in Section 3.3.3 and 3.3.4 with Eq.(3.40), or

$$\sigma_{\chi-\mathrm{p}} = \sigma_{\chi-\mathrm{N}} \frac{\mu^2_{\chi-\mathrm{p}}}{\mu^2_{\chi-\mathrm{N}}} \frac{C_{\mathrm{p}}}{C_{\mathrm{N}}} \tag{6.11}$$

For the ratio of the enhancement factors for the spin-independent cross section($\sigma^{\mathrm{SI}}_{\chi-\mathrm{p}}$) limits, we use Eq. (3.47), or

$$\frac{C^{\mathrm{SI}}_{\mathrm{N}}}{C^{\mathrm{SI}}_{\mathrm{p}}} = A^2. \tag{6.12}$$

For the spin-dependent cross section($\sigma^{\mathrm{SD}}_{\chi-\mathrm{p}}$) limits, we use Eq. (3.51) and the $\lambda^2 J(J+1)$ values listed in Table 3.1. We use the values of odd group model and they are listed in Table 6.10

Isotope	$\lambda^2 J(J+1)$
p	0.75
^{7}Li	0.411
^{19}F	0.647

Table 6.10: $\lambda^2 J(J+1)$ values used to derive the $\sigma^{\mathrm{SD}}_{\chi-\mathrm{p}}$. Values are same as listed in Table 3.1.

We derived $\sigma_{\chi-\mathrm{p}}$ limits from Li and F independently, then combined the results by Eq.

(3.61) or

$$\frac{1}{\sigma_{\lim\chi-\mathrm{p(LiF)}}} = \frac{1}{\sigma_{\lim\chi-\mathrm{p(Li)}}} + \frac{1}{\sigma_{\lim\chi-\mathrm{p(F)}}} \tag{6.13}$$

The obtained $\sigma^{\mathrm{SI}}_{\chi-\mathrm{p}}$ and $\sigma^{\mathrm{SD}}_{\chi-\mathrm{p}}$ limits are shown in Fig. 6.11 and Fig. 6.12, respectively. As we have performed a more conservative analysis than the pilot run by discarding the low energy bins with efficiency less than 0.5, we could not improve the limits for the neutralino lighter than 10GeVc^{-2} . The limits to neutralinos heavier than 30GeVc^{-2} have been improved by about one order of magnitude. The best limits are $\sigma^{\mathrm{SI}}_{\chi-\mathrm{p}}$=0.055 pb and $\sigma^{\mathrm{SD}}_{\chi-\mathrm{p}}$=21 pb for $M_\chi = 28\mathrm{GeVc}^{-2}$

6.3.5 σ^{SD} Limits with New Method

We analyzed the data with the new method described in Section 3.3.6 for the model independent interpretation of the results[42].

Limits to $\sigma^{\mathrm{SD}}_{\chi-\mathrm{p}}$ and $\sigma^{\mathrm{SD}}_{\chi-\mathrm{n}}$

From the $\sigma^{\mathrm{SD}}_{\chi-\mathrm{N}}$ limits described in Section 6.3.3, we derived spin-dependent neutralino-nucleon cross section $\sigma^{\mathrm{SD}}_{\chi-\mathrm{p}}$ and $\sigma^{\mathrm{SD}}_{\chi-\mathrm{n}}$limits with new method. We used Eq. (3.66):

$$\begin{aligned}
\sigma^{\mathrm{SD}}_{\chi-\mathrm{p}} &= \sigma^{\mathrm{SD}}_{\chi-\mathrm{N}} \frac{\mu^2_{\chi-\mathrm{p}}}{\mu^2_{\mathrm{N}}} \left(\frac{C^{\mathrm{SD}}_{\mathrm{p(N)}}}{C^{\mathrm{SD}}_{\mathrm{p}}} \right)^{-1} \\
\sigma^{\mathrm{SD}}_{\chi-\mathrm{n}} &= \sigma^{\mathrm{SD}}_{\chi-\mathrm{N}} \frac{\mu^2_{\chi-\mathrm{n}}}{\mu^2_{\mathrm{N}}} \left(\frac{C^{\mathrm{SD}}_{\mathrm{n(N)}}}{C^{\mathrm{SD}}_{\mathrm{n}}} \right)^{-1}
\end{aligned} \tag{6.14}$$

and the values listed in Table 3.2. $C^{\mathrm{SD}}_{\mathrm{p(N)}}/C^{\mathrm{SD}}_{\mathrm{p}}$ and $C^{\mathrm{SD}}_{\mathrm{n(N)}}/C^{\mathrm{SD}}_{\mathrm{n}}$ values used to derive the $\sigma^{\mathrm{SD}}_{\chi-\mathrm{p}}$ and $\sigma^{\mathrm{SD}}_{\chi-\mathrm{n}}$ limits are listed in Table 6.11. Derived $\sigma^{\mathrm{SD}}_{\chi-\mathrm{p}}$ and $\sigma^{\mathrm{SD}}_{\chi-\mathrm{n}}$ limits are shown in Fig. 6.13.

$\sigma^{\mathrm{SD}}_{\chi-\mathrm{p}}$ and $\sigma^{\mathrm{SD}}_{\chi-\mathrm{n}}$ limits for some M_χ are listed in Table 6.12 for further discussions.

Limits in the $\sigma^{\mathrm{SD}}_{\chi-\mathrm{p}} - \sigma^{\mathrm{SD}}_{\chi-\mathrm{n}}$ plane

With the limits listed in Table 6.12, we derived the limits in the $\sigma^{\mathrm{SD}}_{\chi-\mathrm{p}} - \sigma^{\mathrm{SD}}_{\chi-\mathrm{n}}$ plane for M_χ =15, 30, 50, 60, 80, and 100GeVc^{-2}. We used Eq. (3.72):

$$\sum_{\mathrm{N=Li,F}} \left(\sqrt{\frac{\sigma^{\mathrm{SD}}_{\chi-\mathrm{p}}}{\sigma^{\mathrm{SD}}_{\lim\chi-\mathrm{p(N)}}}} \pm \sqrt{\frac{\sigma^{\mathrm{SD}}_{\chi-\mathrm{n}}}{\sigma^{\mathrm{SD}}_{\lim\chi-\mathrm{n(N)}}}} \right)^2 = 1. \tag{6.15}$$

The limits in the $\sigma^{\mathrm{SD}}_{\chi-\mathrm{p}} - \sigma^{\mathrm{SD}}_{\chi-\mathrm{n}}$ plane are shown in Fig. 6.14 and Fig. 6.15. $\sigma^{\mathrm{SD}}_{\chi-\mathrm{n}}$ are plotted as a function of $\sigma^{\mathrm{SD}}_{\chi-\mathrm{p}}$ for M_χ=15, 30, 50, 60, 80 and 100GeVc^{-2} and both signs of $a_{\mathrm{p}}/a_{\mathrm{n}}$. Inside(left down part) of the limit lines are allowed regions.

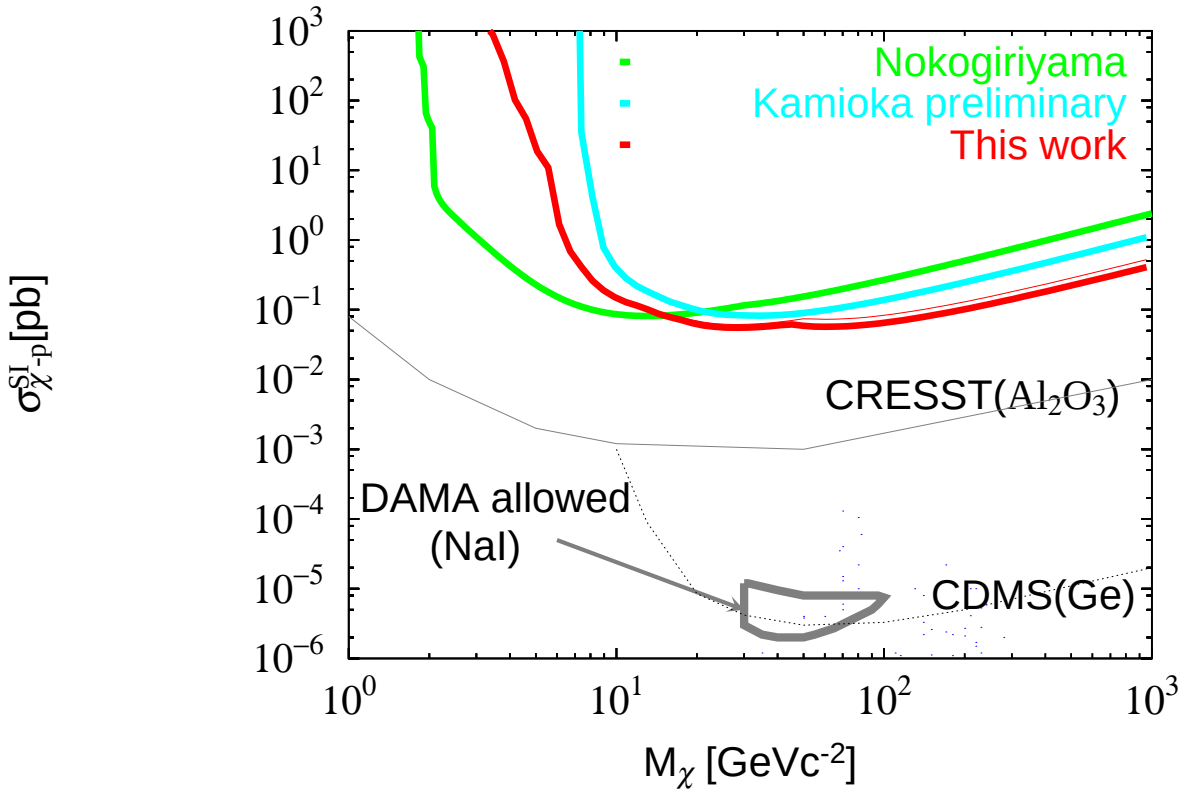

Figure 6.11: $\sigma^{\mathrm{SI}}_{\chi-\mathrm{p}}$ limits as a function of M_χ. The regions above the curves are excluded at 90% C.L. The result from this experiment is shown in thick red(This work) line together with the 95% limits in thin red line. The results of the pilot run and the preliminary measurement at Kamioka Observatory are shown in green (Nokogiriyama)[29] and in sky blue(Kamioka preliminary), respectively. DAMA's allowed region is shown in thick gray line[22]. Limits from other experiments are also shown[23, 30]. MSSM predictions are shown in blue plots[84].

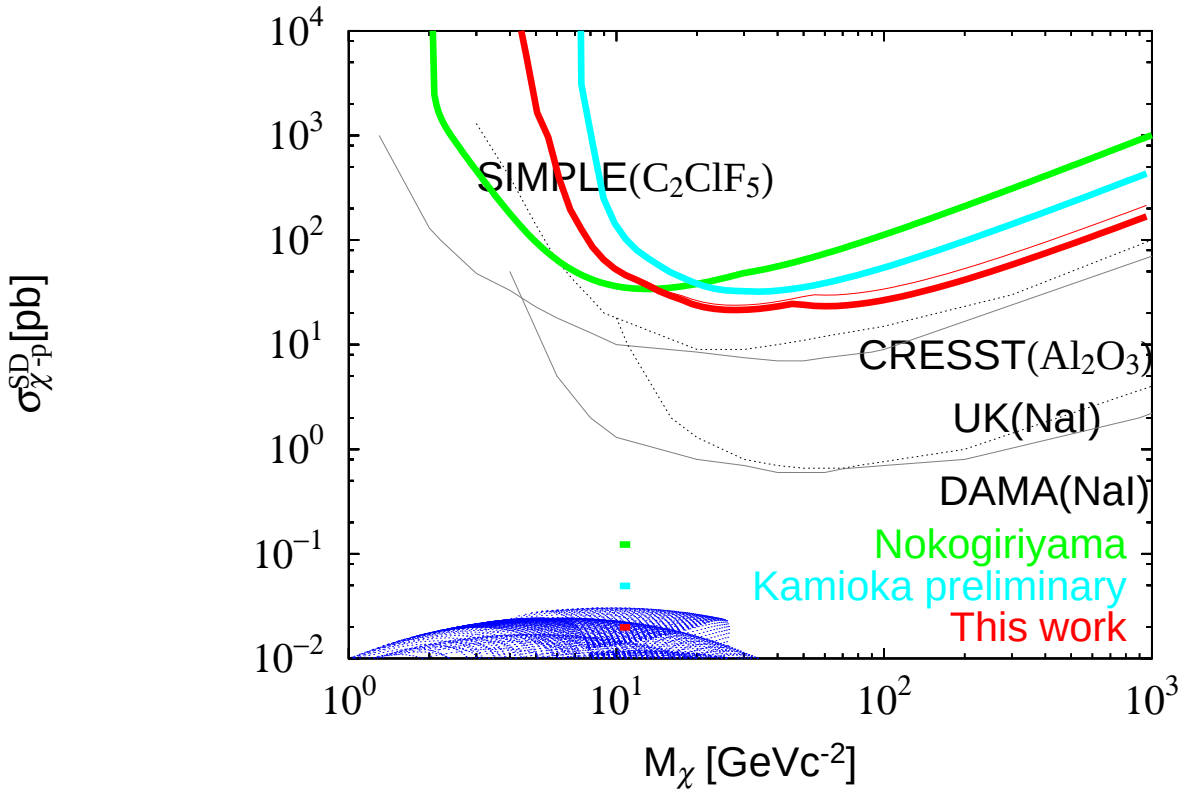

Figure 6.12: $\sigma^{\mathrm{SD}}_{\chi-\mathrm{p}}$ limits as a function of M_χ. The regions above the curves are excluded at 90% C.L. The result from this experiment is shown in thick red(This work) line together with 95% limits in thin red line. The results of the pilot run and the preliminary measurement at Kamioka Observatory are shown in green (Nokogiriyama)[29] and in sky blue(Kamioka preliminary), respectively. Results from other experiments are shown for comparison[28, 30, 53, 64]. MSSM predictions are shown in blue plots.

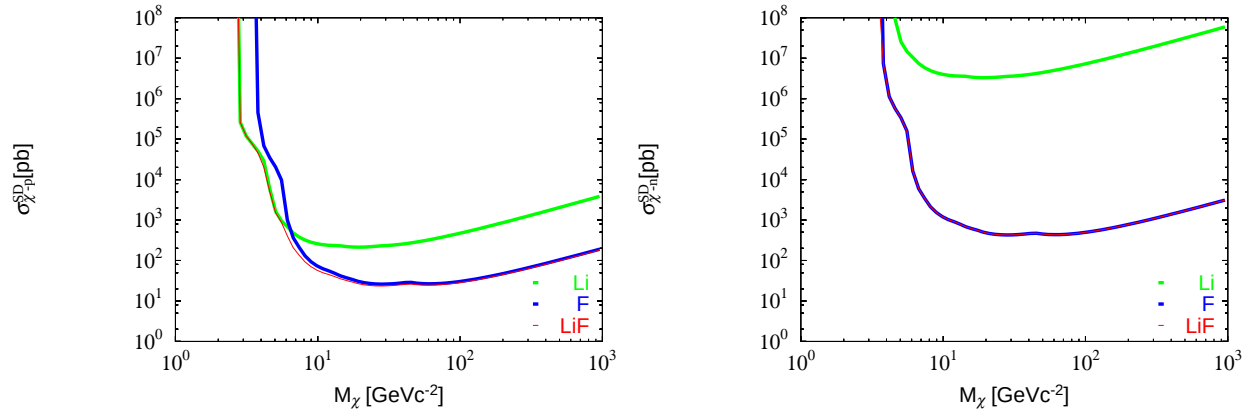

Figure 6.13: $\sigma^{\mathrm{SD}}_{\chi-\mathrm{p}}$(left) and $\sigma^{\mathrm{SD}}_{\chi-\mathrm{n}}$(right) limits as a function of M_χ. The regions above the curves are excluded at 90% C.L. Limits from Li and F are shown in green and blue thick line, respectively. The combined limits are also shown in red thin line.

For $M_\chi = 15\mathrm{GeVc}^{-2}$ and $M_\chi = 100\mathrm{GeVc}^{-2}$, the limits from the DAMA experiments[53] are shown. For M_χ = 30, 50, 60, and 80 GeVc^{-2}, the lower and upper limits by DAMA's annual modulation signal, expressed as case (c) in Fig. 2.7[31], are shown. Values used to calculate DAMA's results are shown in Table 6.13. In the Ref.[31], only $\sigma^{\mathrm{SD}}_{\chi-\mathrm{p(NaI)}}$ and $\sigma^{\mathrm{SD}}_{\chi-\mathrm{n(NaI)}}$ are shown, so we calculated the $\sigma^{\mathrm{SD}}_{\chi-\mathrm{p(Na)}}$, $\sigma^{\mathrm{SD}}_{\chi-\mathrm{n(Na)}}$, $\sigma^{\mathrm{SD}}_{\chi-\mathrm{p(I)}}$, and $\sigma^{\mathrm{SD}}_{\chi-\mathrm{n(I)}}$ values with the sensitivities of Na and I at the threshold considering the detector responses described in Ref.[53]. As for $15\mathrm{GeVc}^{-2}$ and $100\mathrm{GeVc}^{-2}$ data, only $\sigma^{\mathrm{SD}}_{\chi-\mathrm{p}}$ limits are shown in Ref.[53], therefore we also calculated $\sigma^{\mathrm{SD}}_{\chi-\mathrm{n}}$ limits from the $\sigma^{\mathrm{SD}}_{\chi-\mathrm{p}}$ limits.

As the sign of $\langle S_\mathrm{p}\rangle/\langle S_\mathrm{n}\rangle$ for ^{19}F differs from those for ^{23}Na and ^{127}I as shown in Table 3.2, results from this work give stringent limits for the $a_\mathrm{p}/a_\mathrm{n} < 0$ neutralino. We excluded a part of the parameter space allowed by the DAMA's annual modulation results for the neutralinos with mass heavier than $50\mathrm{GeVc}^{-2}$. We also excluded a part of the parameter space which is not excluded by the DAMA's upper limits for the neutralinos with mass lighter than $15\mathrm{GeVc}^{-2}$ and heavier than $100\mathrm{GeVc}^{-2}$

Limits in the a_p-a_n(neutralino-nucleon couplings) plane.

With the values listed in Table 6.12, we derived the limits in the $a_\mathrm{p} - a_\mathrm{n}$ plane for $M_\chi = 15, 30, 50, 60, 80, 100\mathrm{GeVc}^{-2}$. We used Eq. (3.73):

$$\sum_{\mathrm{N_i=Li,F}} \left(\frac{a_\mathrm{p}}{\sqrt{\sigma^{\mathrm{SD}}_{\mathrm{lim}\chi-\mathrm{p(Ni)}}}} \pm \frac{a_\mathrm{n}}{\sqrt{\sigma^{\mathrm{SD}}_{\mathrm{lim}\chi-\mathrm{n(Ni)}}}} \right)^2 = \frac{\pi\hbar^4}{24 G_\mathrm{F}^2 \mu_\mathrm{p}^2} \tag{6.16}$$

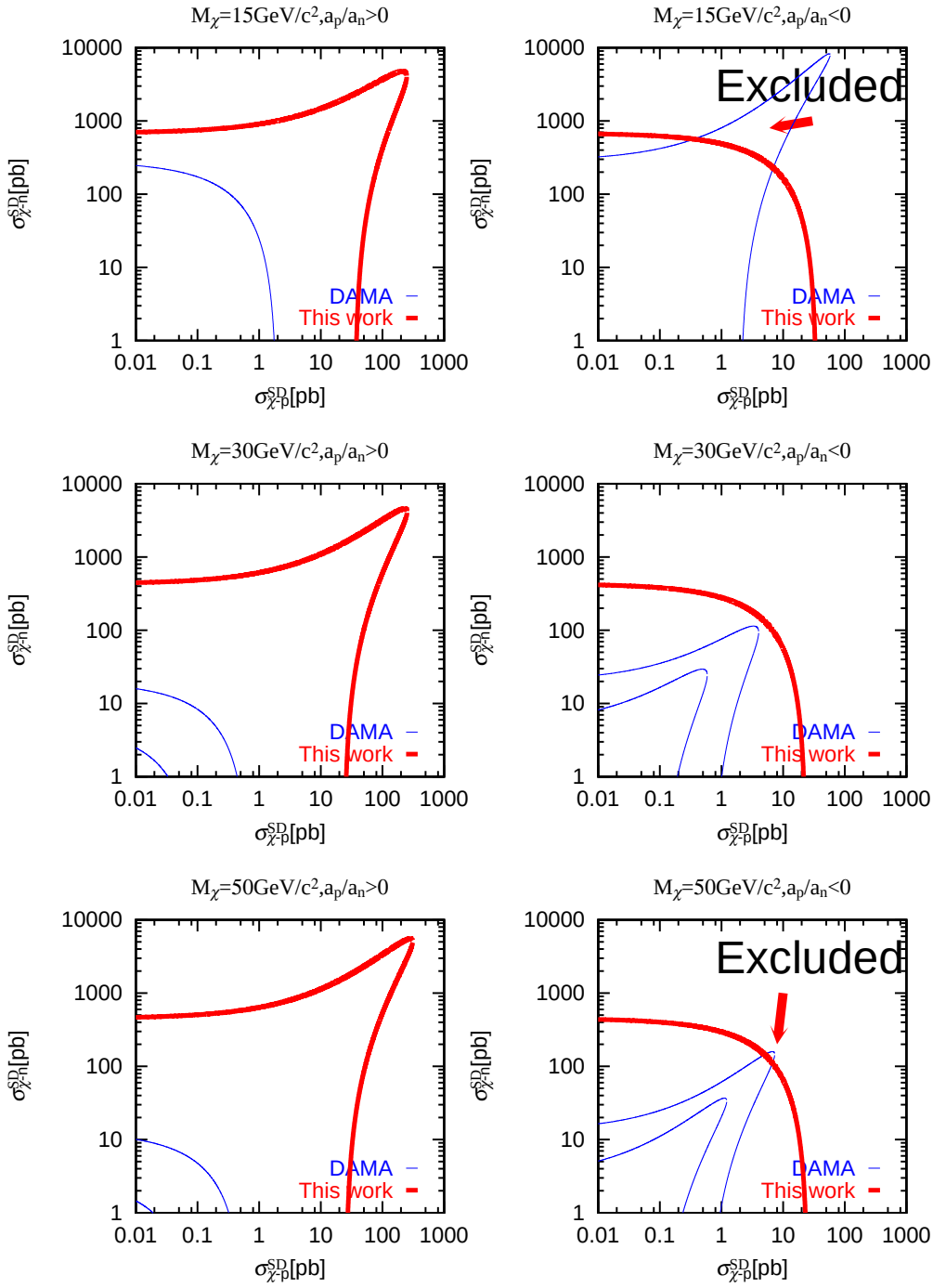

Figure 6.14: Limits in the $\sigma^{\mathrm{SD}}_{\chi-\mathrm{p}}-\sigma^{\mathrm{SD}}_{\chi-\mathrm{n}}$ plane for various M_χ and both signs of $a_\mathrm{p}/a_\mathrm{n}$. Inside(left and down part in the plot) of the red and blue lines are allowed region by this work and DAMA experiment, respectively. For $M_\chi = 30\mathrm{GeVc}^{-2}$ and $M_\chi = 50\mathrm{GeVc}^{-2}$, the lower limits by DAMA's annual modulation signal, shown as case (c) in Fig. 2.7[31], are also shown.

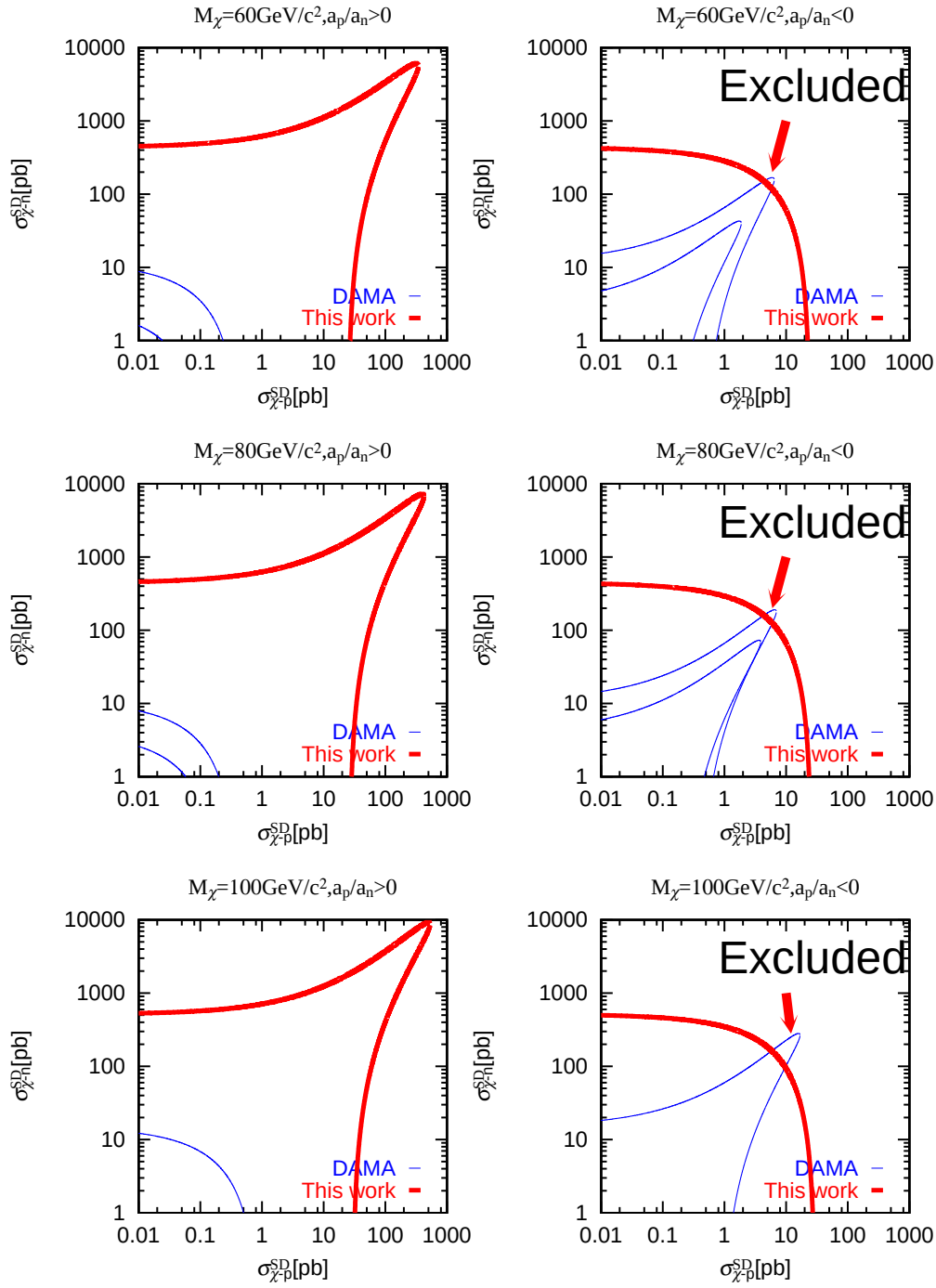

Figure 6.15: Limits in the $\sigma^{\mathrm{SD}}_{\chi-\mathrm{p}}-\sigma^{\mathrm{SD}}_{\chi-\mathrm{n}}$ plane for various M_χ and both signs of $a_\mathrm{p}/a_\mathrm{n}$. Inside(left and down part in the plot) of the red and blue lines are allowed region by this work and DAMA experiment, respectively. For $M_\chi = 60\mathrm{GeVc}^{-2}$ and $M_\chi = 80\mathrm{GeVc}^{-2}$, the lower limits by DAMA's annual modulation signal, shown as case (c) in Fig. 2.7[31], are also shown.

The limits in the $a_p - a_n$ plane are shown in Fig. 6.16. Inside of the red line is the allowed region by this work. For $M_\chi = 15\text{GeVc}^{-2}$ and $M_\chi = 100\text{GeVc}^{-2}$, upper limits from the DAMA experiments[53] are shown in blue. For M_χ = 30, 50 60, and 80 GeVc^{-2}, the lower and upper limits by DAMA's annual modulation signal, shown as case (c) in Fig. 2.7[31], are shown in blue. The regions between the two blue lines are allowed by annual modulation signal.

We excluded a part of the parameter space allowed by the DAMA's annual modulation results for the neutralinos with mass heavier than 50GeVc^{-2}. We also excluded a part of the parameter space which is not excluded by the DAMA's upper limits for the neutralinos with mass lighter than 15GeVc^{-2} and heavier than 100GeVc^{-2}. We have achieved these new constraints because the sign of $\langle S_p \rangle / \langle S_n \rangle$ of ^{19}F is different from those of ^{23}Na and ^{127}I as shown in Table 3.2. This is the merit of the LiF bolometer which is not achieved by other dark matter search detectors with materials such as germanium, since the $\langle S_p \rangle / \langle S_n \rangle$ signs of ^{73}Ge is same as ^{23}Na and ^{127}I.

We have another important result from this experiment. The experiments with NaI detectors cannot set finite allowed region in the $a_p - a_n$ plane for the low mass neutralino since iodine loses sensitivity to the neutralinos lighter than 15 GeVc^{-2} and single nuclide is not sufficient to set a finite allowed region in the $a_p - a_n$ plane as shown in Fig. 3.5. The experiments with Ge detector or Al_2O_3 cannot set a finite allowed region by the same reason[1]. Therefore, this is the only experiment which set the finite allowed region in the $a_p - a_n$ plane for the neutralinos lighter than 15GeVc^{-2}.

[1] Al_2O_3 is effectively a detector with one element because ^{16}O does not have effective spin.

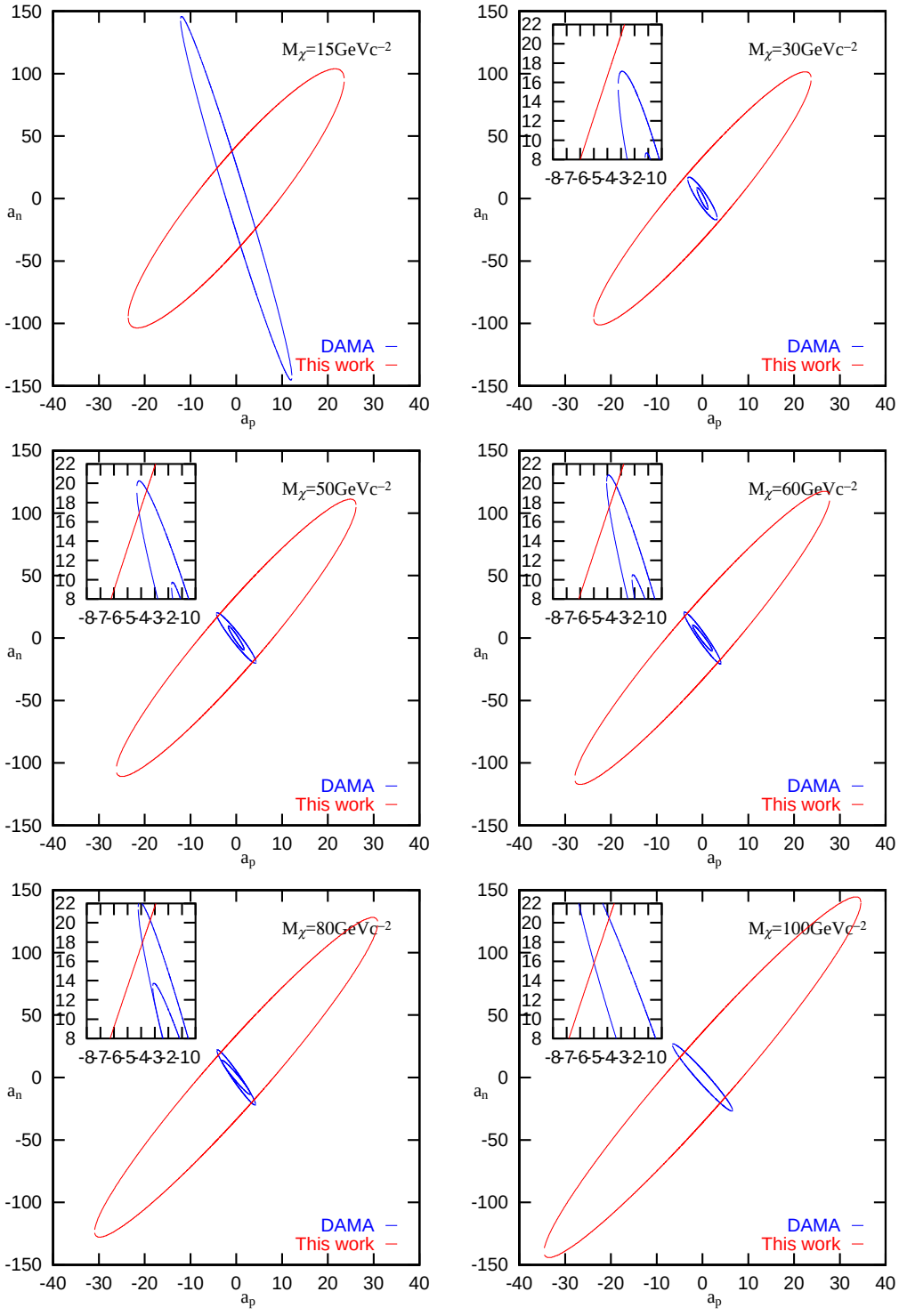

Figure 6.16: Limits in the $a_{\rm p} - a_{\rm n}$ plane for various M_χ. Inside of the red and blue lines are allowed region by this work and DAMA experiment, respectively. For M_χ = 30, 50, 60, and 80 GeVc^{-2}, the lower limits by DAMA's annual modulation signal, shown as case (c) in Fig. 2.7[31], are also shown.

Isotope	$C^{SD}_{p(N)}/C^{SD}_{p}$	$C^{SD}_{n(N)}/C^{SD}_{n}$
^{7}Li	5.49×10^{-1}	3.56×10^{-5}
^{19}F	7.78×10^{-1}	4.75×10^{-2}

Table 6.11: $C^{SD}_{p(N)}/C^{SD}_{p}$ and $C^{SD}_{n(N)}/C^{SD}_{n}$ values used to derive the $\sigma^{SD}_{\chi-p}$ and $\sigma^{SD}_{\chi-n}$ limits. The values are same as those shown in Table 3.2.

M_χ[GeVc^{-2}]	$\sigma^{SD}_{\chi-p(Li)}$	$\sigma^{SD}_{\chi-n(Li)}$	$\sigma^{SD}_{\chi-p(F)}$	$\sigma^{SD}_{\chi-n(F)}$
15	230	3.6×10^{6}	42	680
30	240	3.6×10^{6}	26	430
50	290	4.4×10^{6}	28	450
60	320	5.0×10^{6}	27	440
80	400	6.1×10^{6}	28	450
100	500	7.7×10^{6}	31	510

Table 6.12: $\sigma^{SD}_{\chi-p}$ and $\sigma^{SD}_{\chi-n}$ limits for some M_χ from this work. All of the cross section data are shown in units of pb.

M_χ[GeVc^{-2}]	$\sigma^{SD}_{\chi-p(NaI)}$	$\sigma^{SD}_{\chi-p(Na)}$	$\sigma^{SD}_{\chi-p(I)}$	$\sigma^{SD}_{\chi-n(NaI)}$	$\sigma^{SD}_{\chi-n(Na)}$	$\sigma^{SD}_{\chi-n(I)}$
15	**2.0**	2.0	190	310	310	3500
30(upper)	**0.70**	1.7	1.2	**20**	270	22
30(lower)	**0.10**	0.24	0.17	**5.0**	68	5.4
50(upper)	**0.60**	3.2	0.74	**13**	520	13
50(lower)	**0.10**	0.53	0.12	**3**	120	3.1
60(upper)	**0.45**	2.8	0.54	**12**	590	12
60(lower)	**0.13**	0.82	0.16	**3.0**	150	3.1
80(upper)	**0.40**	3.2	0.46	**11**	670	11
80(lower)	**0.22**	1.7	0.25	**4.1**	250	4.2
100	**0.90**	7.6	1.0	15	1100	15

Table 6.13: $\sigma^{SD}_{\chi-p}$ and $\sigma^{SD}_{\chi-n}$ limits of DAMA experiment used to calculate the results shown in Fig. 6.14, Fig. 6.15, and Fig. 6.16. Values for 15GeVc^{-2} and 100GeVc^{-2} are taken from the limits data in Ref.[53] and values for 30GeVc^{-2}, 50GeVc^{-2}, 60GeVc^{-2} and 80GeVc^{-2} are taken from the allowed region data in Fig. 2.7[31]. In the Ref.[31], only the $\sigma^{SD}_{\chi-p(NaI)}$ and $\sigma^{SD}_{\chi-n(NaI)}$ are shown(shown in **bold** in the Table), so we calculated the $\sigma^{SD}_{\chi-p(Na)}$, $\sigma^{SD}_{\chi-n(Na)}$, $\sigma^{SD}_{\chi-p(I)}$, and $\sigma^{SD}_{\chi-n(I)}$ values with the sensitivities of Na and I at the threshold considering the detector responses described in Ref.[53]. As for 15GeVc^{-2} and 100GeVc^{-2} data, only $\sigma^{SD}_{\chi-p}$ limits are shown in the Ref.[53], therefore we also calculated $\sigma^{SD}_{\chi-n}$ limits from the $\sigma^{SD}_{\chi-p}$ limits. All of the cross section data are shown in units of pb.

Chapter 7

Discussions

The results of this experiment suggest that we still need to reduce the background by more than an order of magnitude for the dark matter detection. We will discuss on the remaining background in this section using the high energy data. For the convenience of the discussion, we define three energy regions as follows:

1	DM energy	20*-80 keV	effective for the dark matter signals
2	γ/β energy	200-1000 keV	γ-rays and β-rays are the dominant background
3	α energy	3-10 MeV	α-rays are the dominant background

The count rates obtained with the seven bolometers for the three energy regions are summarized in Table 7.1. The spectra of the higher energy regions are shown in Fig. 7.1 and Fig. 7.2.

7.1 Contaminations within the Crystals

In a low background experiment, contaminations within the detector often determine the background level. We will start the estimation of the remaining background with the contaminations within the LiF crystals.

7.1.1 Uranium and Thorium in the LiF Crystals

Uranium and thorium are radioactive contaminations that often limit the sensitivities of the detectors in many low background experiments. As the polishing powder contains uranium

*The lower limits of the DM energy region is set to the lowest energy of the flat spectrum and differ among the detectors. The energies are shown in Table 7.1.

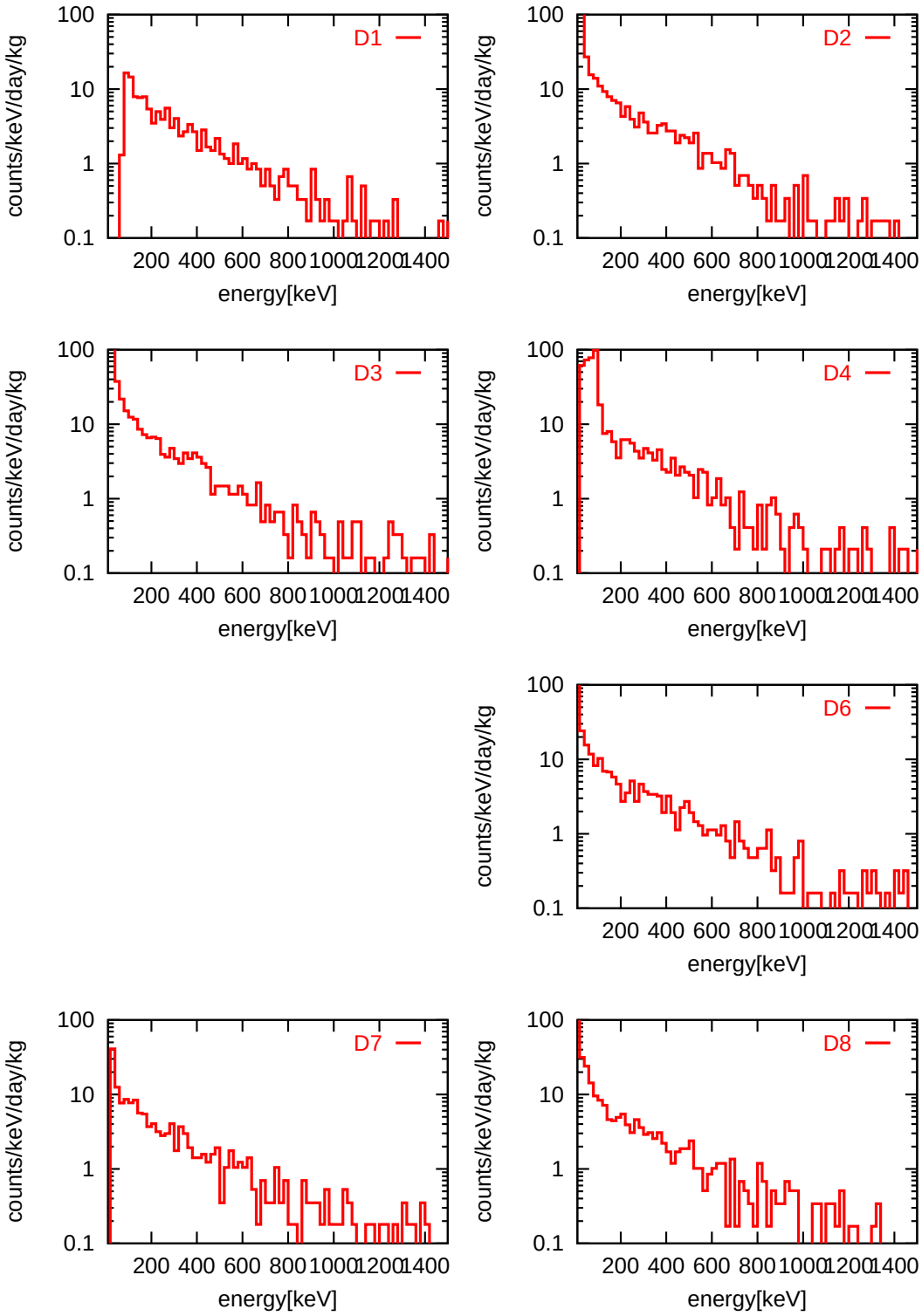

Figure 7.1: Energy spectra of the γ/β energy region obtained with the seven bolometers.

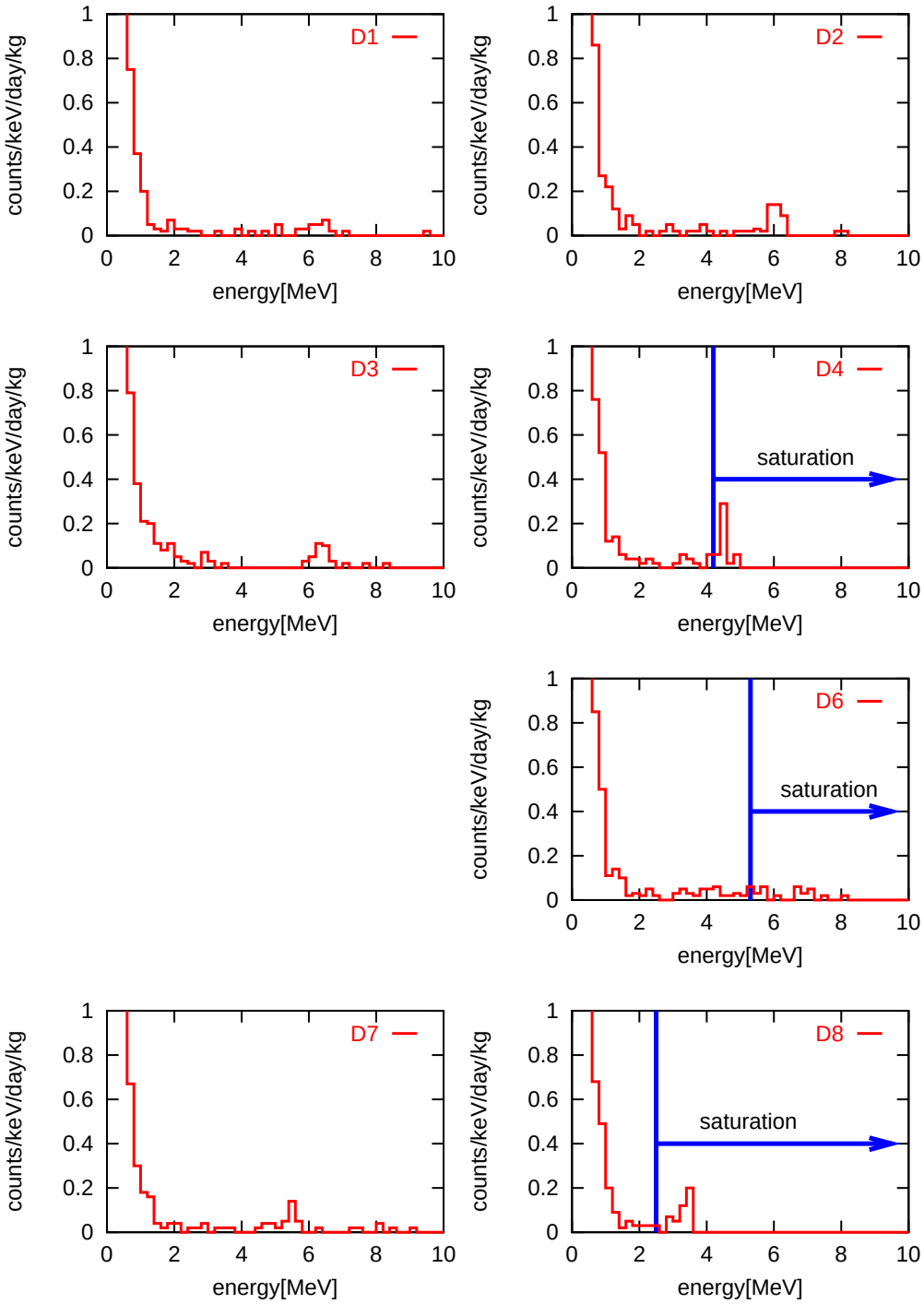

Figure 7.2: Energy spectra of the α energy region obtained with the seven bolometers. The spectra of D4, D6, and D8 lose the information on the shapes because of saturation.

	LiF ID	etching [μm]	DM [keV]	averaged [c/keV/kg/day]	γ/β energy [10^{-3}c/kg/s]	α energy [10^{-3}c/kg/s]
D1	BIC[†]1	21	-	-	20	1.1±0.2
D2	BIC2	22	50-80	16	15	1.8±0.3
D3	BIC3	26	40-80	29	17	1.1±0.2
D4	BIC4	29	60-80	59	18	1.5±0.3
D6	OK[‡]3	24	30-80	15	15	1.7±0.3
D7	OK4	27	30-80	11	12	1.4±0.2
D8	OK5	27	30-80	20	14	1.0±0.2
D1-D4(avgd)	BIC				17	1.4±0.1
D6-D8(avgd)	OK				14	1.4±0.2
Run4/D8	RM[§]5	0	20-80	26	32	7.1±0.1
Run8/D3	BIC3	2	60-80	170	63	1.3±0.2

Table 7.1: Count rates of the seven bolometers in the three energy regions. The rates are shown in units of counts/keV/kg/day for the DM energy region. The unit for the higher energy regions is 10^{-3}counts/kg/sec as this is a convenient unit for the estimation of the contamination. The results of the Run4 and Run8 are shown together for the reference.

and thorium as shown in Table 5.10, we estimate the background from the uranium and thorium contamination.

- Amount of the Contamination
  The background in the α energy region can have two causes: α-rays from the uranium and thorium contaminations inside the crystals and muons going through the crystals. The latter is estimated to be two orders of magnitude smaller than the obtained rate as described in Section 7.2.5. Therefore, the background in the α energy region can be attributed to the α-rays from the uranium and thorium contaminations. As we have etched the surfaces of the crystals between 20 μm and 30 μm, the surface contaminations are now negligible and the peaks can be attributed to homogeneous distribution over the volume.

  As the count rate in the α energy region obtained in this experiment is very low and it is difficult to estimate the contaminations of ^{238}U, ^{232}Th, and ^{210}Pb separately, we have estimated each amount of ^{238}U, ^{232}Th, and ^{210}Pb by scaling the result of Kamioka-run4. Results of this experiment, Kamioka-run4, and the estimated contaminations are shown in Table 7.2. As the count rates of the crystals from BICRON Co. Ltd. are not

[†]Purchased from BICRON Co. Ltd.
[‡]Purchased from OHYO KOKEN KOGYO Co. Ltd.
[§]Purchased from Rare Metallic Co. Ltd.

different from those from OHYO KOKEN KOGYO Co. in the α region, we used the average of all the detectors.

	α energy rate(result) $[10^{-3}$c/s/kg]	^{238}U $[10^{-12}$g/g]	^{232}Th $[10^{-12}$g/g]	^{210}Pb $[10^{-3}$Bq/kg]
Run4/D8	7.1	34	12	0.53
This work	1.4	9.6	3.4	0.15

Table 7.2: α energy count rates and contaminations of ^{238}U, ^{232}Th, and ^{210}Pb of D8 of Kamioka-run4 and the average of this work. The α energy count rates are the integrated rate of the experimental results. ^{238}U, ^{232}Th, and ^{210}Pb contaminations in run4 are the measured values, while those of this work are estimated values by scaling.

- Count Rate in the DM Energy Region
  We simulate the background from the uranium and thorium using the values in Table 7.2. We assumed a homogeneous distributed contamination over the volume as we have etched the surfaces of the crystals deep enough compared to the ranges of the α-rays in the LiF crystal. Simulated count rate in the DM energy region is about 0.3 counts/keV/kg, which is negligible to the current background rate. This measured result has about $\pm$20% statistical error which dominates the error of this background estimation.

7.1.2 Potassium in the LiF Crystals

The polishing powder used at BICRON Co. Ltd. contains a certain amount of potassium in it as shown in Table 5.10. If grains of these polishing powder remain on the surface of the LiF crystals, they would be a serious source of the background. Potassium has an radioactive isotope ^{40}K and the decay scheme is shown in Table 7.3.

β^-	89.3%	Q_β=1.312MeV
EC	10.7%	E$_\gamma$=1.461MeV
		natural abundance : 0.0117%
		half life : 1.277×10^9years.

Table 7.3: Decay scheme of ^{40}K.

- Amount of the Contamination
  As the result of the survey of the LiF crystal with HPGe spectrometer gives only the

upper limits, we estimated the amount of the potassium contamination assuming that all events in the γ/β energy region are from the potassium contamination. We used the D3 results of this experiment and Run8/D3 results listed in Table 7.1. We etched the surface of D3 about 2μm for Run8, while we etched the surface about another 26μm for this experiment.

First we assumed the depth of the remaining contamination by scaling the depth of the etching with the count rate in the γ/β region as follows.

$$d_{\rm remain} = d_{\rm etching} \cdot \frac{R^{\rm D3}_{\gamma/\beta}}{R^{\rm Run8/D3}_{\gamma/\beta} - R^{\rm D3}_{\gamma/\beta}} = 26 \cdot \frac{17}{63-17} \sim 10\mu{\rm m} \tag{7.1}$$

where $d_{\rm remain}$ is the depth of the remaining ^{40}K contamination, $d_{\rm etching}$ is the depth of the etching for this experiment, $R^{\rm D3}_{\gamma/\beta}$ is the count rate in the γ/β region of D3 in this experiment, and $R^{\rm Run8/D3}_{\gamma/\beta}$ is the count rate in the γ/β region of Run8/D3. The depth of the remaining potassium contamination is estimated to be about 10 μm.

We then estimated the amount of the contamination comparing the simulation results with the experimental results in the γ/β energy region. Results are shown in Fig. 7.3. The best fit is 13000ppm contamination of potassium distributed in the depth of 10μm from the surface. This amount is equivalent to 39ppm concentration of a homogeneously distribution over the volume.

- Count Rate in the DM Energy Region
  We estimated the background from ^{40}K in the DM energy region with the values estimated above. The simulation result is shown in Fig. 7.4. We assumed 13000ppm contamination of potassium distributed in the depth of 10μm from the surface. It is seen that ^{40}K contamination makes 6 counts/keV/kg/day background in the DM energy region. As this background estimation is based upon the assumption that all events in the γ/β energy region are from potassium contamination, the lower value is 0 counts/keV/kg/day, while we still can have 50% excess in the DM region if we assume thinner contamination depth. Therefore the systematic error dominates the error and the result is 6^{+3}_{-6} counts/keV/kg/day.

7.1.3 Tritium in the LiF Crystals

Lithium has an isotope ^{6}Li with natural abundance of 7.5% whose neutron capture cross section is 942barn. The tritium produced by the neutron capture decays with a half life of 12.3years. The decay scheme is shown below.

$$\begin{aligned} {}^6{\rm Li} + {\rm n} &\rightarrow {}^3{\rm H} + \alpha \quad (Q_\alpha = 4.78{\rm MeV}) \\ {}^3{\rm H} &\rightarrow {}^3{\rm He} + e^- + \bar{\nu}_e \quad (Q_\beta = 18.6{\rm keV}) \end{aligned}$$

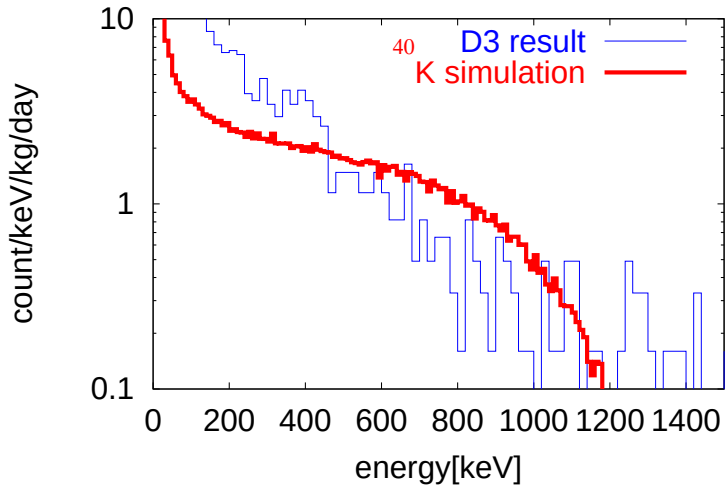

Figure 7.3: Simulation and experiment results of the potassium contamination in the γ/β energy region. The experimental result is shown in blue, while the simulation result is shown in red. We assumed the contamination is distributed in 10μm from the surfaces and obtained the best fit value of 13000ppm there.

The Q_β is 18.6 keV and there is a possibility that these β-rays dominate the background below 20keV.

- Amount of the Contamination
  As we have used the crystals OK2,3,4,5 since the 'Pilot Run', we have exposed these crystals to the ambient neutron during the 'Modification' period at the surface laboratory in Table 4.1. In addition, we used the neutron capture reaction for the calibration with Q_α=4.78MeV shown above by irradiating ^{252}Cf neutron source. The exposure of the OK2,3,4,5 to the ambient neutrons at surface laboratory is at most 200 days and the irradiation of the ^{252}Cf source corresponds to less than 1/10 of the exposure at the surface laboratory. We take 300 days as a typical value of the effective exposure at the surface laboratory. The crystals BIC 1,2,3,4 were not exposed to the ambient neutrons at the surface laboratory. The radioactivity of the tritium produced by the neutron capture can be calculated to be

  $$5.5 \times 10^{-5} t[\text{counts/kg/s}] \tag{7.2}$$

  where t is the exposure in units of days and we assumed the values listed in Table 7.4.

- Count Rate in the DM Energy Region
  We estimated the background from the ^{3}H using Eq. (7.2). The simulation result is

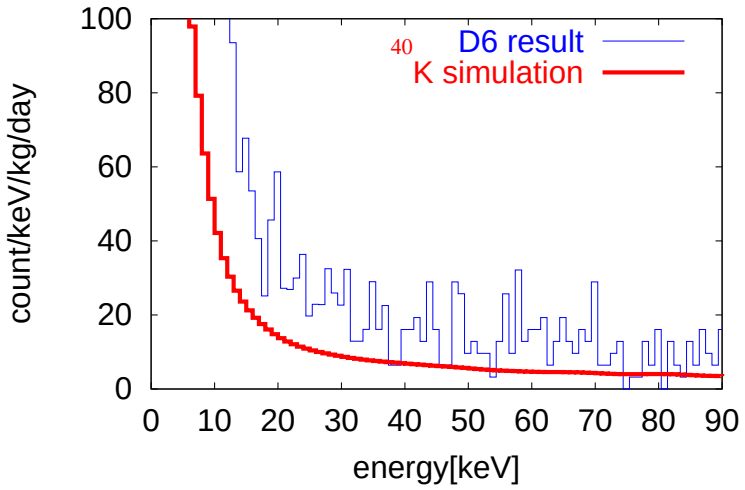

Figure 7.4: Simulation and experiment result of the potassium contamination in the DM energy region. The experimental result is shown in blue, while the simulation result is shown in red. We assumed the contamination of 13000ppm is distributed in 10μm from the surfaces.

Dimension of the crystal	$2 \times 2 \times 2\text{cm}^3$
Thermal neutron flux[62]	$1.9 \times 10^3\text{cm}^{-2}\text{s}^{-1}$
Natural abundance of ^{6}Li	7.5%
Capture cross section	942barn
Half life of ^{6}Li	12.3years

Table 7.4: Values used for the estimation of the tritium background.

shown in Fig. 7.5. The total radioactivity is about 1.7×10^{-2}Bq/kg and about 10% of it deposit energies higher than 10keV. Thus the count rate averaged between 10keV and 20keV is 1.7×10^{-3}counts/kg/sec, which is equivalent to 15 counts/keV/kg/day. Though this is smaller than the experimental result, it is possible to explain the spectra below 20keV by the β-rays from ^{3}H considering the ambiguity of the exposure during the manufacture and other unknown periods. The ambiguities of the exposure and the calculation can cause about $\pm$20% of systematic error.

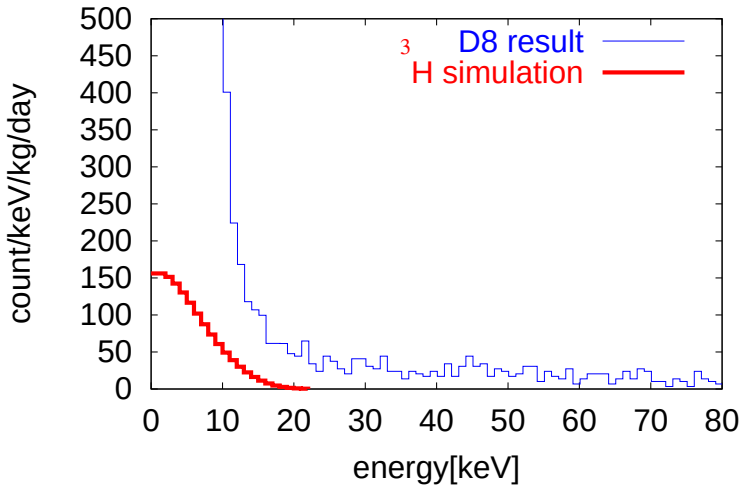

Figure 7.5: Simulated background of the ^{3}H. We assumed a 300days exposure to the ambient neutron at the surface. The spectrum of the D8 is shown together for the reference.

7.2 Background from Outside

7.2.1 Crystal Holder and Inner Shield

- Amount of the Contamination
  The OFHC copper used for the crystal holder and the Kanazawa lead for the inner shield was surveyed with ICP-MASS method[73]. The results are shown in Table 7.5.

	^{238}U[ppb]	^{232}Th[ppb]
OFHC copper	< 0.1	0.6
Kanazawa lead	< 0.1	1.4

Table 7.5: Contaminations in the OFHC copper and Kanazawa lead[73].

- Count Rate in the DM Energy Region
  With the values listed in Table 7.5, we estimated the background from the holder and the inner lead by simulation[79]. The results are shown in Fig.7.6 and Table 7.6. From the results of the simulation, we can see that the holder and the inner shield make almost the same contribution. The background from the contaminations in the crystal holder and the inner shield can explain at least 10% of the remaining background. The systematic error of the ICP-MASS measurement dominates the error, which is estimated to be $\pm$50%.

source	count rate[counts/keV/day/kg]
holder	2
inner lead	3

Table 7.6: Simulation results of the background from the uranium and thorium contaminations in the OFHC copper for the crystal holder and the Kanazawa lead for the inner shield. Averaged count rates between 20keV and 80 keV are shown.

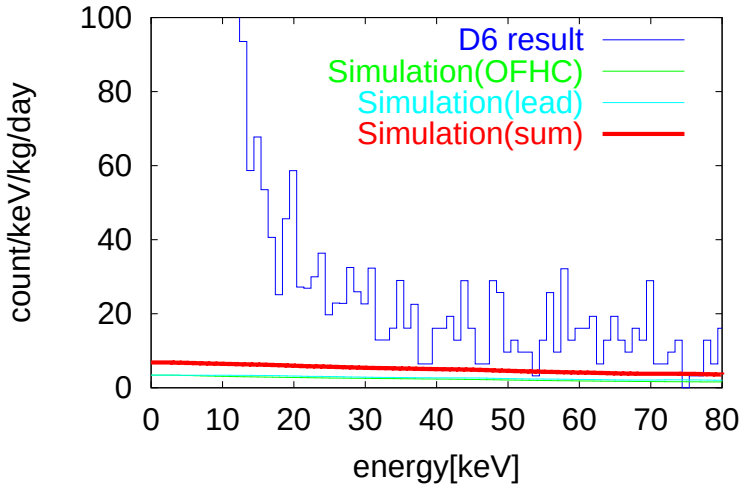

Figure 7.6: Simulation results of the background from the uranium and thorium contaminations in the OFHC copper for the crystal holder and the Kanazawa lead for the inner shield. The spectrum of the the experimental, sum of OFHC and lead are also shown.

7.2.2 Ambient Neutron

The flux of the fast neutron at the Kamioka Observatory was previously measured and the background by the elastic scattering of the fast neutron is estimated. The flux of the fast neutron at Kamioka Observatory is $2 \times 10^{-5}\mathrm{cm}^2\mathrm{s}^{-1}$[65]. The estimated count rate due to the elastic scattering of the neutron in the DM energy region is below 0.1 counts/keV/kg/day without the shield. The coverage of the neutron shield is about 85%. If we assume a reduction of about one order of magnitude, the count rate in the DM energy region will be 0.01 counts/keV/kg/day.

7.2.3 Ambient Gamma and Beta Rays

As we have no information on gamma rays at Kamioka Observatory, we will estimate from the values we measured at Nokogiriyama underground cell and the surface laboratory. The background level at Nokogiriyama underground cell in the DM energy region was 170 counts/keV/kg/day without the inner shield. We assume this is all from the ambient gamma and beta rays and the fluxes of ambient gamma and beta rays at Kamioka Observatory are same. The inner lead would reduce the background at least two orders magnitude and the rate will be less than 2 counts/keV/kg/day.

7.2.4 Gamma and Beta Rays from the Radon Gas

Radon gas in the space between the Dewar for the dilution refrigerator and the heavy shield are purged with nitrogen gas. The concentration of the radon gas is monitored to be less than 0.2Bq/m^3 throughout the measurement period. This concentration of radon gas would make background of less than 0.1 counts/keV/kg/day in the DM energy region[80]. Thus the background from the radon gas is negligible.

7.2.5 Cosmic Ray Muon

The flux of the cosmic ray muon at Kamioka Observatory is about 10^{-7}cm^{-2}s^{-1}. This is four orders of magnitude smaller than that of Nokogiriyama underground cell. The count rate in the DM energy region obtained in the pilot run without the muon veto is about 350 counts/keV/kg/day[62]. Considering this rate is all induced by the comic ray muon, the muon induced background rate at Kamioka Observatory is estimated to be less than 0.05 counts/keV/kg/day and this is a negligible value compared to the results shown in Table 7.1. The contribution to the α energy region by minimum ionization events of muons going through the crystal corresponds to 1.9×10^{-5}counts/kg/sec, which is two orders of magnitude smaller than the background rates shown in Table 7.1.

7.3 Summary

In Table 7.7 and Fig. 7.7, results of the background studies are shown.

The ^{40}K contamination in the LiF crystal and the contaminations in the crystal holder and inner shield are found to be the main background sources in the DM region. The tritium contamination and the ^{40}K contamination are thought to be the cause of the steep rise of the low energy spectra below 20keV. Though we have not discussed on the energy range below 20keV, if we reduce the background in that energy region, better sensitivities to the dark matter would be achieved.

For the further improvement, we need to reduce the background inside the detector, and the background from the crystal holders and the inner shield. Plans of the improvements are described in the following Section.

Source	Count rate	Note
Exp. results	11∼29	
U,Th in LiF	0.3 ± 0.1	
^{40}K in LiF	6^{+3}_{-6}	10μm surface contamination is assumed.
^{3}H in LiF	15 ± 3	10-20keV averaged
OFHC holder	2 ± 1	
Kanazawa lead	3 ± 1.5	
Ambient neutron	< 0.1	
Ambient γ and β	< 2	
Rn	< 0.1	
μ	< 0.1	
BG simulation total	11^{+5}_{-7}	

Table 7.7: Results of the background studies. Count rate are shown the values of the DM energy region. They are shown in units of counts/keV/day/kg. As the baseline of D4 is noisier than other detectors and the spectrum of D4 in the DM energy region might be contaminated by the electric noise, we did not use the D4 result to show the 'Exp. result' in the table.

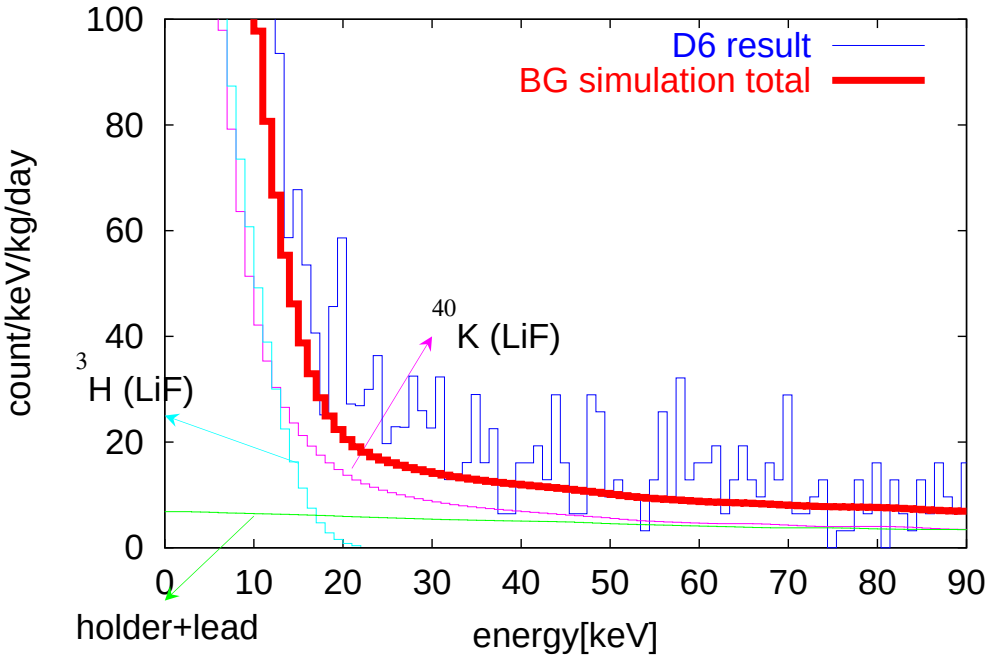

Figure 7.7: Results of the background studies. The experimental result of the D6 is shown in blue, while the simulated total background is shown in red. Three dominant background sources are also shown.

Chapter 8

Future Prospects

8.1 Further Background Reduction

As the crystals purchased from OHYO KOKEN KOGYO Co. Ltd. might have tritium contamination in them, we will focus on the further purification of the crystals purchased from BICRON Co. Ltd. If the background in the crystals from BICRON Co. Ltd. are due to the potassium contaminations, we will be able to remove the contaminations by etching the surface of the crystals moer than another 10μm. As the crystals from BICRON Co. Ltd. have not been exposed to the ambient neutrons, we can expect less count rate in the energy region below 20keV.

8.2 Measurements with Other Materials

One of the features of the bolometer is that we have a wide choice of the target materials. If we use NaF as the target material, we can expect better sensitivities in the $a_p - a_n$ plane since Na has a large $C^{SD}_{n(N)}/C^{SD}_{n}$ value compared to Li as shown in Table 3.2. Expected sensitivities in the $a_p - a_n$ plane with NaF target are shown in Fig. 8.1. Here we assume the same spectrum as that of LiF target.

8.3 Background Reduction with Active Shield

As the background from outside of the LiF crystal, especially from the OFHC copper holder and Kanazawa lead, contributes a certain fraction of the background, we need to reduce these background for better sensitivities. We are planning to adopt an active shield to reduce the background from outside. A. Takeda suggests to install an active shield by the following two steps[85].

1. Active shield with LiF bolometers

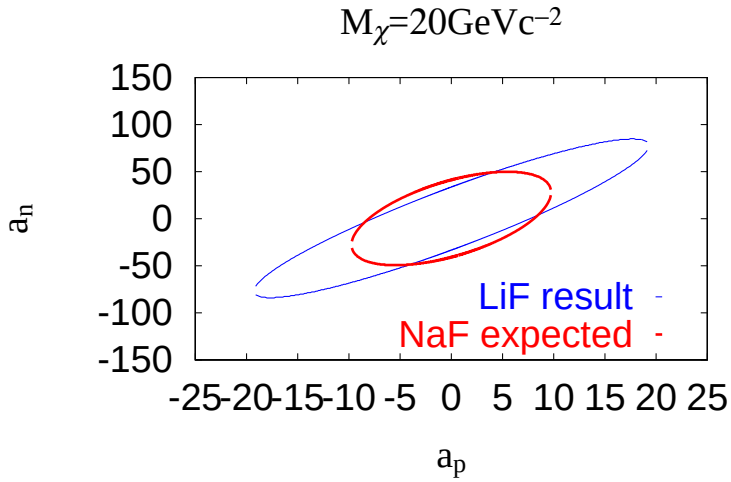

Figure 8.1: Expected limits in the a_p-a_n plane with a NaF bolometer. Here we assume the same spectrum as that of LiF target.

2. Active shield with Ta bolometers

Schematic drawings of these two configuration are shown in Fig. 8.2. Expected sensitivities with the second step are shown in Fig. 8.3.

8.4 Directional Detectors

For the positive sign of the neutralino, the only method to identify it is annual modulation in the currently going measurements[22]. This method requires stability of the detector, large mass, long live time. The difference in the count rate due to the modulation of the relative velocity of the earth to the dark matter sea is only a few percent. If we can detect the direction of the recoil, on the other hand, it is estimated that we can detect a positive sign[87] with much more accuracy. There are two plans for the development of directional detectors.

8.4.1 Anthracene Detector

It is known that anthracene scintillation detectors have a direction dependence of their light yields. If we measure the total recoil energy together with the scintillation light, we'll be able to know the recoil direction [86].

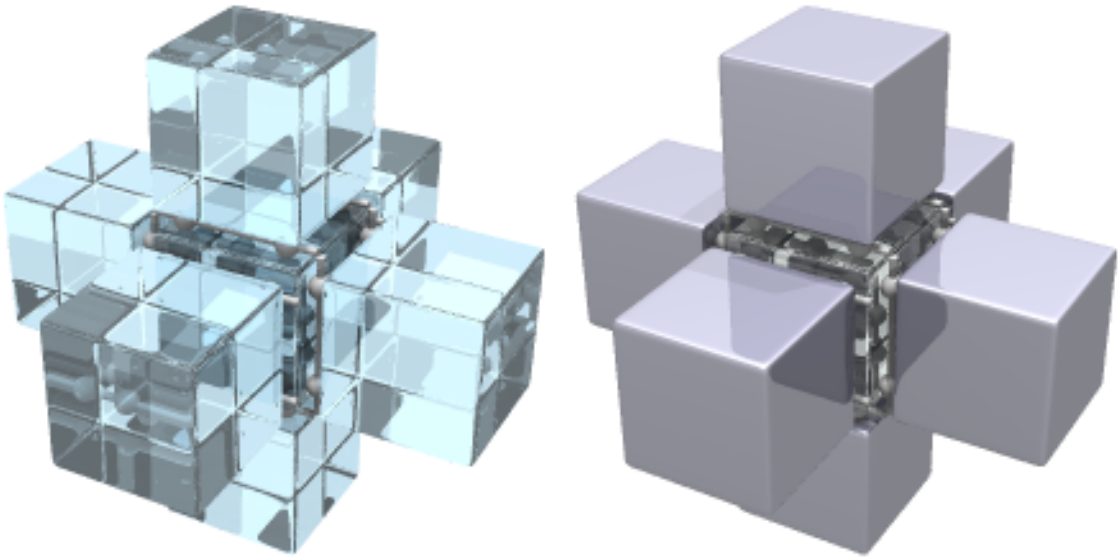

Figure 8.2: Designs of active shield for the LiF bolometer[85]. Schematic drawing of the detector system for Step1(LiF crystals are used for the active shield.) and Step2(Ta crystal are used.) are shown.

8.4.2 MPGC-TPC Detector

There has been an attempt to detect the direction of the recoil[87]. However, the threshold was not been low enough for the dark matter detection because of the poor resolution of the position. There is a suggestion to apply an MPGC-TPC(Micro Pixel Gas Chamber-Time Proportional Chamber) detector for a dark matter detection[88]. MPGC has high position resolution and scaling-up is relatively easy, therefore this would be a promising method for the dark matter detection.

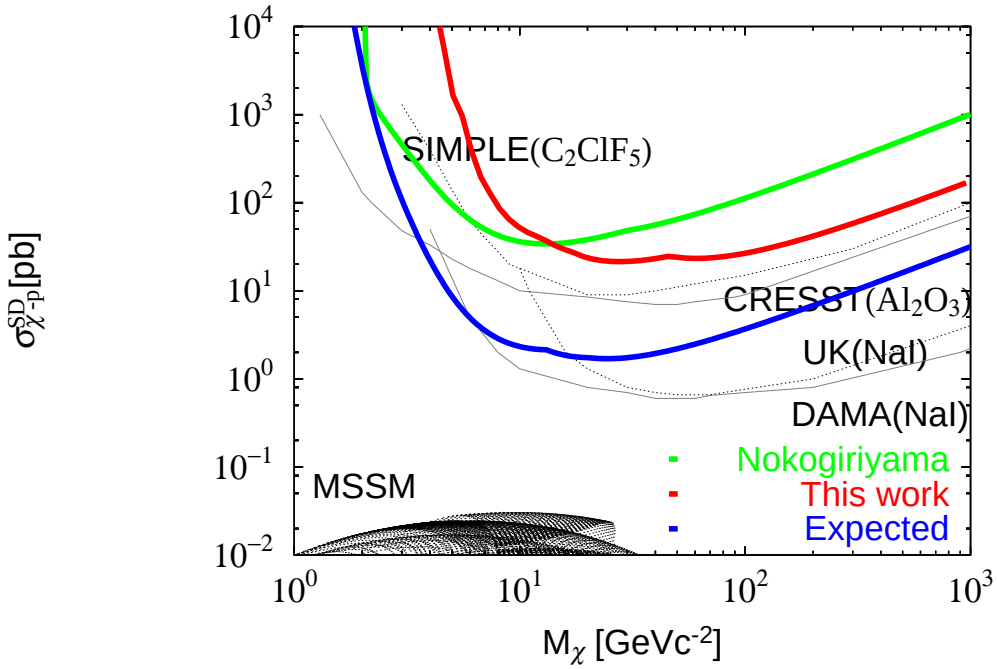

Figure 8.3: Expected sensitivities with Ta active shield[85].

Chapter 9

Conclusions

- $\sigma^{\mathrm{SI}}_{\chi-\mathrm{p}}$ and $\sigma^{\mathrm{SD}}_{\chi-\mathrm{p}}$ limits
  In this experiment, we have obtained the $\sigma^{\mathrm{SI}}_{\chi-\mathrm{p}}$ limit of 0.055 pb and $\sigma^{\mathrm{SD}}_{\chi-\mathrm{p}}$ limit of 21 pb for $M_\chi = 28\mathrm{GeVc}^{-2}$. M_χ dependence of the limits are shown in Fig. 6.11 and 6.12.

- Limits in the $\sigma^{\mathrm{SD}}_{\chi-\mathrm{p}}$-$\sigma^{\mathrm{SD}}_{\chi-\mathrm{n}}$ plane
  We derived the limits in the $\sigma^{\mathrm{SD}}_{\chi-\mathrm{p}}$-$\sigma^{\mathrm{SD}}_{\chi-\mathrm{n}}$ plane and compared our result with DAMA's results as shown in Fig. 6.14 and Fig. 6.15. For the $\langle a_{\mathrm{p}} \rangle / \langle a_{\mathrm{n}} \rangle < 0$ neutralinos, we have obtained the following results:

  1. For neutralinos lighter than $15\mathrm{GeVc}^{-2}$, we excluded a part of the $\sigma^{\mathrm{SD}}_{\chi-\mathrm{p}}$-$\sigma^{\mathrm{SD}}_{\chi-\mathrm{n}}$ plane that is not excluded by DAMA's result.
  2. For neutralinos heavier than $50\mathrm{GeVc}^{-2}$, we excluded a part of the $\sigma^{\mathrm{SD}}_{\chi-\mathrm{p}}$-$\sigma^{\mathrm{SD}}_{\chi-\mathrm{n}}$ plane that is allowed by DAMA's annual modulation result.
  3. For neutralinos heavier than $100\mathrm{GeVc}^{-2}$, we excluded a part of the $\sigma^{\mathrm{SD}}_{\chi-\mathrm{p}}$-$\sigma^{\mathrm{SD}}_{\chi-\mathrm{n}}$ plane that is not excluded by DAMA's result.

- Limits in the a_{p}-a_{n}(neutralino-nucleon spin-dependent couplings) plane
  We derived the limits in the a_{p}-a_{n} plane as shown in Fig. 6.16. The results are as follows.

  1. For neutralinos lighter than $15\mathrm{GeVc}^{-2}$, we excluded a part of the a_{p}-a_{n} plane that is not excluded by DAMA's result.
  2. For neutralinos heavier than $50\mathrm{GeVc}^{-2}$, we excluded a part of the a_{p}-a_{n} plane that is allowed by DAMA's annual modulation result.
  3. For neutralinos heavier than $100\mathrm{GeVc}^{-2}$, we excluded a part of the a_{p}-a_{n} plane that is not excluded by DAMA's result.

- This is the only experiment that excluded a part of the parameter space of DAMA's annual modulation signal in the $\sigma^{\mathrm{SD}}_{\chi-\mathrm{p}}$-$\sigma^{\mathrm{SD}}_{\chi-\mathrm{n}}$ plane and the a_{p}-a_{n} plane.

- This is the only experiment that has set a finite allowed region in the a_{p}-a_{n} plane for neutralinos lighter than 15GeVc^{-2}.

Acknowledgements

I wish to first thank my adviser Prof. M. Minowa for his excellent guidance, support, and patience. I really appreciate having learned various things from his broad knowledge on physic and other things.

I want to thank my collaborators: Y. Inoue, Dr. Y. Ito, Dr. S. Moriyama, Dr. W.Ootani, Dr. T. Watanabe, A. Takeda, H.Sekiya, Y.Shimizu, and Prof. Y. Ootuka for many useful discussions and good advices. I especially thank A. Takeda, H.Sekiya, and Y.Shimizu for their devoted help for the running of this experiment.

I want to thank other members of Minowa group, T. Namba, Y. Takasu, T. Taniguchi, T. Horiuchi, and T. Ichiki for their helpful discussions.

I want to express my gratitude to Prof. Komura at Kanazawa University for offering 25kg of very low background lead. Without this lead, this experiment would not get much improvement like this.

I want to express my gratitude to all of the staff of Kamioka Observatory, Institute for Cosmic Ray Research(ICRR), University of Tokyo for their help in performing this experiment. I wish to thank then for preparing a new laboratory for this dark matter experiment, allowing us to use the control room of the Super-Kamiokande detector, the office, and the dormitory, sharing the air from outside of the mine, giving us lifts to the mine every day, and allowing us to use the HPGe spectrometer in the Kamioka mine.

I want to thank International Center for Elementary Particle Physics University of Tokyo (ICEPP) for allowing me to use its workstations, facsimile, scanners, library, and so on. I would like to thank S. Otsuka for his advice and support of our engineering work.

I want to thank S.Sato in the gravitational group for many pieces of precious advices especially on the suspension of the detector.

I want to thank the dark matter competitors in Japan: the ELEGANT group and Xmass group for a lot of useful discussions.

I want to express my gratitude to my friends in the same year at Hongo: N. Isobe, Y.Matsumoto, Y. Terada; and at Kamioka: K. Kobayashi, S. Nakayama, and S.Yamada. They always encouraged me whenever needed.

I want to thank M. Tomoyama and his family for their support throughout my university years.

Last but not least I want to thank my family members: M. Miuchi, K. Miuchi and Y.Miuchi for their kind help and encouragement.

Appendix A

Preceding Runs at Kamioka Observatory

We have performed several test runs at Kamioka Observatory. Here we will summarize the run data of the test runs. The detector set-ups for all of the runs are summarized in table A.2.

A.1 Kamioka-run1

A.1.1 Run Data of Kamioka-run1

Refrigeration Start	December 14, 1999
Measurement Start	-
Shutdown	December 20, 1999

Table A.1: Run data of Kamioka-run1

A.1.2 Run Summary of Kamioka-run1

- This run was the test of the cryogenics.
- No detector was mounted.

Run/Set-up	D1	D2	D3	D4	D5	D6	D7	D8
2/NTD	3-18	3-17	3-4	3-13	3-13	3-1	3-6	3-16
2/LiF	OK[†]2	OK3	OK4	OK5	RM[‡]1	RM3	RM4	RM5
3/NTD	3-18	3-17	3-4	3-13	3-13	3-1	3-6	3-16
3/LiF	OK2	OK3	OK4	OK5	RM1	RM3	RM4	RM5
4/NTD	3-1r	3-17	3-6	3-2r	3-13	3-1	3-4	3-16
4/LiF	OK2	OK3	OK4	OK5	RM1	RM3	RM4	RM5
5/NTD	3-3i	3-17	3-4	3-2r	3-4r	3-3r	3-6	3-16
5/LiF	OK2[¶]	OK3	OK4[¶]	OK5[¶]	RM1[¶]	RM3	RM4	RM5
6/NTD	3-3i	3-17	3-4	3-2r	3-4r	3-3r	3-6	3-16
6/LiF	BIC1[§¶]	BIC2[¶]	BIC3[¶]	BIC4[¶]	BIC5[¶]	BIC6[¶]	BIC7[¶]	BIC8[¶]
7/NTD	3-3i	3-17	3-4	3-2r	3-4r	3-3r	3-6	3-16
7/LiF	BIC1[¶]	BIC2[¶]	BIC3[¶]	BIC4[¶]	BIC5[¶]	BIC6[¶]	BIC7[¶]	BIC8[¶]
8/NTD	3-3i	3-17	3-4	3-2r	3-4r	3-3r	3-6	3-16
8/LiF	BIC1[¶]	BIC2[¶]	BIC3[¶]	BIC4[¶]	BIC5[¶]	BIC6[¶]	BIC7[¶]	BIC8[¶]
9/NTD	2-1i	3-9r	3-4	3-7	4-3i	3-3r	3-6	3-16
9/LiF	BIC1[‖]	BIC2[‖]	BIC3[‖]	BIC4[‖]	OK2[‖]	OK3[‖]	OK4[‖]	OK5[‖]

Table A.2: Bolometer set up for preceding runs at Kamioka Observatory.

A.2 Kamioka-run2

A.2.1 Run Data of Kamioka-run2

Refrigeration Start	January 9, 2000
Measurement Start	-
Shutdown	January 19, 2000

Table A.3: Run data of Kamioka-run2

[†]OK:purchased from from OHYO KOKEN KOGYO Co. Ltd.
[‡]RM:purchased from Rare Metallic Co. Ltd.
[§]BIC:purchased from BICRON Co. Ltd.
[¶]The surface was etched with perchloric acid $\sim 2\mu$m.
[‖]The surface was etched with perchloric acid $20 \sim 30\mu$m.

A.2.2 Run Summary of Kamioka-run2

- No data was obtained due to the cold electronics problem.

A.3 Kamioka-run3

A.3.1 Run Data of Kamioka-run3

Refrigeration Start	January 23, 2000
Measurement Start	February 3, 2000
Shutdown	April 20, 2000

Table A.4: Run data of Kamioka-run3

A.3.2 Run Summary of Kamioka-run3

- This is the first run with the bolometers.
- Background rate was high because of the contamination during the bolometer assembly.

A.4 Kamioka-run4

A.4.1 Run Data of Kamioka-run4

Refrigeration Start	May 29, 2000
Measurement Start	June 2, 2000
Shutdown	August 31, 2000

Table A.5: Run data of Kamioka-run4

A.4.2 Run Summary of Kamioka-run4

- This run is referred to as 'preliminary underground run'.
- Bolometers were mounted in the control room of Super-Kamiokande where radon free air is sent from outside of the mine.

- Kanazawa lead and OFHC Copper was etched with nitric acid.
- Some parts of the OFHC copper holder were newly made.
- Low energy data were taken with the helium liquefier stopped.

A.5 Kamioka-run5

A.5.1 Run Data of Kamioka-run5

Refrigeration Start	November 13, 2000
Measurement Start	December 2, 2000
Shutdown	February 11, 2001

Table A.6: Run data of Kamioka-run5

A.5.2 Run Summary of Kamioka-run5

- The surfaces of four bolometers were etched with perchloric acid for test. The peaks of the α-rays were reduced.
- Bolometers were mounted in the control room of Super-Kamiokande.
- Signal lines were fixed to the frame of the dilution refrigerator for microphonic noise reduction, however, no improvement was seen.

A.6 Kamioka-run6

A.6.1 Run Data of Kamioka-run6

Refrigeration Start	April 10, 2001
Measurement Start	April 27, 2001
Shutdown	July 4, 2001

Table A.7: Run data of Kamioka-run6

A.6.2 Run Summary of Kamioka-run6

- Air supply from the outside of the mine started.
- Newly purchased crystals(BIC1,2,..., 8) were installed.
- New cold stage amplifier was installed.(gain: $\times 1 \rightarrow \times 10$).
- New crystal holder with delrin balls was installed.
- Signal lines between the thermistors and the cold stage amplifier was replaced with new cables.
- Nylon connector used for the signal lines was eliminated.
- No improvement was seen for the microphonic noise.

A.7 Kamioka-run7

A.7.1 Run Data of Kamioka-run7

Refrigeration Start	July 17, 2001
Measurement Start	-
Shutdown	August 3, 2001

Table A.8: Run data of Kamioka-run7

A.7.2 Run Summary of Kamioka-run7

- Bolometer array was suspended by the kevlar cords.
- Signal lines between the thermistors and the cold stage amplifier was partly replaced with low noise coaxial cables.
- No data was obtained as the thermal connection between the bolometer array and the dilution refrigerator was not enough.

Refrigeration Start	August 15, 2001
Measurement Start	August 23, 2001
Shutdown	September 24, 2001

Table A.9: Run data of Kamioka-run8

A.8 Kamioka-run8

A.8.1 Run Data of Kamioka-run8

A.8.2 Run Summary of Kamioka-run1

- The set up was same as that of Kamioka-run7 except some change in the thermal anchor.
- Microphonic noise was reduced.
- High level of contamination was detected in the crystals purchased from BICRON Co. Ltd.

A.9 Kamioka-run9

A.9.1 Run Data of Kamioka-run9

Refrigeration Start	October 12, 2001
Measurement Start	November 2, 2001
Shutdown	January 12, 2002

Table A.10: Run data of Kamioka-run9

A.9.2 Run Summary of Kamioka-run9

- The configuration of the kevlar cord suspension was slightly modified.
- All crystal were etched the surface $20 \sim 30\mu$m with with perchloric acid.
- 4 crystals were replaced with the ones used for till Kamioka-run5(OK2,3,4, and 5).
- Background of the crystals purchased from BICRON Co. Ltd was reduced.

Appendix B

Low Background HP Germanium Detector

The materials used for the detector and dilution refrigerator were carefully selected from the viewpoint of radioactive contamination. The measurements were performed with a low-background germanium gamma ray spectrometer(HPGe spectrometer). Usually we used our HPGe spectrometer operated at the Hongo campus of University of Tokyo, while we used the HPGe spectrometer operated at Kamioka Observatory owned by ICRR[70] for the survey of the LiF crystals purchased from BICRON Co. Ltd. Details of the both detector are listed in Table B.1. Fig. B.1 shows the schematic drawing of the HPGe detector system at Hongo. Inside of the OFHC is purged with gas nitrogen. Typical background spectrum obtained with the HPGe spectrometers are shown in Fig. B.2[89].

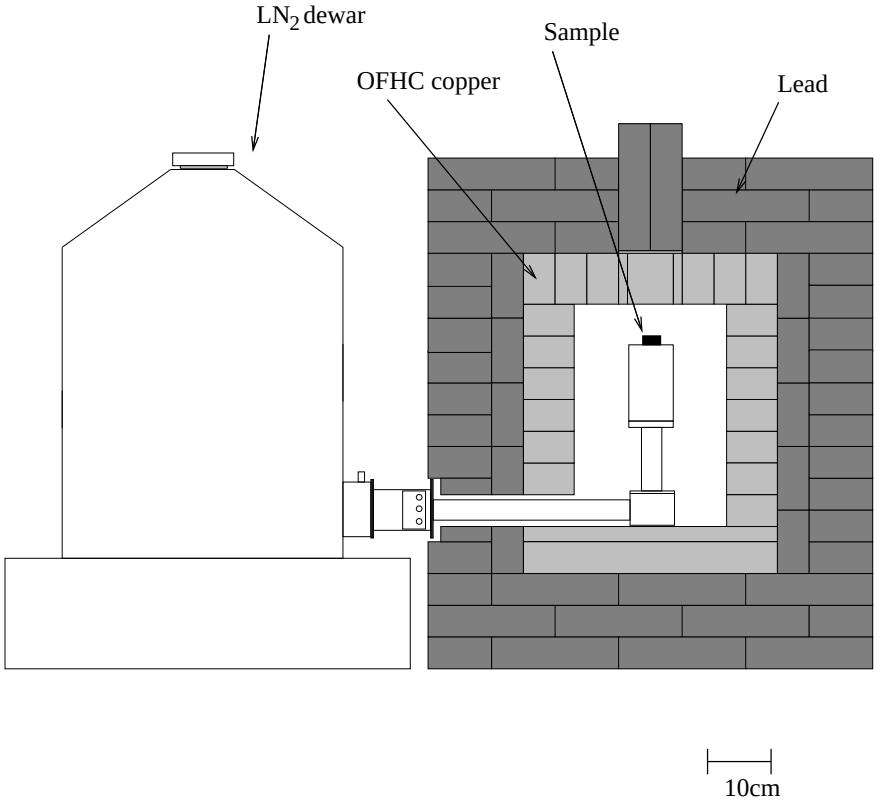

Figure B.1: Schematic drawing of low-background HPGe spectrometer at Hongo. The shield consists of 7.5cm-thick inner OFHC copper layer and 15cm-thick outer lead layer.

	Hongo	Kamioka
Product	EG&G ORTEC	Cambera
Model	GEM-25195	GC10021
Shape	Coaxial	Coaxial
Diameter	57.1mm	78.5mm
Length	54.6mm	78mm
Volume	134cm^3	370cm^3
Endcap	Mg(1.5mm)	Al(1.5mm)
Shield(inner)	7.5cm OFHC Copper	7.5cm OFHC Copper
Shield(outer)	15cm Lead	15cm Lead

Table B.1: The features of the HPGe spectrometeres.

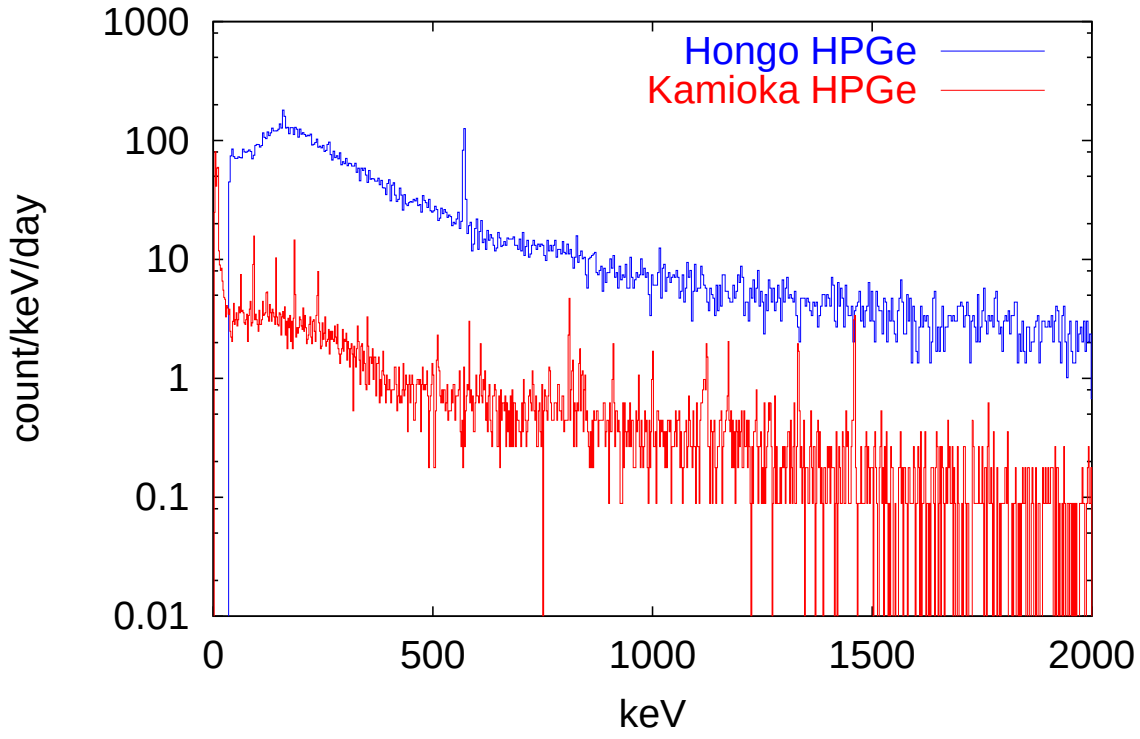

Figure B.2: Typical background spectra obtained with HPGe spectrometer at Hongo and Kamioka[89]. Live times are 0.84days and 5.6days for Hongo and Kamioka, respectively.

Appendix C

Accident of the Super-Kamiokande

There was a accident in the Super-Kamiokande about 11:00 on November 12, 2001. Strong earthquake was felt in our dark matter laboratory[77]. We were in the midst of calibrating the detector with the ^{137}Cs source. Signals of the seven bolometers ± 15 second of the accident are shown in Fig.C.1. Signals from the γ-ray source are seen and no disturbance is seen at the time of the accident.

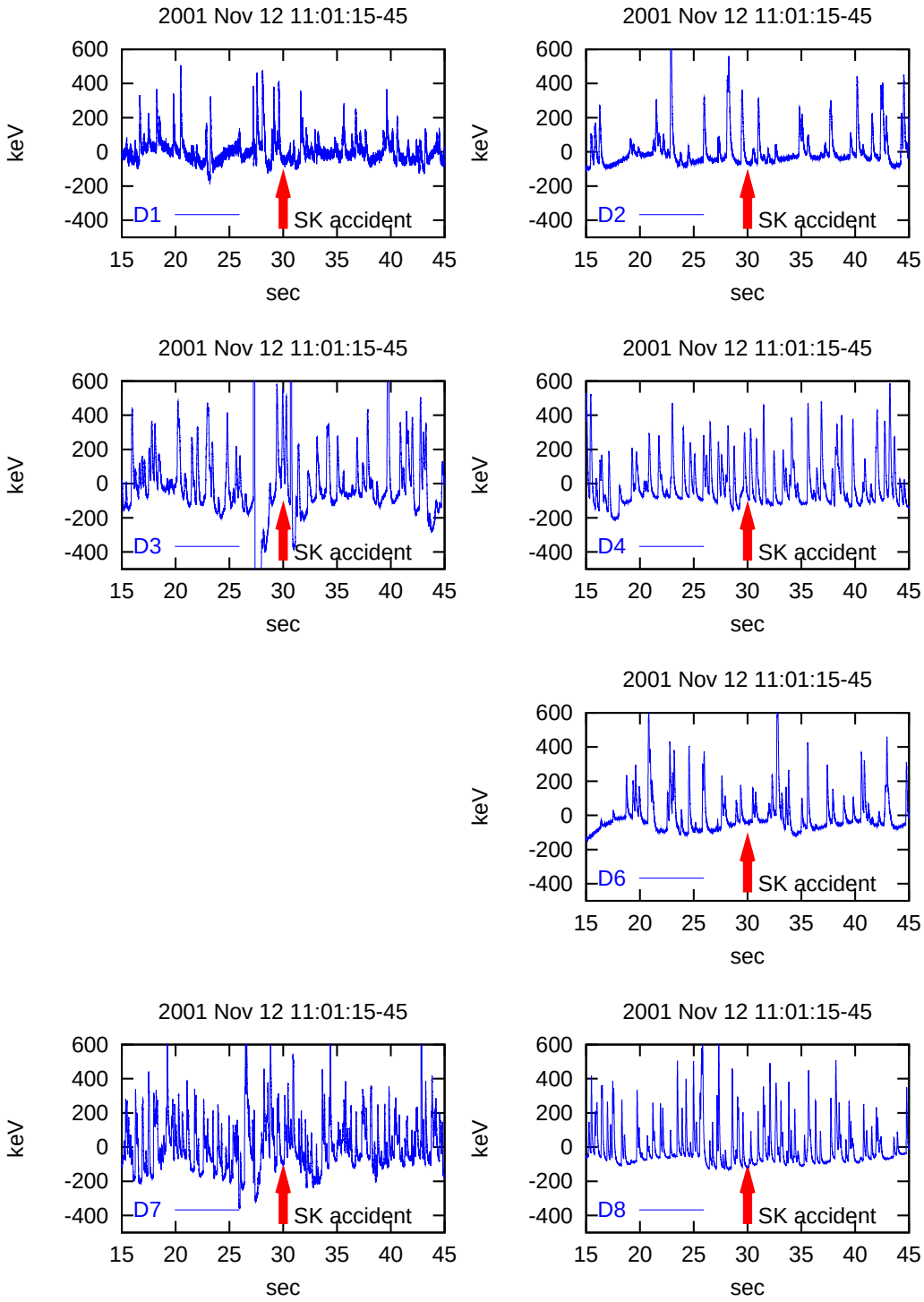

Figure C.1: Bolometer signals at the time of the Super-Kamiokande accident. Signals from the ^{137}Cs source are seen. No disturbance by the vibration due to the accident is seen. D3 has an undershoot because of the large signal just before the accident time.

Bibliography

[1] Review of Particle physics, Particle Data Group,The European Physical Journal C**15** (2000)1 and 2001 off-year partial update for the 2002 edition available on the PDG WWW pages (URL:http://pdg.lbl.gov/)

[2] V. Trimble, Ann. Rev. Astron. Astrophys.**25**(1987)425

[3] B. Sadoulet , Rev. Mod. Phys. **71**(1999)S197.

[4] P. de Bernardis et al., Nature **404**(2000)955

[5] A.Balbi et al., Astrophys. J. **545**(2000)L1, and S.Hanany et al., Astrophys. J. **545**(2000)L5

[6] S.Perlmutter et.al, Astrophys. J. **517**(1999)565

[7] E.I. Gates, G. Gyuk, and M.S. Turner, Astrophys. J. **449**(1995)L123

[8] W. Sutherland, Rev. Mod. Phys. **71**(1999)421.

[9] K.A. Olive, G. Steigman, and T.P. Walker, Phys. Rep. **333**(2000)389.

[10] A. N. Taylor and M. Rowan-Robinson, Nature **359**(1992)396.

[11] Y. Fukuda *et al.,* (Super-Kamiokande Collaboration), Phys. Rev. Let. **81**(1998)1562.

[12] S. Fukuda *et al.,*(Super-Kamiokande Collaboration), Phys. Rev. Let. **86**(2001)5651.

[13] The SNO Collaboration, Phys. Rev. Lett.**87**(2001)071301.

[14] R. D. Peccei and H. R. Quinn, Phys. Rev. Lett. **38**(1977)1440.

[15] S. DePanfilis *et al.,* Phys. Rev. Let. **59**(1987)839, W. Wuensch *et al.,*,Phys. Rev. D**40**(1989)3153.

[16] C. Hagmann *et al.,*, Phys. Rev. D **42**(1990)1297,C. Hagmann *et al.,* Phys. Rev. Let. **80**(1998)2043

[17] I. Ogawa *et al.,* Proc. of the 2nd RESCEU International Symposium on 'Dark Matter in the Universe and its Direct Detection', November p.175, 1996, Universal Academy Press.

[18] G. Jungman *et al., Supersymmetric Dark Matter* Physics reports**267**(1996)195.

[19] W. Ootani, doctoral thesis, University of Tokyo,1998.

[20] D. Reusser *et al.,* Phys. Lett. B **255**(1991)143.

[21] R.Bernabei *et al.,* Phys. Lett. B **424**(1998)195.

[22] R.Bernabei *et al.,* Phys. Lett. B **450**(1999)448, R.Bernabei *et al.,* Phys. Lett. B **480**(2000)23.

[23] CDMS Collaboration Phys. Rev. Lett. **84**(2000)5699.

[24] H.V. Klapdor-Kleingrothaus, Nucl. Phys. B Proc. Suppl., **100**(2001)350.

[25] Y. Suzuki, astro-ph/0008296.

[26] R.Bernabei *et al.,* Phys. Lett. B **389**(1996)757.

[27] P. F. Smith *et al.,* Phys. Lett. B**379**(1996)299.

[28] N.J. Spooner *et al.,* Phys. Lett. B**473**(2000)330.

[29] W.Ootani *et al.,*Phys. Lett. B **461**(1999)371,and W.Ootani *et al.,* Nucl. Instr. Meth. A **436**(1999)233.

[30] G.Angloher *et al.,*, submitted to Astropart. phys

[31] R. Bernabei *et al.*, Phys. Lett. B**509**(2001)197.

[32] H.Ejiri *et al.*, Phys. Lett. B**317**(1993)14.

[33] Super-Kamiokande Collaboration,astro-ph/0007003.

[34] AMANDA Collaboration Proceeding of the Third International Workshop on the Identification of Dark Matter, 499, World scientific, edited by Neil. J. C. Spooner and Vitaly Kudryavtsev.

[35] Piero Ullio, M. Kamiinkowski, and P Vogel, astro-ph/0010036.

[36] L3 Collaboration, Phys. Lett. B **350**(1995)109.

[37] A. Gabutti, M. Olechowski, S. Cooper, S. Pokorski, and L. Stodolsky, Astropart. Phys. **6**(1996)1.

[38] J. D. Lewin and P. F. Smith, Astropart. Phys. **6**(1996)87.

[39] J. Ellis,A. Ferstl, and A. Olive, Phys. Lett. B **481**(2000)304.

[40] J. Ellis and R. A. Flores, Phys. Lett. B **263**(2000)259.

[41] J. Ellis and R. A. Flores, Nucl. Phys. B**307**(1988)883.

[42] D.R. Tovey, R.J. Gaitskell, P. Gondolo, Y. Ramachers, L. Roszkowski, Phys. Lett. B **488**(2000)17.

[43] A. F. Pacheco and D.Strottman Phys. Rev. D **40**(1989)2131.

[44] M.T. Ressell *et al.,* Phys. Rev. D **48**(1993)5519.

[45] M.T. Ressell and D.J. Dean, Phys. Rev. C **56**(1997)535.

[46] J. Engel *et al.,* Phys. Rev. C **52**(1995)2216.

[47] G. Eder, *Nuclear Forces* (MIT Press, 1968), Chapter 7.

[48] A.K. Drukier, K, Freese, and D.N. Spergel, Phys. Rev. D **33**(1986)3495.

[49] K.M. Cudworth, Astron. J. 99(1990)590.

[50] American Institute of Physics Handbook, third edition, edited by D. E. Gray, (McGraw-Hill, New York, 1972)

[51] O.Meier *et al.,* Nucl. Instr. Meth. A **444**(2000)350.

[52] A. Alessandrello *et al.*, Phys. Lett. B**408**(1997)465.

[53] R. Bernabei *et al.,* Phys. Lett. B **389**(1996)757.

[54] G. J. Davies *et al.,* Phys. Lett. B **322**(1994)159.

[55] R. Hazama, doctor thesis, the Osaka University graduate school of science Toyonaka, Osaka, 1998.

[56] Y.Messous *et al.,* Astropart. Phys. **3**(1995)361.

[57] G.Gerbier *et al.,* Phys. Rev. D **42**(1990)3211.

[58] R. Bernabei *et al.,* Phys. Lett. B **436**(1998)379.

[59] B. I. Shkolovskii and A. .L. Efros, Electric Properties of Doped Semiconductors, Solid-State Science vol. 45, Spring-Verlag, Berlin Heiderberg New York Tokyo, 1984.

[60] W. Ootani *et al.,* Nucl. Instr. Meth. A **372**(1996)534.

[61] W. Ootani *et al.,* Astropart. Phys. **9**(1998)325.

[62] K. Miuchi, master thesis, University of Tokyo, 1999.

[63] K. Miuchi *et al.,* Proceeding of the Third International Workshop on the Identification of Dark Matter, 391, World scientific, edited by Neil. J. C. Spooner and Vitaly Kudryavtsev.

[64] J.I. Collar, J. Puibasset, T.A. Girard, D. Limagne, H.S. Miley, and G. Waysand, Phys. Rev. Lett. **85**(2000)3083.

[65] W. Ootani, master thesis, University of Tokyo, 1994.

[66] The Super-Kamiokande Collaboration, Phys. Lett. **452**(1999) 418.

[67] Drawn by A. Takeda.

[68] Purchased from Junkosha Inc.

[69] This measurement was performed by Tama Chemicals Co. Ltd. with ICP-MS(Inductively Coupled Plasma Mass Spectrometer) method.

[70] This measurement was performed with HPGe spectrometer at Kamioka Observatory owned by ICRR.

[71] Richard B. Firestone, Table of Isotopes Eighth Edition. CD-ROM Edition(Version 1.0, March 1996)

[72] A. de Bellefon *et al.,* Astropart. Phys.**6**(1996)35.

[73] This measurement was performed by Japan Energy CO.,LTD with ICP-MS(Inductively Coupled Plasma Mass Spectrometer) method.

[74] This measurement was performed by KANEKA TECHNORESEARCH CO.,LTD with ICP-MS(Inductively Coupled Plasma Mass Spectrometer) method.

[75] This measurement was performed by Kawatetsu TECHNORESEARCH CO.,LTD with GDS(Glow Discharge Emission Spectrometer) method.

[76] Kevlar cords are purchase from Goodfellow Cambridge Limited.

[77] Private communiaction with H.Sekiya.

[78] N.J. T. Smith, J.D. Lewin, P.F. Smith, Phys. Lett. B**485**(2000)9.

[79] H. Sekiya, master thesis, University of Tokyo, 2001.

[80] A. Takeda, master thesis, University of Tokyo, 2000.

[81] S.Pirro *et al.,* Nucl. Instr. Meth. A **444**(2000)71.

[82] S.Cebrián*et al.,* Astropart. Phys.**15**(2001)79.

[83] Review of Particle physics, Particle Data Group, Phys. Rev. D **50**(1994)1280.

[84] V. Bednyakov *et al.,* Z.Phys.A 357 (1997) 339

[85] A. Takeda, talk given at JPS meeting, 23 September 2001.
http://www.icepp.s.u-tokyo.ac.jp/~takeda/2001okinawa/

[86] H.Sekiya, talk given at JPS meeting, 23 September 2001.
http://www.icepp.s.u-tokyo.ac.jp/~sekiya/mywork/jps2001.pdf

[87] M.J. Lehner *et al.,* astro-ph/9905074, and D.P. Snowden-Ifft, C.J. Martoff, J.M. Burwell, astro-ph/9904064

[88] T.Tanimori, talk given at JPS meeting, 27 March 2001.

[89] Background measurement at Kamioka Observatory was performed by T. Namba.